

# **A pragmatic approach towards modeling microchannel condensation and evaporation**

THÈSE N° 6532 (2015)

PRÉSENTÉE LE 11 MARS 2015

À LA FACULTÉ DES SCIENCES ET TECHNIQUES DE L'INGÉNIEUR  
LABORATOIRE DE TRANSFERT DE CHALEUR ET DE MASSE  
PROGRAMME DOCTORAL EN ENERGIE

ÉCOLE POLYTECHNIQUE FÉDÉRALE DE LAUSANNE

POUR L'OBTENTION DU GRADE DE DOCTEUR ÈS SCIENCES

PAR

**Nicolas Espen ANTONSEN**

acceptée sur proposition du jury:

Prof. F. Maréchal, président du jury  
Prof. J. R. Thome, directeur de thèse  
Prof. C. Colin, rapporteuse  
Prof. D. Del Col, rapporteur  
Dr P. Leyland, rapporteuse



ÉCOLE POLYTECHNIQUE  
FÉDÉRALE DE LAUSANNE

Suisse  
2015



The important thing is to not stop questioning. Curiosity has its own reason for existing.  
— Albert Einstein

To my family...



# Acknowledgements

This work has been carried out at the Laboratory of Heat and Mass Transfer (LTCM), Swiss Federal Institute of Technology (EPFL), under the direction of Prof. John R. Thome. This study was supported by the European Space Agency which I gratefully acknowledge.

I would like to express my gratitude to Prof. John R. Thome for offering me the opportunity to develop this work and for his extensive guidance. I thank the members of the jury, Prof. Colin (Institut de Mecanique des Fluides de Toulouse), Dr. Davide Del Col (Univ. Padova), Prof. Marechal (EPFL) and Dr. Leyland (EPFL) for their valuable comments and suggestions.

I wish to acknowledge all my current and former friends from the LTCM for all the discussions and good time together, frequent coffee breaks and numerous outings in the mountains.

Finally, I would like to thank my family for all the support they gave me during these years.

*Lausanne, 10 February 2015*

D. K.



# Abstract

A numerical model for evaporation and condensation in microchannels is presented. The model uses a pragmatic mix of empirical correlations, numerical discretization and analytical models in order to describe the heat transfer and fluid flow performance in microchannel heat exchangers. It currently includes condensing and evaporating annular flows, and condensing and evaporating slug flows, in single and multi microchannels. For evaporating flows, dry patch formation and growth was included in the evaporation process. The range of operation handled by the model goes from low to high mass velocities and low to high pressure fluids. Each sub-model was validated against a set of experimental data from carefully selected laboratories. While not meant to be a fully numerical code, the model was developed with the purpose to be fast and reliable for engineering design of micro heat exchangers that is a pragmatic modeling code that is accurate and respects the main characteristics of the flow and heat transfer process. As such, it provides local outputs such as local heat transfer coefficient around the perimeter and perimeter-averaged, pressure drop gradients and local fluid charge in a matter of a few hours compared to a few days or weeks for complete CFD codes. Thus, it is particularly suitable for optimization purposes that require multiple simulations to be run. Finally, several parametric studies were run for selected processes.

**Keywords:** condensation, evaporation, numerical model, microchannel, conjugate heat transfer, annular flow, slug flow





# Résumé

Un modèle numérique pour l'évaporation et la condensation de réfrigérants dans des microcanaux est développé. Le modèle utilise un mélange de corrélations empiriques, de discrétisation numérique et de modèles analytiques prouvés de façon à décrire le transfert de chaleur et l'écoulement de fluides biphasiques dans des échangeurs de chaleur à microcanaux. Le modèle inclut actuellement les écoulements annulaires sous évaporation et condensation, les écoulements à bulles en condensation et évaporation dans un unique microcanal. Pour l'écoulement annulaire sous évaporation, le modèle inclut la création de patches de vapeur à la surface interne du canal. Le modèle a été validé avec un large éventail de résultats expérimentaux allant de bas à hauts débits et de réfrigérants à basse et haute pression. Chaque sous modèle a été validé par rapport à des données expérimentales de laboratoires sélectionnés. Malgré le fait que ce modèle numérique ne soit pas une discrétisation numérique complète des écoulements biphasiques, il a été développé avec l'idée de le rendre robuste, fiable et rapide pour le design d'échangeurs de chaleur en un temps réaliste. Par conséquent, il donne accès aux informations locales liées à l'échange thermique, tel que le coefficient de transfert de chaleur en chaque point du micro canal, les données moyennées sur le périmètre, les pertes de charge et la charge de réfrigérant nécessaire en quelques heures au lieu de quelques jours habituellement. Il est donc particulièrement adapté pour l'amélioration de l'échange thermique entre deux fluides et peut être intégré à des systèmes plus larges. Différentes analyses sont finalement conduites avec le modèle.

**Mots clés :** condensation, évaporation, modèles numériques, microcanaux, transfert de chaleur couplé, écoulement annulaire, écoulement à bulles



# Contents

<b>Acknowledgements</b>	<b>v</b>
<b>Abstract (English/Français)</b>	<b>vii</b>
<b>List of figures</b>	<b>xii</b>
<b>List of tables</b>	<b>xiv</b>
<b>Nomenclature</b>	<b>xvii</b>
<b>Introduction</b>	<b>1</b>
<b>1 Literature review</b>	<b>3</b>
1.1 Experimental condensation in microchannels . . . . .	3
1.2 Flow pattern transition for condensation in microchannels . . . . .	5
1.3 Numerical and mechanistic models for condensation in microchannels . . . . .	6
1.4 Experimental evaporation in microchannels . . . . .	7
1.5 Numerical and mechanistic models for evaporation in microchannels . . . . .	9
<b>2 Mathematical modeling</b>	<b>13</b>
2.1 Annular flow modeling . . . . .	13
2.1.1 Coordinate system . . . . .	14
2.1.2 Energy equations . . . . .	15
2.1.3 Mass conservation equation . . . . .	15
2.1.4 Momentum conservation . . . . .	16
2.1.5 Turbulent liquid film . . . . .	23
<b>3 Hybrid 1D/3D model for bubble nucleation, slug flow and elongated bubbles</b>	<b>27</b>
3.0.6 Mathematical model . . . . .	27
<b>4 Numerical resolution</b>	<b>37</b>
<b>5 Experimental validation</b>	<b>41</b>
5.1 Turbulent liquid film condensation validation . . . . .	41
5.2 Annular flow evaporation validation . . . . .	46
5.3 Slug flow and elongated bubble validation . . . . .	47

<b>6 Case studies</b>	<b>55</b>
6.1 Condensing turbulent annular flows . . . . .	55
6.2 Evaporating annular flows . . . . .	60
6.2.1 Bubbly flows and elongated bubbles in microchannels . . . . .	70
<b>7 Conclusions</b>	<b>77</b>
<b>A Color function calculation</b>	<b>79</b>
<b>B Laminar and turbulent liquid films</b>	<b>83</b>
<b>C Thin film integral model</b>	<b>85</b>
<b>Bibliography</b>	<b>91</b>
<b>Curriculum Vitae</b>	<b>93</b>

# List of Figures

1.1	Three zone model elongated bubble of Thome <i>et al.</i> [51]	9
2.1	Domain decomposition as in Nebuloni and Thome [32]	14
2.2	Three phase line transition, intrinsic meniscus, thin-film region and non-evaporating region	19
2.3	Dry patch identification	21
2.4	Vapor to liquid volume ratio identification	22
3.2	Bubble nucleation	30
3.3	Bubble Elongation	33
4.1	Resolution procedure for the annular flow model	39
5.1	Adiabatic entrance length definition for the experimental validation	41
5.2	Vapor to liquid volume ratio identification	42
5.3	Validation against experimental data of Del Col <i>et al.</i> , R134a at 31°C, square cross section with $D_h = 1.23mm$ , horizontal orientation	43
5.4	Validation against experimental data of Matkovic <i>et al.</i> [30], R134a at 31°C, Circular cross section with $D_h = 960\mu m$ , horizontal orientation	44
5.5	Validation against experimental data of Matkovic <i>et al.</i> , R134a at 31°C, Square cross section with $D_h = 1.18mm$ , horizontal orientation	45
5.6	Ong and Thome <i>et al.</i> [35] experimental setup	46
5.7	Ong and Thome [35] experimental comparison, mass velocity $G=200 \frac{kg}{m^2s}$	47
5.8	Ong and Thome [35] experimental comparison, mass velocity $G=400 \frac{kg}{m^2s}$	48
5.9	Elongated bubble front film thickness correlation of Moriyama <i>et al.</i> [31] modified by Dupont <i>et al.</i> [23] for R134a, R245fa and CO2	49
5.10	Predicted bubble velocity versus experimental results of Agostini and Thome [4]	50
5.11	Fully developed state definition	52
5.12	Ong and Thome <i>et al.</i> [35] heat transfer coefficient experimental validation for isolated bubble regime, Circular microchannel with $D_h = 1 mm$	53
6.1	Cross sectional liquid film thickness for square, circular and elliptical channel with $D_h = 1.23mm$	56
6.2	Cross sectional local dimensionless film thickness for square, circular and elliptical channel with $D_h = 1.23mm$	57
6.3	Cross sectional local eddy diffusivity for heat for square, circular and elliptical channel with $D_h = 1.23mm$	58

6.4	3D representations of the local heat transfer coefficient for square channel, $D_h = 1.23mm$ . . . . .	59
6.5	3D representations of the local heat transfer coefficient for square channel, test section of Agarwal <i>et al.</i> [2] . . . . .	59
6.6	Perimeter averaged heat transfer coefficient for square, circular and elliptical channel .	60
6.7	Liquid film profile, circular cross section $Dh = 1.03mm$ . . . . .	63
6.8	Heat transfer coefficient profile, circular cross section $Dh = 1.03mm$ . . . . .	63
6.11	Film thickness profile at outlet of microchannel at different times, $Dh = 1.03mm$ , R134a at $31^\circ$ . . . . .	66
6.12	Local Nusselt number at outlet of microchannel at different times, $Dh = 1.03mm$ , R134a at $31^\circ$ . . . . .	67
6.13	Liquid vapor interface at outlet of microchannel at different times, $Dh = 1mm$ , R-245fa at $31^\circ$ . . . . .	68
6.14	Liquid vapor interface at outlet of microchannel at different times, $Dh = 1mm$ , CO2 at $10^\circ$	69
6.15	Local heat transfer coefficient for bubble frequencies 29-85 Hz . . . . .	72
6.16	Wall temperature profile at $t = 2s$ for copper and silicon microchannels . . . . .	73
6.17	Start up phase, wall temperature variation with time . . . . .	74
A.1	Vapor to liquid ratio . . . . .	80
B.1	Liquid film velocity profile . . . . .	83

## List of Tables

5.1	Del Col <i>et al.</i> [21] annular flow condensation operating conditions . . . . .	42
5.2	Matkovic <i>et al.</i> [30] annular flow condensation operating conditions . . . . .	45
5.3	Ong <i>et al.</i> [35] annular condensation operating conditions . . . . .	46
5.4	Ong <i>et al.</i> [35] experimental validation parameters . . . . .	51
6.1	Turbulent Annular Flow Condensation Parameters . . . . .	55
6.2	Input parameters for circular and rectangular cross section simulations . . . . .	65
6.3	Heat transfer coefficient trends observed at high vapor qualities and corresponding interfacial resistance number . . . . .	70
6.4	Influence of frequency on overall heat transfer coefficient, input parameters . . . . .	71





# Nomenclature

## Roman Letters

A	Hamaker constant	$[kgm^2s^{-2}]$
Bo	bond number	[-]
C	color function	[-]
Ca	Capillary number	[-]
$C_f$	friction factor	[-]
$C_p$	heat capacity	$[J/K]$
$D_h$	hydraulic diameter	[m]
$f_{tp}$	friction factor	[-]
F	color function	[-]
G	mass velocity	$[kg/m^2 \cdot s]$
h	heat transfer coefficient	$[W/m^2 \cdot K]$
$\Delta h_{lv}$	latent heat of vaporization	$[J/kg]$
Ja	Jackob number	[-]
J	evaporative or condensive mass flux	$[kg/m^2 \cdot s]$
k	thermal conductivity	$[W/m \cdot K]$
L	length	[m]
$m''$	mass flux	$[kg/m^2 \cdot s]$
Nu	Nusselt number	[-]
p	pressure	[Pa]
Pr	Prandtl number	[-]
q	heat flux	$[W/m^2]$
r	bubble radius	[m]
R	universal gas constant	$[m^2s^{-2}K^{-1}]$
Re	Reynolds number	[-]
S	area	$[m^2]$
t	time	[s]
$t^+$	dimensionless liquid film thickness	[-]
T	temperature	[K]
v	local liquid film velocity	$m$
U	vapor velocity	$m/s$
We	Weber number	[-]
$W_N$	bubble front velocity	$[m/s]$
X	vapor quality	[-]
$X_{tt}$	Lockhart-Martinelly parameter	[-]

## Greek Letters

$\alpha_t^+$	eddy diffusivity for momentum	[-]
$\alpha_l$	thermal diffusivity	$[m^2/s]$
$\alpha_{sp}$	single phase flow heat transfer coefficient	$[W/m^2 \cdot K]$
$\alpha_{tp}$	two phase flow heat transfer coefficient	$[W/m^2 \cdot K]$
$\delta$	thickness	[m]
$\theta$	contact angle	[rad]
$\kappa$	interface curvature	$[m^{-1}]$
$\mu$	viscosity	$[Pa \cdot s]$
$\nu_t^+$	eddy diffusivity for momentum	
$\rho$	density	$[kg/m^2 \cdot s]$
$\sigma$	surface tension	$[N/m]$
$\sigma_{rec}$	receding contact angle	$[rad]$
$\tau$	shear stress	$[kgm^{-2}s^{-2}]$

## Subscripts

a	a
adv	advancing
CV	control volume
d	disjoining
F	forced
l	liquid phase
lim	micro to macro transition
m	mixture
R	receding
s	saturation
sp	single-phase
t	turbulent
tf	thin film
tp	two-phase
v	vapor phase
w	wall
$\partial$	interface
0	non-evaporating region

# Introduction

Two-phase flow heat exchangers have been used for decades as an efficient mean to remove or provide heat to a given source or sink by using the latent heat of fluids. Recent trends have seen a miniaturization of heat exchangers and cold plates in order to respond to the needs of compactness and from the surge in heat fluxes of electronic equipment. While technology has evolved widely over the past decades, the physical description and understanding of the phase change phenomena happening in microchannels has struggled to provide engineers with accurate models for calculating the performance of the latter. This task was further complicated by the differences in physical phenomena involved between macro, mini and micro scale heat exchangers, and between condensing and evaporating flows. As a result, the field is comprised of a segregated and vast set of experimental results, empirical or analytical models and numerical studies.

Microscale two phase flow heat exchangers have become trendy in the past 15 years with uses in electronic cooling, automotive, and HVAC industries among others. Their increased heat transfer performance and subsequent reduction of refrigerant charge have made it particularly appealing. Still, improved fundamental understanding of the physics happening in microchannels is needed as well as coherent modeling of the process.

Microchannel condensation has been investigated both analytically and numerically. In particular, the thinning of the liquid film and capillary forces arising from the microchannel corners has lead to improved geometries that can enhance the heat transfer efficiency of the heat exchanger while maintaining a low refrigerant charge and pressure drop. One of the first theoretical models was developed by Zhao and Liao [59] in 2002 and enhanced by Wang and Rose [56] in 2005. A model for microchannel condensation comprising a numerical discretization and selected empirical correlations was later developed by Nebuloni and Thome [32].

Microchannel evaporation has been studied both for low and high vapor qualities. In particular, extensive numerical modeling was done in the elongated bubble/slug flow regime using standard CFD techniques. A set of mechanistic and flow pattern based models were also developed to predict the elongated bubble/slug flow regime (taking as a basis the pioneering three zone model of Thome *et al.* [51]) and annular flow evaporation (such as the model of Cioncolini *et al.* [11]).

While mechanistic models are widely being used to obtain heat transfer and fluid flow data provide a first estimation of the heat exchanger performance, they fail at (i) covering a large set of experimental conditions other than the one it was developed for (ii) providing local quantities. Obtaining the local behavior of the heat flux or fluid flow often requires one to use full CFD that, while providing local characteristics, requires a considerable amount of resources to run (multiphase flow in laminar and

turbulent regimes). Finally, the dependence of two-phase flow modeling on initial and boundary conditions make it, for now, not a suitable tool for the design of heat exchangers.

The current research proposes to tackle the issues mentioned above by combining the power of numerical modeling and simplification of mechanistic models in order to develop a code that is reliable, fast and covers a large set of operating conditions. Based on the preliminary work done by Nebuloni and Thome *et al.* [32], the current research was divided into 3 distinct steps:

1. Base code understanding and extension to curved channels and turbulent annular flows
2. Extension to evaporating annular flows and dry patch modeling
3. Extension to nucleating bubble and slug/elongated bubble flow

The thesis will firstly give an overview of the state of the art research done in the field of two-phase flow modeling, covering both numerical and experimental modeling methods. The mathematical model used will then be depicted, an experimental validation carried out and some simulation results will be provided.

# 1 Literature review

Microscale heat transfer and fluid flow spans a large variety of configurations and operating conditions. Added to that the difficulty to mathematically describe the physical phenomena of the phase change, this has led to various attempts to develop either fully numerical models or mechanistic models that unfortunately only work for a narrowly selected set of operating conditions of interest to heat exchangers. While 2D and 3D numerical codes that fully model the phase change phenomena are on the rise, the high computational cost and the difficulty to set coherent initial and boundary conditions do not make them, yet, a viable engineering tool. In an attempt to answer the engineers dilemma of minimizing the refrigerant load and pressure drop while answering the heat transfer requirements, a few pragmatic models were developed that, while still discretizing the fluid flow and heat transfer equations in the medium, include a blend of empirical correlations, with the objective to reach an engineering design realistic time scale within a coherent time span.

## 1.1 Experimental condensation in microchannels

Condensation is a heat transfer mechanism occurring from a fluid to a cold element. In the case of in-tube condensation, the fluid can enter a given channel at a thermodynamic quality above 1, equal to 1 or lower than 1. Four different types of condensation are identified and well documented in Thome [50] in 2008, namely *drop-wise* condensation, *film wise* condensation, *direct contact* condensation and *homogeneous* condensation. Presently, film wise condensation will be addressed.

Several experimental studies covering micro and mini channel condensation are currently available in the literature and cover a large range of the flow pattern regimes, fluids and operating conditions. However, the difficulty to capture the small heat loads resulting from the condensation process makes it difficult to obtain experimental results that are reliable. It is believed that as the dimensions of the channels decrease, the capillary forces at the liquid-vapor interface that can be a consequence of non-circular cross sectional geometries or wavy vapor-liquid interfaces tend to dominate over inertia and body forces in the liquid film. However, this transition from an inertial regime, occurring when liquid films are thick, to capillary dominated regime is not yet well defined. Recent studies give this transition to be anywhere between 1 and 10 mm hydraulic diameter while below  $100\ \mu m$  we are mostly certain to have a capillary dominated regime. Furthermore, the transition will be different when we consider the slug flows/ elongated bubble flow regime rather than the annular flow regime and will be also dependent on the geometry/shape of the microchannel (certainly a reason for the discrepancies).

Experimental studies carried out in the last decades have allowed authors to develop fully empirical models, which are generally limited to the range of application the experiments were run at, and then more recently develop empirical models with some mechanistic description of the physics occurring during the phase change. In 2006, Bandhauer *et al.* [5] carried out an experimental campaign on condensation of R134a in horizontal microchannels with circular cross sections and hydraulic diameters ranging from 0.506 to 1.524 mm. Heat duties at their selected mass fluxes ( $G=150-750 \frac{kg}{m^2s}$ ) were so small that if the heat transfer coefficients were to be developed from measurements directly at the inlet and outlet of the microchannel, the resulting uncertainties would be too large to be considered as reliable. The authors overcame this conflict by developing a thermal amplification technique where water flows at high flow rate in a primary loop and cools down the refrigerant, and then the primary loop is cooled down by a secondary loop with water at a much lower mass flow rate, resulting in larger temperature differences and lower uncertainties. Data were obtained for three different hydraulic diameters, with vapor qualities ranging from 0.15 to 0.85, hence covering the whole range of flow regimes. The authors then developed a mechanistic model for predicting the heat transfer and pressure drop in microchannels and validated it against their own set of data. They also pinpointed the need for specific models for microchannels as models developed for larger tubes tended to underestimate the importance of the interfacial shear between the liquid and the vapor. The mist flow correlation developed by the authors reads as:

$$Nu = 0.00345 Re_m^{0.9} \left( \frac{\mu_v \Delta h_{lv}}{k_v (T_s - T_w)} \right)^{1/3} \quad (1.1)$$

where the two-phase mixture viscosity is defined as:

$$\mu_m = \left( \frac{X}{\mu_v} \frac{1-X}{\mu_l} \right)^{-1} \quad (1.2)$$

They assume the liquid is shear driven by the vapor core, entraining droplets and forming a mist flows.

Koyama *et al.* [29] developed a correlations based on their experimental results of R-134a in multi-port extruded tubes with 1.1mm and 0.8 mm hydraulic diameters. The authors expressed the Nusselt number in terms of an asymptotic combinations between convective condensation and gravity driven condensation:

$$NU = (Nu_F^2 + Nu_B^2)^{1/2} \quad (1.3)$$

where the forced convection Nusselt number is given by:

$$Nu_F = 0.0152(1 + 0.6 Pr_l^{0.8}) \left( \frac{\Phi_v}{X_{tt}} \right) Re_l^{0.77} \quad (1.4)$$

where the Reynolds number is given by  $Re = \frac{G(1-X)D_h}{\mu_l}$  and the Lockhart-Martinelli parameter is given by:

$$X_{tt} = \left( \frac{1-X}{X} \right)^{0.9} \left( \frac{\rho_v}{\rho_l} \right)^{0.5} \left( \frac{\mu_v}{\mu_l} \right)^{0.1} \quad (1.5)$$

The gravity controlled condensation is given by  $Nu_B$  as:

$$Nu_B = 0.725 H(\epsilon) \left( \frac{Ga Pr_l}{Ja} \right)^{1/4} \quad (1.6)$$

where  $Re_{lo}$  is the liquid only Reynolds number  $Re_{lo} = GD_h/\mu_l$ .

Cavallini *et al.* proposed a model for the entrainment of the liquid phase into the vapor core, expressed as a function of the dimensionless temperature and the shear stress:

$$h = \frac{\rho_l C_{p,l}}{T^+} \sqrt{\frac{\tau}{\rho_l}} \quad (1.7)$$

where the dimensionless temperature is given for different dimensionless thickness.

Del Col *et al.* [22] investigated experimentally the local heat transfer coefficients during condensation of the low GWP refrigerant R1234yf in a single circular microchannel of 0.96 mm hydraulic diameter which they compared to their earlier data from R134a from Matkovic *et al.* [30]. Their data included results for mass velocities ranging from 200 to 1000  $\frac{kg}{m^2 s}$ . In order to capture the small heat loads and temperature gradients, they developed a novel test section that is composed of an inner channel where the refrigerant flows and an outer channel where the cooling water flows. The outer channel is included in the test section in a solenoidal manner and thermocouples measure the water temperature that is then used to calculate the local heat transfer coefficient. Results for R1234yf depicted lower heat transfer performance compared to R134a, for instance 15% lower at 200  $\frac{kg}{m^2 s}$ .

## 1.2 Flow pattern transition for condensation in microchannels

While experimental data is important for the development of empirical and mechanistic models and the validation of numerical models, a further requirement is an understanding of the different flow regimes the fluid goes through as it condenses is, in order to develop coherent analytical and mechanistic models that respect the two-phase flow structures. Furthermore, the different trends in heat transfer and fluid flow performance encountered experimentally at low and high vapor qualities pin point the need for an accurate description of the transition between flow regimes. For instance, at low vapor qualities, where the liquid slug/elongated bubble regime dominates, the performance of the microchannel is directly dependent on the speed and frequency of the bubbles, while at high vapor qualities where the annular flow regime dominates and is modeled as a condensing falling film flow, the performance is dependent on the microchannel cross sectional shape. Such differences should lead the designer to consider different approaches depending on the range where his heat exchanger will operate or the design model should be able to capture these two important flow regimes.

Coleman and Garimella [14] started in 1999 developing a comprehensive flow regime map that at first only included adiabatic flows. They defined 6 different flow regimes based on observations of an air-water mixture flowing in transparent tubes with hydraulic diameters ranging from 1.3 to 5.5 mm. The regimes identified were *annular*, *elongated bubble*, *slug flow*, *wavy-annular*, *bubble* and *dispersed* flow patterns. The experimental transitions were compared with available correlations for air-water mixtures and adiabatic conditions.

Later, the same authors in [15] developed a simple flow pattern map for R134a in-tube condensation in mini channels with hydraulic diameters ranging from 2.67 to 4.91 mm and mass velocities between 150 and 750  $\frac{\text{kg}}{\text{m}^2\text{s}}$ . They considered cross sections of round, square and rectangular shapes. The different flow regimes identified from the experiments were classified into 4 categories: *annular*, *wavy*, *intermittent* and *dispersed* type. Each flow regime was then further divided into different flow patterns, for instance, the annular flow pattern would include *mist flow*, *annular ring*, *wave ring*, *wave packet* and *annular film* that would often be related to the level of instability of the liquid film or vapor core.

While the diameters mentioned above still lie in the upper range of microscale channels and could even be considered as mini channels, authors have also attempted to identify the transition in the case where the capillary forces are dominant. For instance, all the instabilities mentioned in the work of Coleman and Garimella [15] that lead to different flow patterns for each flow regime disappear as the capillary forces become dominant.

In another study, Quan *et al.* [39] identified condensation flow patterns in micro channels of 120 and 128  $\mu\text{m}$  hydraulic diameter. Overall, they identified *mist*, *annular*, *injection*, *plug/slug* and *bubbly* flows. They also investigated the influence of the mass velocity on the *annular* to *plug/slug* flow transition.

### 1.3 Numerical and mechanistic models for condensation in microchannels

Over the past 15 years, researchers have attempted to develop models that accurately capture different outputs of the condensation processes such as liquid film profile, heat transfer behaviors, pressure drop or fluid charge. As a matter of simplicity, we will only consider here the models developed for annular flow condensation and bubbly flow condensations. Other flow patterns are generally transition patterns and covering a very small part of the vapor quality range, in addition to being too difficult to model.

One of the first attempts to model annular flow condensation was carried out by Zhao and Liao [59] who developed an analytical model for predicting film condensation of vapor flowing inside a triangular microchannel. The model takes into account the effects of capillary forces, interfacial shear stress, interfacial thermal resistance and gravity. While the authors identified increased thermal performance for the triangular geometry compared to standard circular geometries, due to the thinning of the liquid substrate on the faces, their model was not validated against any experimental data.

In 2005, Wang and Rose [56] presented a theoretical model to predict condensation heat transfer inside triangular and rectangular mini or microchannels. They ran simulation test cases for hydraulic diameters varying from 0.5 to 5 mm and fluids R134a, R22 and R410a assuming a fixed temperature as a boundary condition.

Nebuloni and Thome [32] developed in 2010 a numerical code for simulating annular condensing flows in microchannels of any arbitrary shape. The code assumes a laminar liquid film behavior while the vapor core can be in a laminar, transition or turbulent state. It also takes into account conjugate effects by allowing a selection of boundary conditions, such as heat fluxes or external heat transfer coefficient. The authors validated the model against an extensive set of data and were able to



conduct studies on the influence of the cross section on the thermal and hydraulic performance of the microchannel. In particular, they noted the importances of the channel faces for the enhancement of the heat transfer due to the creation of thin liquid films with very low thermal resistances. The same authors later added oil effects to the model that can be useful for instance for automotive applications.

Da Riva and Del Col [19] used a VOF method for tracking the interface of a condensing annular flow in a 1 mm microchannel where the liquid film is treated as laminar while the vapor core is modeled using a  $k - \omega$  model. Bortolin *et al.* [8] later investigated annular flow condensation in a 1 mm square minichannel where both the liquid film and vapor core are in a turbulent state and modeled using a SST  $k - \omega$  model. In the latter, the authors investigated mass velocities of 400 and 800 kg/m<sup>2</sup>s. The turbulence state of the liquid film in a condensing annular flow has currently not been resolved due to the complexity of characterizing turbulence intensity in a very thin film with strong surface tension forces that dampen or cancel the eddy diffusivity for heat and momentum. Hence, while the transition from a laminar to a turbulence driven liquid film can be observed experimentally from the change of slope of the heat transfer coefficient versus the vapor quality, as well as the pressure drop, numerically, the transition criterion is often arbitrary and does not take into account the transitory state. In an attempt to understand the transition in minichannels, which may vary for each geometry or operating conditions, Da Riva and Del Col [20] compared simulations and experimental results for R134a in a 1 mm minichannel for mass velocities ranging from 50 to 1000 kg/m<sup>2</sup>s where the liquid film was treated as either in a laminar or turbulent state. Results showed that for higher mass velocities, the laminar liquid film assumption greatly underpredicted the heat transfer coefficient and in particular did not capture the influence of the mass velocity on the heat transfer coefficient that can be found experimentally. The turbulent liquid film assumption showed a fairly good agreement with experimental results carried out in their laboratory.

## 1.4 Experimental evaporation in microchannels

Condensation in microchannels sees its main challenges arising in experiments from the low heat loads involved and low temperature differences that make it difficult to obtain results with a low uncertainty. Evaporations, on the other end, has been widely investigated experimentally and faces different challenges when it comes to obtaining experimental results or developing models. Steinke and Kandlikar [27] provide an extensive review of experimental studies carried out between 1982 and 2003. The review shows a fair amount of studies held for hydraulic diameters up to 500 μm and less in the range 500 μm - 3 μm for Reynolds numbers between 10 and 1000. Szczukiewicz *et al.* [48] provide a review of experimental and numerical studies carried out until 2013. From a design stand point, the challenges faced by engineers differs from microchannel condensation. In Bergles *et al.* [6] the authors point out the two main problems being the flow distribution in parallel microchannels as bubble nucleation is likely to cause back-flow, and the conjugate effects, becoming more important as the diameter decreases. The first problem was solved in Szczukiewicz *et al.* [47] with the use of restrictions at the inlet of the microchannels that prevent back-flow from occurring. The second issue is yet under investigation as experiments, in particular measurement of local wall temperature is still not achieved. Temperature measurements of the footprint would not allow one to obtain the rate of axial conduction in microchannels for example and data reduction methods currently being used tend to assume a 1D conduction across the wall. The understanding of local conduction resistance is of foremost importance as channel size decreases and the relative importance of wall conduction

to liquid film/inner wall convection becomes larger. In particular, it can play an important role in reducing the burnout of the microchannel through azimuthal conduction when local dryout occurs.

Experimental studies on flow boiling in microchannels have been going for more than 20 years. While it would be too extensive to cite them all, a few key studies are mentioned here based on the review of Szczukiewicz *et al.* [48]. Back in 1996, Tran *et al.* [52] performed experiments of R12 in small circular and rectangular channels with hydraulic diameters of respectively 2.46 and 2.4 mm. They found the nucleation mechanism to dominate over the convective mechanism based on observations that the heat transfer was function of the heat flux, which is opposed to a convection dominated flow in macrochannels. They also found little difference between circular and rectangular channels for the given operating conditions.

Flow boiling in a vertical multiport extruded tube with channels of 3.28x1.47 mm was investigated by Agostini and Bontemps [3] in 2005. The authors also found that nucleate boiling was the dominant mechanism for heat fluxes above  $14 \frac{kW}{m^2}$  and were able to obtain the transition from a nucleate to convective boiling. Dryout conditions were obtained for vapor qualities as low as 0.4.

Revellin *et al.* [43] carried out experiments on adiabatic and diabatic colliding bubbles in microchannels of 509 and 790  $\mu m$ . A model for predicting the collision of elongated bubbles in microchannels was proposed and the bubble length distribution along the microchannel obtained.

Agostini *et al.* [4] studied R236fa and R245fa boiling in a silicon multi microchannel heat sink. The heat sink was composed of 223x680  $\mu m$  microchannels and the authors conducted experiments up to vapor qualities of 0.75, heat fluxes between 3.6 to 221  $\frac{W}{m^2}$  and mass velocities between 281 and 1501  $\frac{kg}{m^2s}$ . The local heat transfer coefficients were calculated and for the first time the heat transfer coefficient depicted a maximum value at very high heat fluxes.

Karayiannis *et al.* [28] investigated flow boiling in vertical tubes with diameters ranging from 0.52 to 4.26 mm with R134a. They changed the mass velocities between 100 and 700  $\frac{kg}{m^2s}$  and heat fluxes from 1.6 to 135  $\frac{kW}{m^2}$ . As in other studies, the heat transfer coefficients increased with increasing heat flux and with decreasing hydraulic diameters.

Ong and Thome ([33], [34]) investigated the macro-to-micro scale transition for three fluids: R134a, R236a and R245fa. The circular channels had diameters of 1.03, 2.2 and 3.04 mm. The authors developed an improved flow pattern map that is suitable for smaller channels. Also, with a measurement of the top and bottom liquid film thickness they were able to demonstrate that the gravity forces are totally suppressed by surface tension and capillary forces when the Confinement number approaches 1. Furthermore, the heat transfer data showed a monotonically increasing heat transfer coefficient with increasing vapor quality (due to the annular flow regime) and decreasing heat transfer coefficient at low vapor qualities, depicting a U shape profile over the whole range of vapor qualities. Finally, they were also able to propose a new critical heat flux correlation that is valid for small diameter channels.

Finally, Vakili-Farahani *et al.* [53] investigated upward flow boiling in multiport extruded tubes with 1.1x2.1 mm channels for R245fa and R1234ze. A new data reduction technique was proposed and the effects of vapor quality, heat flux and saturation temperature were investigated. They found the heat transfer coefficient to increase with the vapor quality when the annular flow prevails and see a decrease when intermittent dryout occurs.

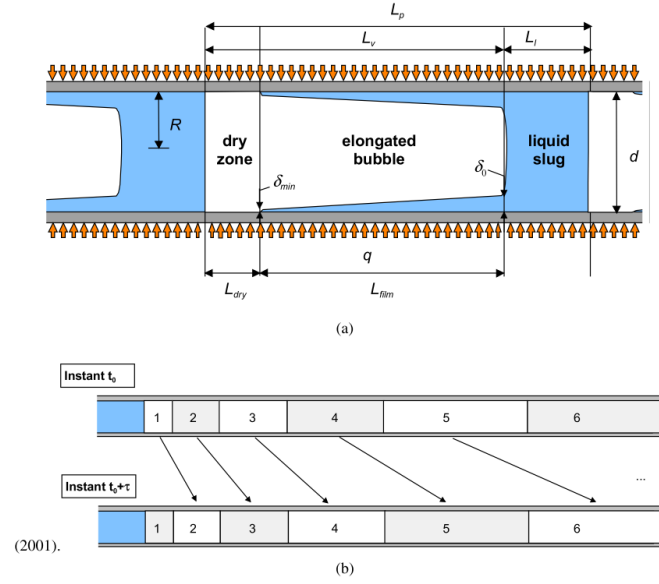


Figure 1.1: Three zone model elongated bubble of Thome *et al.* [51]

## 1.5 Numerical and mechanistic models for evaporation in microchannels

Despite infrared thermography or other high resolution techniques to measure and capture the flow and heat transfer characteristics in microchannel heat transfer, there is currently no non-invasive way to access the physical fluid flow and heat transfer behavior inside the microchannel. As such, numerical simulations can provide on one hand a deep understanding of the local heat and fluid flow behavior while mechanistic models prove to be rather accurate by using experimental observations to develop simple models that can predict the overall heat transfer and fluid flow behavior.

Several studies have tried to develop mechanistic models to capture the heat transfer and fluid flow behavior more accurately than raw empirical models. In the current section we will point out the main flow pattern based models that are relevant to our research, i.e. annular flow models and liquid slug/elongated flow models which cover 95% of the flow pattern map. Recent additions to critical heat flux models are also mentioned.

One of the most accurate models to describe evaporation of elongated bubbles in microchannels was proposed by Thome *et al.* [51] in 2004. Despite multiple attempts to improve it, the model is, up to now, the most accurate one for predicting flow boiling in the elongated bubble regime. The model conceptually divides the elongated bubble into a liquid slug, dry zone and elongated bubble as shown in 1.1. Each region is then modeled with available heat transfer correlations and a time-averaged heat transfer coefficient can be obtained. In particular, the results show the critical importance of the bubble frequency, minimum liquid film thickness at dryout and liquid film formation thickness. Heat transfer in the liquid film is shown to be several times higher than in the liquid slug, which confirms the need for an accurate modeling of the film surrounding the bubble and eventually the importance of the microchannel geometry. However, the minimum thickness of the liquid film at dryout, proposed in their recent work to be taken as the roughness height, is still subject to debate and not a solved issue.

In a later study, Dupont and Thome [23] investigated the influence of the channel diameter on flow boiling and the transition from macro to microchannel evaporation using the three-zone model of Thome *et al.* [51]. The results obtained showed an influence of the diameter on the heat transfer coefficient due to the thinning of the liquid film when the channel diameter decreases (and provided that the thin film heat transfer is the main heat transfer mechanism). Revellin *et al.* [43] then developed a model for predicting colliding elongated bubbles in microchannels. The bubble speed and frequency playing a critical role in the time averaged heat transfer coefficient, and thus Agostini *et al.* [4] developed an analytical model that displays an increase in bubble velocity with an increase in bubble length.

Costa-Patry and Thome [18] later developed a flow pattern based method by combining the three zone model of Thome *et al.* [51] and the comprehensive annular flow model of Cioncolini *et al.* [12] in order to cover the complete range of vapor qualities. The three zone model was also modified slightly in order to improve its performance. For instance, the arbitrary minimum thickness was set to the wall roughness, assuming that the liquid film breaks once it reaches the roughness thickness. The model of Costa-Patry and Thome [18], and secondly the method of Bertsch *et al.* [7], seem to be the most accurate available today.

Harirchian and Garimella [25] also used the three zone model to predict their own experimental data ([24]) for 7 microchannel heat sinks and proposed a new flow pattern based prediction method that showed reliable results for one test fluid.

Overall, most observations carried out up to date in microchannel flow boiling, depict a U trend relationship between the heat transfer coefficient and the vapor quality, with the heat transfer coefficient decrease with respect to increasing vapor quality, at low vapor qualities, and the heat transfer coefficient increasing with vapor quality at high vapor qualities.

The annular flow model of Cioncolini and Thome [11] developed in 2011 to describe the heat transfer, liquid to vapor entrainment and friction factor in the annular flow regime, currently shows some of the most accurate predictions for this regime. However, its use has to be limited to the case of turbulent liquid films, i.e. generally at high mass velocities, otherwise the model would not predict accurately the heat transfer behavior.

Numerical studies on flow boiling heat transfer often requires the usage of modified traditional CFD methods to take into account the change in physical properties due to the boiling process. In particular, both Volume Of fluid and Level Set methods can be used to solve the energy, mass and momentum equations. Both methods treat the domain as a single fluid with varying density and a Heaviside function that identifies the vapor and liquid cells. A weakness of such a method is that the interface is not explicitly defined and needs to be reconstructed by the means of a color function field, originally proposed by Blackbil [9]. Such a procedure is however generally computationally very intensive and expensive. When we reduce the scale of the problem and tend towards microchannels, the appearance of additional forces such as the interface resistance, the disjoining and capillary forces tend to increase the temperature discontinuity at the liquid vapor interface, generating an increased interfacial resistance acting against interfacial mass transfer.

Wang *et al.* [55] developed a linearized expression of the interfacial mass transfer for the low liquid-vapor temperature jump (at maximum 5K) that was implemented in various solvers for both con-

densation and evaporation. When a dry patch is created, its numerical treatment requires the use of empirical imposed contact angles at the three phase line. One approach is to enforce the normal vector to the interface with the value of the calculated contact angle (Brackbill *et al.* [9], Renardy *et al.* [42], Afkhami and Bussmann [1]).



## 2 Mathematical modeling

In this chapter the annular flow model will be explained in detail. The model is based on the condensing annular flow model developed by Nebuloni and Thome [32] and was extended to include (i) turbulent liquid films for condensation (ii) evaporating annular flow (with both turbulent and laminar liquid film assumption) (iii) dry patch modeling and treatment. As such, the new model extended the applicability of the code to a larger set of problems and operating conditions.

### 2.1 Annular flow modeling

The present pragmatic model, initially developed for condensing annular flows, was extended to evaporating and slug/elongated bubble flows. As such, a modification of the structure was carried out in order to adapt to the new development. Separate codes deal with the different process types, for instance evaporating and condensing annular flows and bubbly/elongated bubble flows. Then, sub-models are implemented into the parent codes to treat turbulent liquid films, thin films or contact angles.

The same modeling approach as in Nebuloni and Thome [32] was followed for discretization of the annular liquid film. The central vapor core is discretized axially only while the liquid film is discretized in the axial and circumferential directions as can be seen in Fig. 2.1. The main assumptions used by the authors, still hold here:

- the computational domain is divided into two distinct regions, a vapor core and a liquid film
- the flow in the vapor core is either laminar, turbulent or in transition. The flow in the liquid film is either laminar or turbulent.
- in the liquid film, the radial component of the velocity is assumed to be negligible.
- the sensible heat is neglected with regards to the latent heat in the energy equation. Thermal conduction across the liquid film is assumed to be the dominant heat transfer mechanism when the film is thin. At the contact line region, thin-film evaporation dominates. In the dry patch, wall to vapor heat convection is the dominant mechanism.
- fluid properties are assumed to be constant in time and space.

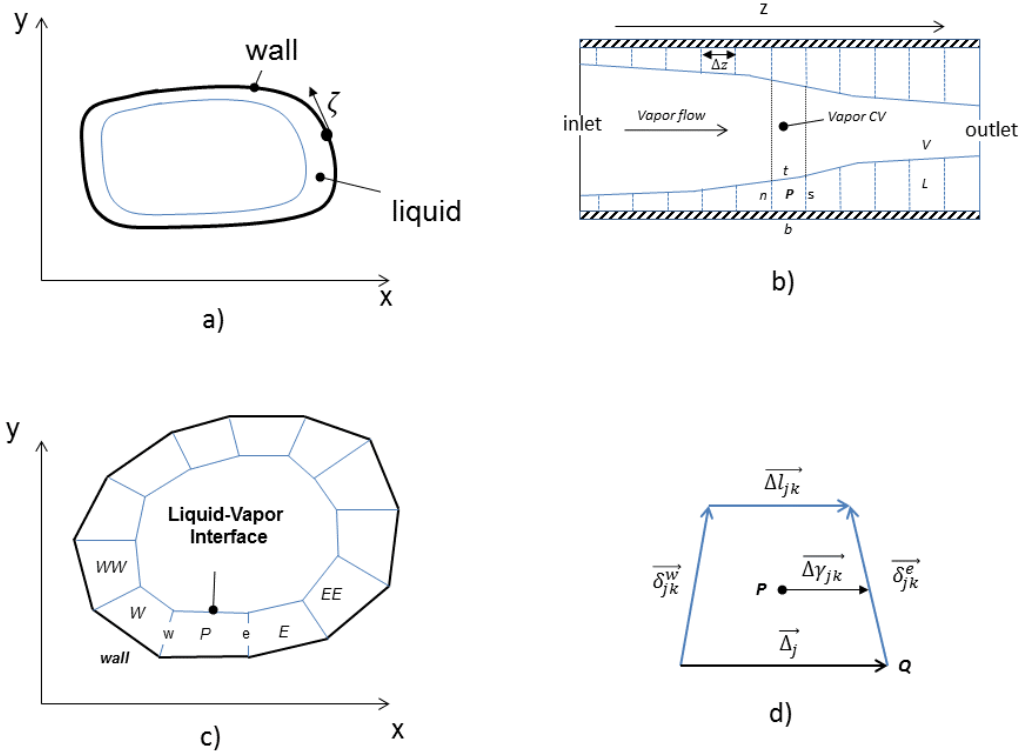


Figure 2.1: Domain decomposition as in Nebuloni and Thome [32]

- interfacial mass transfer is taken into account when the film is thick. Disjoining pressure is taken into account in the thin film region.
- the boundary conditions considered are (1) wall temperature (2) uniform wall heat flux for both evaporation and condensation. Adiabatic annular flow can also be simulated.
- the effects of gravity and inlet flow disturbances can be considered.
- the liquid-vapor interfacial shear stress is modeled empirically

### 2.1.1 Coordinate system

We consider two different cases, when the liquid film fully coats the wall and when secondly a dry patch is created. In the first case, no changes in the coordinate system are made and the grid is used to discretize the annular liquid film as explained in Nebuloni and Thome [32] (see Fig. 2.1). In the second case, and in order to take into account dry patches that are likely to be created during the evaporation process, the control volumes can either be filled with liquid or in a vapor state (for modeling the dry patch).

The domain is discretized using a finite volume approach as shown in Fig. 2.1. A grid is created on



the inner wall of the microchannel with a vapor core at the center. By using a lubrication approach for modeling thin films, the momentum, mass and energy conservation equations can be expressed as mean flow equations for the axial and circumferential velocity and with respect to the liquid film thickness. The momentum and energy conservation equations for the liquid film are discretized in the axial and circumferential directions in the liquid film sub-grid, while the vapor core is discretized axially only. The liquid film is treated in the local reference system as a fluid bounded flow, with the vapor core acting as a shearing fluid in form of a boundary condition for the liquid film. Such an approach removes the need to fully discretize the vapor flow and the liquid-vapor interface, thus reducing the computational time.

A 1D axial conduction problem is solved across the liquid film in order to model both evaporation and condensation processes. The conjugate problem is taken into account by incorporating 2D axial and circumferential conduction at the wall. Three types of boundary conditions are considered: imposed wall temperature, imposed wall heat flux or external convective cooling or heating.

### 2.1.2 Energy equations

While a 2D conduction problem is solved in the wall domain, a simple 1D conduction problem is solved across the liquid film by taking into account the effect of evaporation. When a dry patch exists, an empirical heat transfer correlation is used to model the wall to vapor convection process. By using a color function approach generally used in VOF methods, a general equation can be derived for both a fully wet and partially wet microchannel, as follows, where the inertial effects in the liquid film are neglected as well as inertial effects in the wall:

$$(1 - C_{j,k})\beta_{j,k}\Delta h_{l,v}J_{j,k} + C_{j,k}h_{j,k}^{dry} + q_{j,k}^{tf} + q_{jk}'' + k_w\delta_w\nabla_{\xi,z}^2 T^w = 0 \quad (2.1)$$

where  $C_{j,k}$  is the color function identifying the dry and wet regions,  $q_{j,k}^{tf}$  is only active at the contact line cells and calculated by using an analytical solution for the thin film problem where  $q_{j,k}$  is provided by the model of Wang *et al.* [54].  $q_{j,k}''$  is the imposed heat flux and  $h_{j,k}^{dry}$  is the dry patch wall to vapor heat transfer rate. The calculation of the color function, the thin film heat flux and the wall to vapor heat transfer coefficient will be explained in upcoming sections. In Eq. 2.1 the subscripts j and k denote the axial and circumferential control volume.

### 2.1.3 Mass conservation equation

We explain here the case where the liquid film completely wets the inner channel and no dryout occurs. The case of dry patches will be treated later. In that case, the mass conservation equation can be stated for both the vapor core and the liquid film domain. The equation needs to take into account the moving liquid-vapor interface as well as interfacial evaporation or condensation. While stated here for the condition where the liquid fully coats the inner channel, the mass conservation is also similar in the case of a dry patch.

## Liquid Domain

The mass conservation for a generic control volume  $\Delta\Omega$  filled with liquid can be expressed in its integral form as:

$$\frac{d}{dt} \int_{\Delta\Omega} d\Omega = \int_{\partial\Delta\Omega} (\vec{v}_\partial - \vec{v}) \cdot d\vec{S} \quad (2.2)$$

where the term on the right side of the equation is the boundary mass flux due to evaporation or condensation through the liquid-vapor interface. The condition at the liquid vapor interface is obtained by the evaporative or condensing volumetric flow rate:

$$\int_{\partial\Delta\Omega_{j,k}} (\vec{v}_\partial - \vec{v}) \cdot d\vec{S} = \frac{1}{\rho_l} J_{j,k} \Delta S_{j,k}^t \quad (2.3)$$

where the evaporative/condensing volumetric flow rate  $J_{j,k}$  only takes into account the contribution due to the temperature gradient and not the thin film effect. Close to the three phase line, the contribution of the thin film region to the evaporative mass flux is added to the corresponding cells as a source term:

$$\int_{\partial\Delta\Omega_{j,k}^{tf}} (\vec{v}_\partial - \vec{v}) \cdot d\vec{S} = \frac{1}{\rho_l} m_{tf}'' L_{tf} \quad (2.4)$$

where  $L_{tf}$  is the computed thin film length in a given control volume.

## Vapor domain

The vapor core domain is axially discretized and for each vapor control volume  $\Delta\Omega_k^v$  we can write the time derivative of each vapor control volume as:

$$\frac{d}{dt} \Delta\Omega_k^v = - \frac{d}{dt} \sum_j \Delta\Omega_{j,k} \quad (2.5)$$

The mass conservation equation for a given control volume is derived to be:

$$(U^v S^v)_{k+1} = (U^v S^v)_k + \sum_j \left( \frac{1}{\rho_l} - \frac{1}{\rho_v} \right) J_{j,k} \Delta S_{j,k}^l + \sum_j \frac{1}{\rho_l} m_{tf}'' L_{tf} \quad (2.6)$$

where the last term represents the sum of all the thin film source terms that are to be added to a vapor control volume.

### 2.1.4 Momentum conservation

The momentum conservation equation for the liquid domain can be defined in its integral form as:

$$\frac{d}{dt} \int_{\Delta\Omega_{j,k}^l} \vec{v} d\Omega = \int_{\partial\Delta\Omega_{j,k}^l} \vec{v} (\vec{v}_\partial - \vec{v}) \cdot d\vec{S} + \int_{\Delta\Omega_{j,k}^l} \vec{f}_b d\Omega + \int_{\partial\Delta\Omega_{j,k}^l} \left( -\frac{p}{\rho} \vec{I} + \frac{\mu}{\rho} (\vec{\nabla} \vec{v} + \vec{\nabla} \vec{v}^T) \right) \cdot d\vec{S} \quad (2.7)$$

The liquid film pressure is governed in a liquid cell by the capillary forces and momentum transfer

due to the evaporating process:

$$p_i^{j,k} = p_k^v + \sigma\kappa + \left(\frac{1}{\rho_v} - \frac{1}{\rho_l}\right) \left(J_{jk}^e\right)^2 \quad (2.8)$$

where  $\sigma\kappa$  is the curvature of the liquid-vapor interface in the case that is no partial dryout. When dryout occurs, the use of the Blackbill force accounts for the change in the surface tension force at the three zone line:

$$p_{j,k}^i = p_k^v + \sigma\kappa F + \left(\frac{1}{\rho_v} - \frac{1}{\rho_l}\right) \left(J_{jk}^e\right)^2 \quad (2.9)$$

where  $F$  is the color function defining the liquid and vapor in the grid and  $\kappa$  the interface curvature. When a three phase line is created from the drying out of the liquid film, the transitions from the liquid film to the dry wall needs a contact angle to be imposed at the cells where the contact line is present. The value of the contact angle is obtained experimentally and is imposed as a boundary condition to the liquid domain. In other numerical models, one approach to implementing the contact angle model into the numerical discretization is to use a Blackbill force that models the behavior of the liquid vapor interface as a body force. The value of the force is normally a function of the color function. In the current case, we can impose the contact angle in the same manner to the contact line cells. The contact angle is imposed by forcing the vector normal to the liquid-vapor interface to a function of the contact angle as:

$$n = n_w \cos(\theta_w) + t_w \sin(\theta_w) \quad (2.10)$$

where the normal  $n_w$  and  $t_w$  are in the local reference system.

When a liquid film wets a solid wall, an extended meniscus forms (Wang *et al.* [54]). The latter can be divided into three regions: (i) a thin-film, where long range molecular forces are non-negligible (disjoining pressure), (ii) an intrinsic meniscus, dominated by macroscopic capillary forces, and (iii) an adsorbed layer. The thin-film region is of particular importance as it has a very low thermal resistance due to its small size and can lead to a consequent enhancement of the heat transfer. Under condensing conditions, the effect of the thin-film is generally not important unless we reduce the dimension of the problem down to a hundred micrometers. Indeed, it is generally considered that the end of the thin-film region is around a millimeter thick (analytically the end of the thin film region is taken as when the disjoining pressure falls to about a  $1/2000^{th}$  of its value in the non-evaporating region. In the case of condensation, we will neglect the effect of the thin-film region since the very low liquid film thermal resistance will tend to condense the vapor directly and a thick liquid film will almost always be there (unless it is sheared by a gas for example). In the case of an evaporating annular flow, a thin film region is likely to form during the formation of dry patches, leading to the enhancement of heat transfer at the three zone line. It is therefore modeled in the upcoming section.

The axial shear stress at the liquid-vapor interface is modeled using a modified expression of the single phase expression adopted by Wang and Rose [57] and Nebuloni and Thome [32] where the relative velocity of the two phases is taken into account. For instance when the vapor velocity is much greater than the liquid film velocity, the axial shear stress reduces to the original. With the relative velocity

given by:

$$U_i = U_v - v_{l,\delta} \quad (2.11)$$

where  $U_v$  is the mean vapor velocity and  $v_{l,\delta}$  the liquid film velocity, the interfacial shear stress is given by:

$$\tau^i = \frac{1}{2} C_f \rho_v U_i^2 \quad (2.12)$$

where the friction coefficient is given by Churchill formula [10] as:

$$C_f = \frac{\phi}{e^\phi - 1} C_{f,v} \quad (2.13a)$$

$$\phi = -\frac{2J^c}{C_{f,v} \rho_v U_{v,r}} \quad (2.13b)$$

$$C_{f,v} = 2 \left[ \left( \frac{8}{Re_{v,r}} \right)^{12} + \frac{1}{(A+B)^{3/2}} \right]^{1/12} \quad (2.13c)$$

$$A = \left[ -4\sqrt{2} \log_{10} \left( \frac{6.9}{Re_{v,r}} \right)^{0.9} \right]^{16} \quad (2.13d)$$

$$B = \left( \frac{37530}{Re_{v,r}} \right) \quad (2.13e)$$

where the  $\phi$  is the correction term for the suction effect arising from the condensation process. The interfacial friction coefficient described in Eq. 2.13 stands the the laminar liquid films assumption. In the case of a turbulent liquid film, the interfacial friction factor is replaced by the empirical correlation of Cioncolini and Thome [12] which takes into account the liquid film thicknes and is function of the vapor core Weber number as explained later.

### Definition of the minimum thickness and thin film region

The transition from a macroscopic liquid film to a dry patch has been subject of a heated debate among scientists and has not yet been mathematically solved. It is well established that the extended meniscus can be divided into three regions: (i) an intrinsic meniscus connected to the macroscopic film, (ii) a thin-film region with very high heat transfer rates and (iii) a non-evaporating film where the Van-der-Walls forces prevent evaporation. The length of the non-evaporating region is often extended all over the dry patch, assuming a nanometer thick layer of liquid film remains over previously wet regions. However, some authors (Rednikov and Colinet [41]) suggest the film can have a terminal "pancake" style shape depending on the physical properties of the liquid, vapor and wall. We assume here an extended microfilm approach and follow the procedure described by Wang *et al.* [54] to mathematically describe the thin film region. The augmented Laplace equations providing the pressure difference between the vapor and the liquid, is given by:

$$P_v = P_l + P_c + P_d \quad (2.14)$$

In the non-evaporating region, the disjoining pressure  $P_d$  dominates and is given by  $\frac{A}{\delta^3}$ , where  $A$  is the Hamaker constant. Assuming the lubrication assumption holds in the thin-film region, a third order

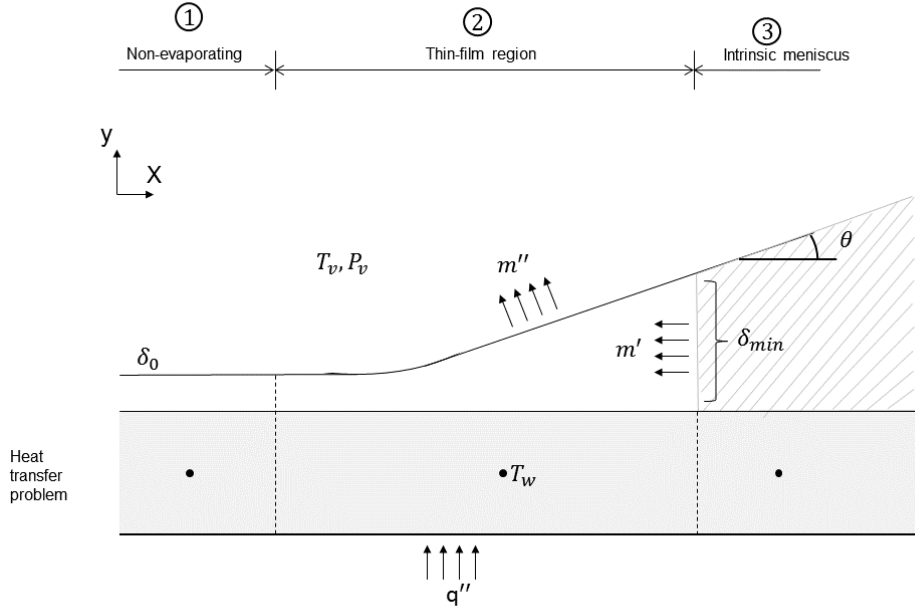


Figure 2.2: Three phase line transition, intrinsic meniscus, thin-film region and non-evaporating region

differential equation can be obtained to describe the thin-film profile:

$$\frac{d}{dx} \left[ \left( \frac{\sigma \delta'''}{(1 + \delta'^2)^{1.5}} - \frac{3\sigma \delta' \delta''^2}{(1 + \delta'^2)^{2.5}} - \frac{3A\delta'}{\delta^4} \right) \frac{\delta^3}{3\nu} \right] = -m'' \quad (2.15)$$

where the evaporative flux is given by Wayner et al. [58] as:

$$m'' = a(T_{lv} - T_v) - b(P_d + P_c) \quad (2.16a)$$

$$\text{with } a = \left( \frac{M}{2\pi RT_{lv}} \right)^{1/2} \frac{P_v M h_{lv}}{RT_v T_{lv}}, \quad (2.16b)$$

$$b = C \left( \frac{M}{2\pi RT_{lv}} \right)^{1/2} \frac{V_l P_v}{RT_{lv}} \quad (2.16c)$$

Setting the evaporative flux  $m''$  to 0 lets us obtain the liquid film thickness in the non-evaporative region as:

$$\delta_0 = \left( \frac{bA}{a(T_w - T_v)} \right)^{1/3} \quad (2.17)$$

and therefore the disjoining pressure in the non-evaporative region  $P_{d0} = A/\delta_0^3$ . It is often assumed that the end of the thin-film region occurs when the disjoining pressure drops to  $1/2000^{th}$  of the non-evaporative region disjoining pressure  $P_{d0}$ . This allows us to calculate the local minimum thickness:

$$\delta_{lim} = (2000P_{d0}A)^{1/3} \quad (2.18)$$

It is important to notice that this limit thickness  $\delta_{lim}$  is calculated locally at each cell and allows the code to identify wet, transition and dry zones, where transition zones are cells with contact lines in them. Compared to most numerical codes, the transition from a wet to a dry zone is hence not calculated with some arbitrary constant. Other approaches consisted in taking the wall roughness as the transition criteria from a wet to a dry zone (see Thome *et al.* [51]). While the latter approach provides some fairly good results, it has not been proven yet how the wall roughness would affect the contact line dynamics. It is worth noting as well that the wall roughness is often around the same order of magnitude as the end of the thin-film region. Using Eq. 2.15 and Eq. 2.16 and integrating over the whole thin film region, we are able to obtain the total heat flux as:

$$q_{j,k}^{tf} = \sqrt{\frac{2Ah_{lv}h_{fg}(T_{j,k}^w - T_k^v)}{\nu}} \ln\left(\frac{\delta}{\delta_0} \frac{1 + C_2\delta_0}{1 + C_2\delta}\right) \quad (2.19)$$

The evaporative mass flux integrated over the thin film region is obtain by conservation of mass and the cross sectional mass flux in the liquid film:

$$m''_{total,j,k} = m'(x_{lim}) = \frac{q_t}{h_{fg}} \quad (2.20)$$

Once the contact line is reconstructed following the procedure described in the upcoming section, the total evaporative and heat flux in the thin film region can be added to contact line cells.

### Modeling the contact line

An interface tracking method is introduced in the domain decomposition in order to allow for appearance of dry patches on the channel walls during evaporation. The tracking method is similar to the color function methods found in standard CFD codes where the liquid phase and vapor phase are characterized by a color function that is equal to 1 when the phase in the selected cell is vapor and 0 when the phase in the selected cell is liquid. In the transition region, namely the three-phase line, the color function can take any value between 0 and 1 depending on the calculated ratio of vapor to liquid volumes. It is proposed here to adapt the color function to the arbitrary mesh that was developed to handle annular flows. The resolution of the contact line requires the following steps:

- the identification of "dry" versus "wet walls" using a color function approach
- the selection of static, advancing and receding contact angles
- the addition of the contact angle influence using a body force approach
- the choice of the minimum acceptable film thickness solving a simplified model of the thin film region
- the addition of the thin film region high evaporative rates and high heat fluxes

Modeling the contact line dynamics is a difficult task in CFD due to the shear stress singularity arising at the three phase line. Different approaches have been proposed that rely on empirical evaluations of the static, advancing and receding contact angles. In the present study, we will follow an approach largely used in standard CFD that consists in tracking the contact line motion with the use of a color function. While generally the numerical grid covers all the domain and the color function is implemented on all cells, in the current case we only implement a color function on the liquid film grid. Therefore, the vapor core axial discretization will remain the same as when no dry patch occurs, while the initial liquid film grid that was developed for fully wetting annular flow will now "experience" cells that are liquid, vapor and contact line. Such an approach is followed in order to be able to track the contact line using the color function approach. The procedure followed can be summarized in the following steps:

1. Identify wet, vapor and transition cells
2. Calculate velocity of contact line
3. Calculate vapor-liquid volume fraction from the calculated contact angle
4. Update the contact angle and contact line position.

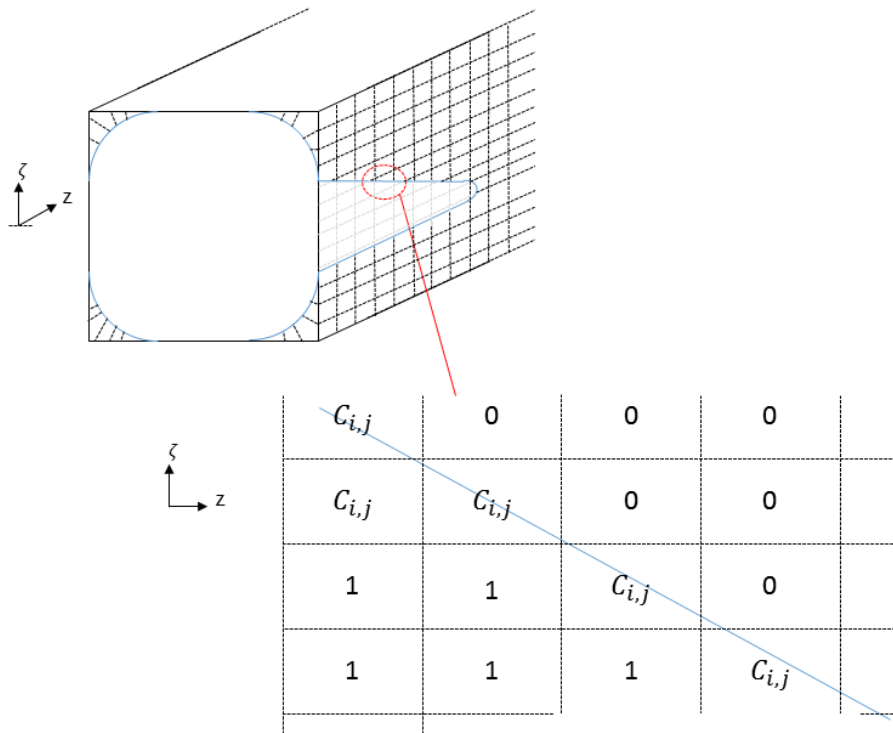


Figure 2.3: Dry patch identification

Wet and dry zones are identified by means of a color function, an approach widely used in CFD. Firstly, Fig. 2.3 shows a conceptual 2D representation of thin film identification region procedure. The dry cells are identified by a color function  $C$  with a value 0 while fully wet cells are identified with a color

function  $C = 1$ . In the transition region, the color function can take any value between 0 and 1 and is defined by the ratio of the volume of vapor over volume of liquid in the selected cell:

$$C_{i,j} = \frac{V_v^{i,j}}{V_l^{i,j}} \quad (2.21)$$

When the cells (liquid film) are thicker than the limit defined in Eq. 2.18, the value of the color function is obviously 0. However, in order to model the transition and contact line, we develop an approach where a virtual hexaedral cell, with a thickness defined by Eq. 2.18 is used to identify the ratio of vapor to liquid. In Fig. 2.4, a virtual control volume  $\Omega_v$  overlaps the arbitrary control volume  $\Omega_{i,j}$  defined

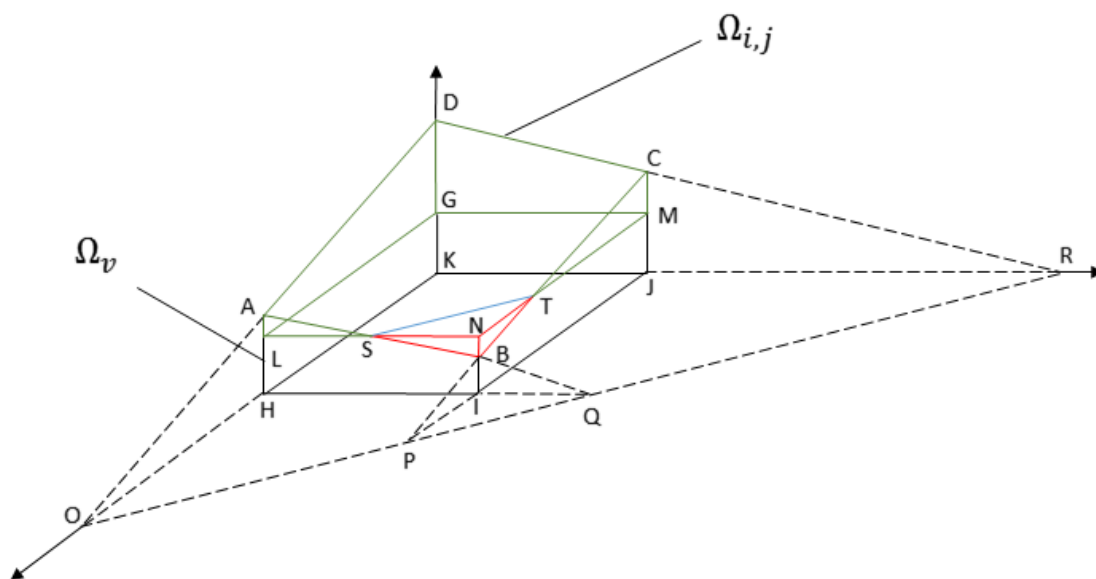


Figure 2.4: Vapor to liquid volume ratio identification

earlier and that discretizes the liquid film. The tetrahedron  $SNBT$  represents the virtual vapor volume, while the hexahedron  $DABCJKHI$  represents the complete control volume. The ratio of the latter provides the value of the color function. The plane liquid-vapor interface, shown by the plane  $DANC$  in Fig. 2.4 intersects with the plane  $MGLN$  at the three phase line. The ratio of the volumes can geometrically be calculated by extending the control volume  $DABCJKHI$  with the three hexahedrons  $AOQH$ ,  $CRPJ$  and  $IPQB$ . The calculation procedure and different situations that is found is provided in Appemdix. A. The identification of the normal vector to the plane  $DANC$  can be calculated from the liquid-vapor interface curvature in the case when no dry patch exists, but is obtained by solving the contact angle problem in the case of a liquid to dry cell. The equation of the plane  $ADCB$  is given as a function of the normal vector to the plane:

$$m_1 x_1 + m_2 x_2 + m_3 x_3 = \alpha \quad (2.22)$$



where  $[m1, m2, m3]$  are the coordinates of the normal vector to the plane, imposed by the calculated contact angle,  $\alpha$  is the minimum distance to the reference point in Fig. 2.4. The static contact angle can be obtained from the Young's equation given by:

$$\sigma_{LG}\cos\theta_s = \sigma_{GS} - \sigma_{LS} \quad (2.23)$$

where  $\sigma_{LG}, \sigma_{GS}, \sigma_{LS}$  are respectively the liquid-gas, gas-solid and liquid-solid surface tensions. The advancing and receding contact angles can be obtained from the Tanner's law ([49]) and from Jiang *et al.* [26]:

$$\sigma_{rec,s}^3 - \sigma_R^3 = 72Ca \quad (2.24)$$

and

$$\frac{\cos\sigma_{adv,s} - \cos\sigma_A}{\cos\sigma_{adv,s} + 1} = \tanh(4.96Ca^{0.702}) \quad (2.25)$$

where  $Ca$  is the capillary number defined as  $Ca = \frac{\mu v}{\sigma}$ . The contact line velocity is calculated from the position of the contact line at previous steps. The advancing and receding contact angles provide the lower and upper limits of the contact angle value. The value of the dynamic contact angle needs to be numerically evaluated by solving the equation connecting the color function to find its value. Furthermore, the evolution of the contact line in time can be computed solving the advection equation: Furthermore, the evolution of the contact line in time can be computed solving the advection equation:

$$\frac{\partial C}{\partial t} + u \cdot \nabla C = 0 \quad (2.26)$$

which will give the velocity of the contact line and hence the new contact angle.

### 2.1.5 Turbulent liquid film

The liquid film so far was assumed to be laminar, thus limiting the applicability range to low mass fluxes and small channel diameters. As such, an extension is proposed here to handle industrially realistic cases where turbulence is typically the norm. However, the transition from laminar to turbulent shear flow is not so obvious in film flows and has been a topic of debate for a long time. There is currently little consensus on a physically based transition from a laminar to a fully turbulent state of a film flow and the dependence of the latter on the local liquid film Reynolds number might also vary from one geometry to another and be a function of the hydraulic diameter. As such, the problem was tackled here in the same pragmatic manner assumed above and with the objective of reducing the computational cost.

Cioncolini and Thome [12] developed an algebraic model for annular flows based on a large set of experimental data. Assuming that the liquid film is shear dominated, a model was developed for the turbulent eddy diffusivity for momentum and for heat. Far from assuming these correlations capture the onset of instabilities in the liquid film and the transition to the fully turbulent state, they do provide however a pragmatic approach to model the influence of turbulence from experimental results. Of course, the turbulent eddy diffusivity will as well include the effects of interface instabilities

and wave patterns on the liquid film interface. In order to capture when the turbulence for heat and momentum is physically active, these authors [12] came up with a transition criterion based on the dimensionless film thickness and do not need the liquid film velocity profile. The turbulent eddy diffusivity for momentum is given by:

$$1 + \nu_t^+ = \left(1 + (0.033t^+)^8\right)^{\frac{1}{8}} \quad \text{for } 1 \leq t^+ \leq 300 \quad (2.27)$$

The turbulent eddy diffusivity is given by means of dimensionless liquid film thickness:

$$1 + \alpha_t^+ = \left(1 + (77.6e^{-3}t^{+0.9}Pr_l^{-0.52})^8\right)^{\frac{1}{8}} \quad (2.28)$$

$$\text{for } 0 \leq t^+ \leq 800 \quad \text{and} \quad 0.86 \leq Pr_l \leq 6.1 \quad (2.29)$$

where  $\nu_t^+$  and  $\alpha_t^+$  are defined as:

$$\begin{aligned} \nu_t^+ &= \frac{\mu_t}{\mu_l} \\ \alpha_t^+ &= \frac{k_t}{k_l} \end{aligned} \quad (2.30)$$

The dimensionless liquid film thickness  $t^+$  can be obtained for the liquid film as:

$$\begin{aligned} t^+ &= \frac{t}{y^*} \\ y^* &= \frac{\mu_l}{\rho_l V^*} \\ V^* &= \sqrt{\frac{\tau_w}{\rho_l}} \end{aligned} \quad (2.31)$$

where the wall shear stress, calculated from the lubrication theory in the case of a laminar liquid film, is here calculated using an empirical friction factor correlation of a shear driven flow given by Cioncolini and Thome [13]:

$$f_{tp} = 0.0196We^{-0.372}Re_l^{0.318} \quad (2.32)$$

$$We_v = \frac{\rho_v U_v^2 Dh_v}{\sigma} \quad (2.33)$$

where the vapor core Weber number describes the shear exerted by the vapor over the liquid film. The Reynolds number provided is the local liquid film Reynolds number calculated when solving the mass and momentum equations. A detailed description on how the momentum and cross momentum fluxes are calculated is provided in Appendix B. It is interesting to notice the lower limits for the eddy diffusivity for heat and momentum. For instance, the eddy diffusivity for heat becomes "active" at a dimensionless thickness of 10. Considering that in our case, then the problem solved is a simple 1D conduction problem across the liquid film when it is smaller than this, and it can be stated that the turbulence intensity may have a significant impact on the microchannel thermal performance. The interfacial friction factor  $f_{tp}$  is injected in the interfacial shear stress Eq. 2.12, thus taking into

account the liquid film thickness and the shearing of the vapor core on the liquid film. The transition from a laminar liquid film to turbulent liquid film is subject to debate among scientists. Standard CFD approaches generally activate the turbulence models and the transition is hence rather arbitrary, meaning that without proper experimental comparison it is difficult to predict the liquid film behavior in the transition state that may happen, depending on the geometry and hydraulic diameter, for a mass velocity anywhere between 200 and 500  $kg/m^2 s$ . Adding further complexity, the channel geometry plays an important role in small channels due to the role of surface tension. In the current case, we use a model that was initially developed for a circular geometry where the liquid film was assumed uniform across the circumference of the channel. The model, for instance, was fitted with a large database containing mainly circular channels with larger hydraulic diameters than the ones being dealt with here. Yet, the correlations obtained in Eq. 2.27 and Eq. 2.29 are function of the dimensionless liquid film thickness. In the present code, the dimensionless liquid film thickness is calculated locally and hence we are able to use a model initially developed for a uniform liquid film thickness for a non-uniform liquid film thickness. The transition from a laminar liquid film to a turbulent liquid film is not given by any arbitrary film thickness constant or threshold but depicts when the turbulence has or does not have an influence on the overall heat transfer coefficient and pressure drop. This influence is obtained from a comparison with the large experimental database provided in Cioncolini and Thome [13]. Unfortunately, the database provided by the latter authors considers channels from 1 to 10  $mm$ , that are larger than the ones being simulated here, we could hence not fine tune the model with a database composed of channels with smaller hydraulic diameters.



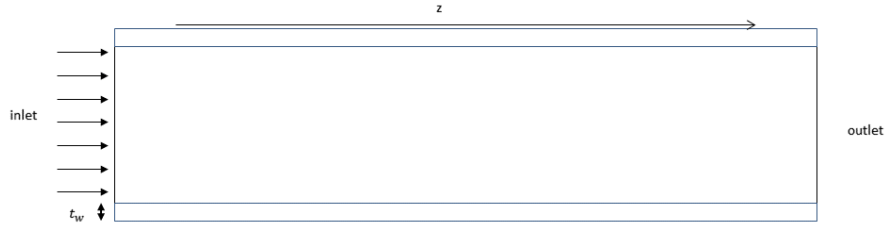
## 3 Hybrid 1D/3D model for bubble nucleation, slug flow and elongated bubbles

Most common condensation applications are for complete condensation of the incoming vapor to a fully liquid state at the outlet. As such, the vapor qualities covered generally go from 1 to 0. However, in evaporation, annular flows are rather interesting to model in order to understand the dryout process and therefore avoid entering the region at high vapor qualities in order to avoid failure of the device due to a rise in temperature above the functioning temperature. Therefore, most practical evaporative applications will tend to keep a high security margin and keep the operating conditions in the low to medium vapor quality range. At low vapor qualities in evaporating fluids, this thus includes the nucleation process as well as the bubble/slug flow and will lead to a substantial increase in heat transfer coefficient compared to subcooled single phase liquid. The current chapter describes the approach used to model nucleation and slug/elongated bubble flows in order to cover the low vapor quality range. The approach focuses on modeling the wall conduction behavior while the bubbles and liquid slug pairs are modeled using a simplified 1D discretization approach, including available correlations from the literature. A similar modeling approach was carried out also by Consolini and Thome [17] for modeling elongated bubble evaporation in the isolated bubble, coalescing bubble regime. Modeling convective boiling at such low vapor qualities has a fundamental importance as it covers most of the operating conditions in microevaporators today.

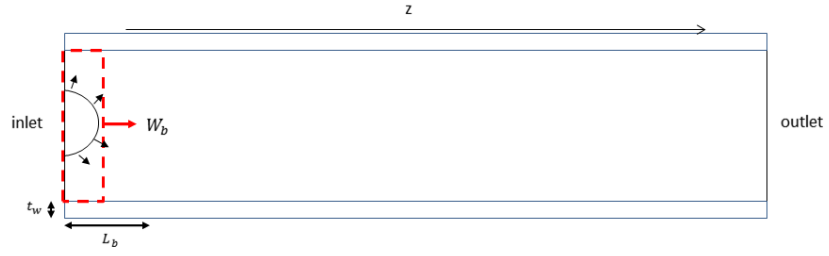
### 3.0.6 Mathematical model

The approach initiated by Thome et al. [51] to describe the behavior of liquid slugs and elongated bubbles in single microchannels using a conceptual three zone division, has been subsequently used in a large variety of studies. In the current study, we used the same conceptual division of the flow domain but include the effect of wall conduction and importantly provides a framework for adapting the liquid film to different cross-sectional geometries of the microchannel. In addition, the effect of wall nucleation on the wall thermal balance is also taken into account. This chapter hence provides a natural continuity to the annular flow model described above and hence allows engineers to cover a larger range of vapor qualities for both evaporation and condensation.

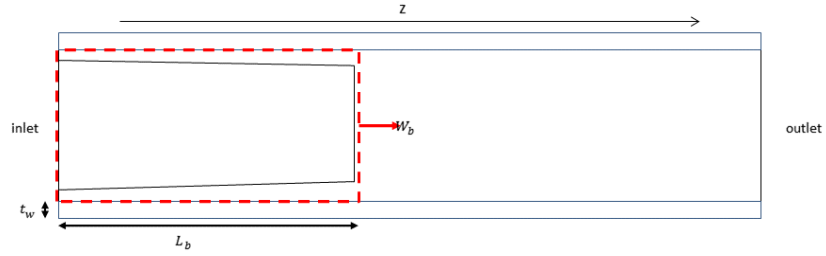
The coordinate system used for the spatial discretization follows the mesh created for the annular flow regime, where the inner channel wall behaves as a boundary condition for the energy equation. Again, the modeling of the slug flow and bubble behavior will be coupled with the energy equation at the wall through a boundary condition.



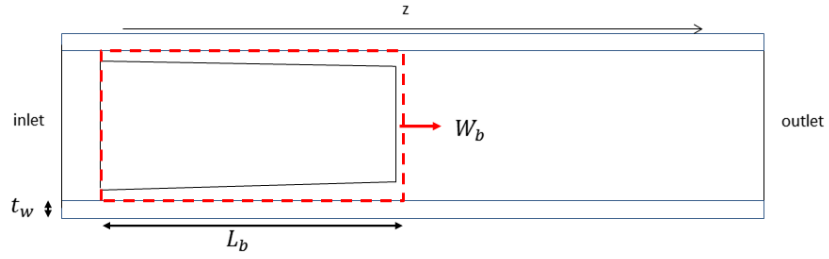
(a) Single phase liquid



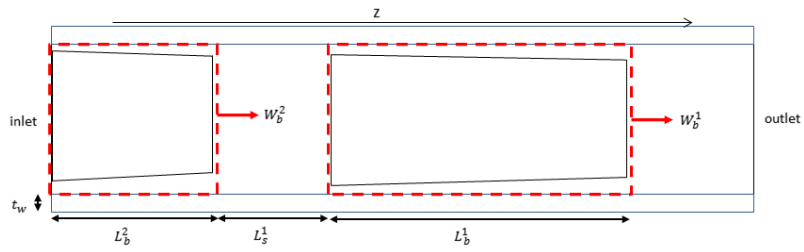
(b) Single phase liquid



(c) Bubble nucleation



(d) Bubble growth



(e) Bubble detachment

Figure 3.1: Bubble nucleation and growth process]

The key assumptions of this model are:

- Flow at constant saturation temperature except for the liquid film resolution

- Bubble velocity governed by thin film evaporation and inlet mass velocity
- No dry patch formation at the end of the bubble. The minimum thickness is imposed as in Eq. 2.18.
- Little influence of the liquid slug on heat transfer

### Energy equation

The energy equation at the wall considers the flow of refrigerant as a time dependent boundary condition and is given by:

$$\rho C_{p,w} \lambda_w \frac{\partial T(t)}{\partial t} + k_w \lambda_w \nabla \cdot T(t) = \dot{Q} + \dot{Q}_{\partial\Omega_{int}}(t, T_w, T_l) \quad (3.1)$$

where the internal boundary heat flux condition depends on the flow characteristics and is time dependent. The focus here is hence put on the conduction at the wall while the bubbles/liquid slugs are modeled using a simple approach proposed in the works of Thome *et al.* [51] and Consolini and Thome [16].

### Bubble and liquid slug model

The creation, detachment and flowing of an elongated bubble is divided into 5 different steps as shown in Fig. 3.1 that will be modeled accordingly:

1. Single phase fluid flowing in microchannel
2. Nucleation of a bubble at the inlet of the microchannel
3. The bubble reaches the hydraulic diameter and begins to elongate axially
4. The bubble flows downstream
5. A new bubble nucleates.

During step 1, single phase refrigerant flows through the channel and is heated by the imposed heat flux at the wall, with the refrigerant temperature increasing as it heads downstream towards the outlet of the channel. In the present case, we assume nucleation is controlled and triggered at the inlet of the channel, for instance through a pre-heater to bring the inlet temperature to saturation or an inlet orifice that would create a small pressure drop, bringing the refrigerant pressure below the saturation pressure. In a later stage, we propose to allow the triggering of nucleation upstream of the diabatic section, leading to different heat transfers at low vapor qualities. Once the nucleation process starts, the bubble grows radially and the vapor occupies a certain volume of the inlet cells. Once the bubble reaches the wall, it starts growing axially, followed by a thin liquid film between the growing bubble and the channel inner wall. The bubble will then detach from the inlet of the channel and flow downstream, creating a liquid slug until the next bubble appears. As it flows downstream,

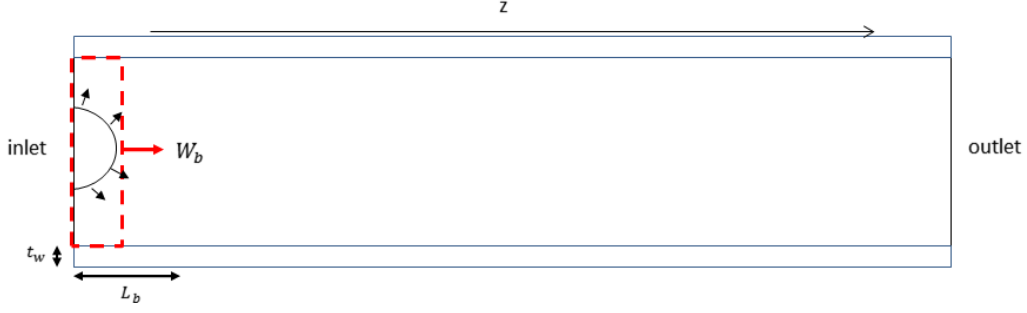


Figure 3.2: Bubble nucleation

the bubble elongates and eventually coalesces with the next bubble. The boundary heat flux is then reconstructed based on the phases mentioned above.

The wall temperature is initialized by using a simple Dittus-Boelter equation to model the heat transfer behavior at the wall-liquid interface. A simple energy balance provides the liquid bulk temperature variation while the maximum temperature is below the saturation temperature.

### Bubble nucleation

We later assume nucleation occurs at the inlet of the channel when the inlet temperature reaches the saturation temperature. In this case, the liquid downstream of the inlet of the channel is therefore superheated but it is assumed that no nucleation occurs on the inner walls of the microchannel. This assumption is likely to be questioned in the case of rough surface or liquids with impurities. During the initial stage of the nucleation process, we consider the bubble grows in the uniformly superheated liquid with a bubble growth rate given by the Plesset and Zwick [38] model:

$$r(t) = Ja \sqrt{\frac{12\alpha_l t}{\pi}} \text{ with } Ja = \frac{\rho_l c_{pl}}{\rho_v \Delta h_{lv}} \Delta T_{sup} \quad (3.2)$$

where the superheat  $\Delta T_{sup}$  can either be imposed (to control the growth speed) or by taking the wall temperature as a reference  $\Delta T_{sup} = T_{wall} - T_{sat}$ . The nucleation model of Plesset and Zwick [38] is used for the sake of simplicity. Other models that take into account wall superheat are not used due to the difficulty to characterize the location of the nucleation sites on the wall. As the bubble nucleates and grows uniformly at the inlet of the channel, it begins to elongate as soon as its diameter reaches the hydraulic diameter of the channel.

As the bubble grows, an arbitrary control volume  $\Omega_{CV}^k$  (the superscript k denotes the  $k^{th}$  bubble) is created as shown in Fig. 3.2. The advancing boundary at  $z_N(t)$  is, during the nucleation process, governed by the bubble growth rate (as in Fig. 3.1). The tail of the control volume  $\Omega_{CV}^k$  is initially taken as the inlet of the microchannel and then, in the elongated bubble regime, as the back of the bubble at a position  $z_B(t)$ . The volume occupied by the bubble is calculated assuming a spherical growth until it reaches one of the walls. In such a manner, we are able to track the volume occupied by the bubble in the arbitrarily shaped control volume.

Initially, we assume the bubble grows radially and that the forces exerted by the flow are not large enough to pull the nucleating bubble downwards. Fig. 3.2 shows that while the bubble is growing in the superheated liquid, single phase flow liquid will surround the bubble, increasing the local velocity



of the liquid and enhancing the convective contribution of the heat transfer coefficient. In order to model the initial stages of bubble growth, we assume the following:

- The bubble detaches only when it reaches a radius of  $\frac{D_h}{2}$  as mentioned by Thome *et al.* [51]
- Until detachment, the single phase liquid surrounds the bubble
- The integral of the interface mass transfer from the liquid to the vapor is assumed to be negligible with respect to the single phase mass flux
- Bubble nucleation is assumed to cause no temperature change on the surrounding fluid and all the latent heat is coming from the superheated wall
- The bubble remains at saturation temperature
- The inner boundary heat transfer coefficient is reconstructed from the convective contribution of the single phase liquid flow and the latent heat contribution of the nucleation process.

A correlation for modeling the convective contribution when the bubble nucleates is proposed here as a ratio with respect to the single phase flow correlation. While we know the bubble growth rate of the bubble from Eq. 3.2, we can calculate the ratio of vapor to liquid volume in the control volume as follows:

$$C(t) = \frac{V_{bubble}(t)}{V_{liquid}} = \frac{\frac{4}{3}\pi r(t)^3}{AL(t)} = \frac{\frac{4}{3}\pi r(t)^2}{A} \quad (3.3)$$

where  $r(t)$  is the bubble radius,  $A$  is the cross sectional area of the inner channel and  $L(t) = r(t)$  is the length of the control volume. When the single phase flow is in a turbulent state, the correlation of Dittus and Boelter is used to model the Nusselt number, while a constant value of the Nusselt number is used for the laminar case:

$$Nu_{conv,turb} = 0.023 Re_L^{4/5} Pr_l^{0.4} \quad (3.4)$$

$$Nu_{conv,lam} = 4.36 \quad (3.5)$$

While for a single phase liquid flowing in a channel, the characteristic length for computing the liquid Reynolds number is  $D_h$ , we assume that when the bubble grows, a local characteristic length can be defined based on the distance between the liquid-vapor interface and the channel wall. As such, a modified heat transfer coefficient can be derived with regards to the plain tube single phase flow coefficient:

$$r_{nucleation}(t) = \frac{\alpha_{tp}(t)}{\alpha_{sp}} \quad (3.6)$$

where  $\alpha_{tp}$  is the modified heat transfer coefficient, taking  $\frac{D_h}{2} - r(t)$  as the characteristic distance for the Reynolds number, and  $\alpha_{sp}$  is the plain tube heat transfer coefficient. The latter is calculated assuming that when the bubble grows, the single phase liquid flow surrounds the bubble and taking

the characteristic length for the Nusselt number as the distance between the wall and the vapor-liquid interface, we are able to obtain the ratio  $r_{nucleation}(t)$  as:

$$r_{nucleation}(t) = \left[ \frac{D_h - r(t)}{D_h} \right] \left[ \frac{\pi((D_h/2)^2 - r(t))^2}{A\rho_l} \right]^{0.8} \quad (3.7)$$

The convective contribution of the flow to the heat transfer when a bubble nucleates can therefore be derived as a function of  $r(t)$ :

$$\alpha_{tp} = r_{nucleation}\alpha_{sp} \quad (3.8)$$

Furthermore, as the bubble grows, latent heat is transferred from the surrounding fluid to the saturated vapor. As mentioned earlier, we assume the latent heat comes from the superheated wall and can be integrated into the inner boundary energy equation Eq. 3.1. Considering a spherical bubble of radius  $r(t)$ , the heat transferred through the interface can be depicted as:

$$\dot{Q}_{\partial\Omega_b} = \Delta h_{lv} J^e \quad (3.9)$$

where  $\Delta h_{lv}$  is the latent heat,  $A_b$  the area of the bubble liquid-vapor interface  $\partial\Omega_b$  and  $J^e$  the mass transfer per unit time through the vapor-liquid interface. Knowing the growth rate of the bubble from Eq. 3.2 and performing an energy balance over the control volume  $\Omega_{CV}$ , the heat transferred from the wall can be obtained for the control volume  $\Omega_{CV}$ :

$$\dot{Q}_{\partial\Omega_{int}} = 2\rho_v\pi r(t)^2 \dot{r}(t) \Delta h_{lv} \frac{A_{\partial\Omega_{int}}}{A_b} \quad (3.10)$$

where the bubble vapor-liquid interface area and control volume  $\partial\Omega_{int}^k$  wall-liquid area are given by:

$$A_b = 4\pi r(t)^2 \quad (3.11)$$

$$A_{\partial\Omega_{int}} = P_{CV} r(t) \quad (3.12)$$

$$(3.13)$$

where  $P_{CV}$  is the control volume perimeter, or perimeter of the microchannel cross section.

### Bubble detachment and growth

Once the bubble radius reaches  $Dh/2$ , the bubble detaches and flows downstream. Let us consider  $z_N(t)$  as the position of the bubble nose from now on. During the transition between the nucleation regime and detachment, the bubble radius equals the position of the bubble front  $r^{max} = z_N^0$ . From this stage, we assume each bubble to be composed of an advancing semi-spherical front with fixed radius  $r^{max}$  and an elongating cylinder. The key assumptions for the calculation of the bubble growth are:

- Heat transfer and evaporation through the thin film is the dominant origin for bubble growth
- The bubble front speed is a function of the liquid velocity and bubble expansion
- A 1D liquid film evaporation is solved to model the wall to vapor conjugate heat transfer

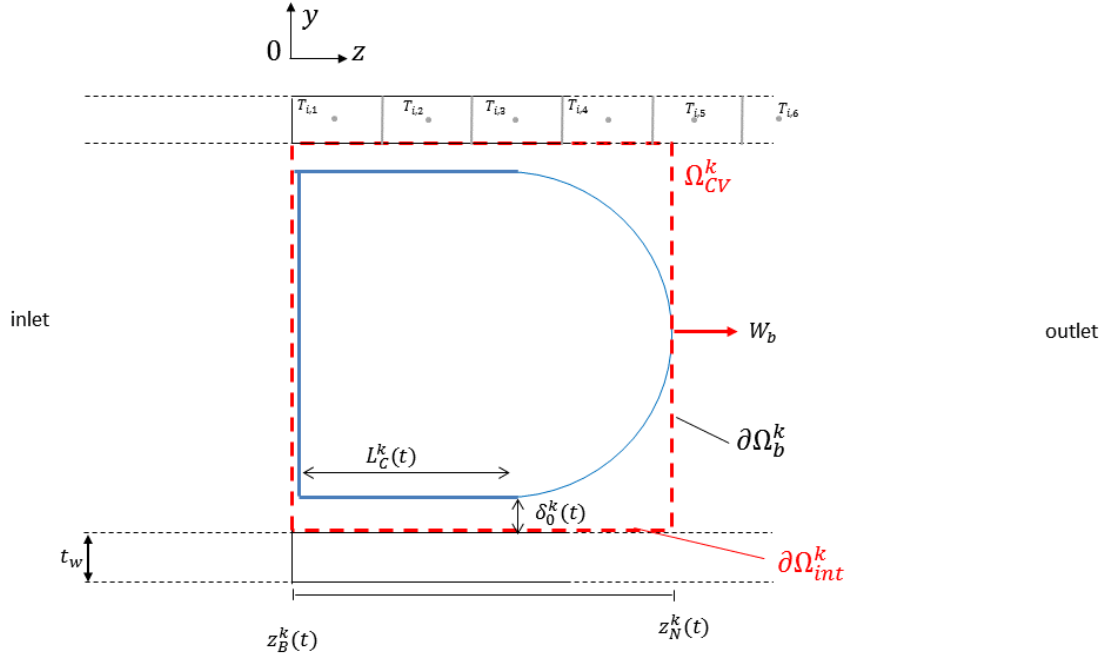


Figure 3.3: Bubble Elongation

- The initial liquid film thickness of the thin film at the bubble nose is calculated empirically

The velocity of the moving boundary  $W_N = \frac{dz_N}{dt}$  can be obtained in a similar manner as in Consolini and Thome [17] through a mass balance over the bubble:

$$W_N = \frac{G}{\rho_l} + \left(1 - \frac{\rho_v}{\rho_l}\right) \frac{1}{A_c} \frac{dV_v}{dt} \quad (3.14)$$

where  $\frac{dV_v}{dt}$  is the derivative of the bubble volume with time solved by integrating the liquid film evaporation and  $A_c = \frac{4}{\pi D_h^2}$  is the channel cross sectional area (assuming the liquid film is very thin compared to the diameter). The first term on the right hand side of Eq. 3.14 is the speed of the entering fluid in the microchannel and the second term is the expansion due to phase-change. Since thin film evaporation is the dominant mode of mass supply to the bubble, the derivative of the bubble volume can be given by:

$$\frac{dV_v}{dt} = A_c \frac{d}{dt} [\pi D_h (z_N(t) - z_0(t))] = \frac{\pi D_h}{\rho_v} \int_{z_B(t)}^{z_N(t)} J^e(z) dz \quad (3.15)$$

Considering the mass and momentum equation of a shear driven liquid film, we can obtain the governing equation for the liquid film thickness to be:

$$\frac{\partial \delta}{\partial t} + \frac{\tau_i}{\mu_l} \delta \frac{\partial \delta}{\partial z} = \frac{J^e}{\rho_l} = \frac{1}{\rho_l} \frac{\phi(\delta) + J_T}{\phi(\delta) J_T} (T^s - T^w) \quad (3.16)$$

where  $\tau_i$  is the shear stress exerted by the vapor on the liquid and calculated in the same manner as for the annular model. The parameter  $\phi$  is given by:

$$\phi = \frac{k_l}{\delta h_{lv}} \quad (3.17)$$

Eq. 3.16 requires the film thickness at the front of the bubble, which is selected from the modified correlation of Thome *et al.* [51] and Dupont *et al.* [23]:

$$\frac{\delta_0}{D_h} = C_{\delta_0} \left( 3 \sqrt{\frac{v_l}{W_N D_h}} \right)^{0.84} \left( (0.07 Bo(\delta))^{0.41} - 8 + 0.1^8 \right)^{-1/8} \quad (3.18)$$

where the velocity of the bubble front is  $W_N$  and  $C_{\delta_0}$  is a parameter selected from the database provided by Dupont *et al.* [16]. The Bond number is a function of the nose velocity and given by:

$$Bo = \frac{\rho_l D_h}{\sigma} W_N^2 \quad (3.19)$$

### Liquid slug and consecutive bubbles

When the first bubble flows downstream, frequency of pair generation is given as in Thome *et al.* [51] by:

$$f = 1/\tau = \left[ \frac{2\rho_l c_{pl} \Delta T_{sat}}{\rho_v h_{lv} D_h} \right] \frac{12\alpha_l}{\pi} \quad (3.20)$$

where the superheat can either be imposed (in order to fix a certain frequency) or linked to the wall temperature. Knowing the frequency of bubble nucleation, speed of the front bubble and volume of the front bubble, we are able to determine the initial length of the liquid slug.

The liquid slug forming between two consecutive bubbles is modeled using the correlation of London and Shah for laminar flows (see VDI [46]) and the Gnielinski (see VDI [46]) correlation for turbulent flows:

$$Nu_{lam} = 0.455(Pr)^{1/3} \left( \frac{D_h Re}{L_{slug}} \right)^{1/2} \quad (3.21)$$

$$Nu_{turb} = \frac{(\xi/8)(Re - 1000)Pr}{1 + 12.7\sqrt{\xi/8}(Pr^{2/3} - 1)} \left[ 1 + \frac{1}{3} \left( \frac{D_h}{L_{slug}} \right)^{2/3} \right] \quad (3.22)$$

$$\text{with } \xi = (1.82 \log_{10} Re - 1.64)^{-2} \quad (3.23)$$

Once more than one bubble is flowing in the channel, the liquid slug trapped between two bubbles will see this volume change based on the growth of the bubble. As such, the liquid slug length can be defined as:

$$L_{slug}^i(t) = L_{slug}(t_0) + \frac{dL_{cyl}^{i-1}}{dt} \quad (3.24)$$

where  $L_{slug}(t_0)$  is the liquid slug before nucleation of the second bubble. The length of the liquid slug is assumed to be dependent on the volume growth of the following bubble. The boundary heat flux to

be solved in Eq. 3.1 can therefore be reconstructed as:

$$\dot{Q}_{\partial\Omega_{int}}(t, T_w, T_l) = \sum_i^N L_{cyl}^i(t) \alpha(\delta^i, L_{cyl}) + (L - \sum_{cyl}^i L_{cyl}^i(t)) \alpha_{coolant} \quad (3.25)$$

The problem is resolved step by step and the resolution procedure will be explained in the coming chapter.



## 4 Numerical resolution

In the current chapter, the resolution of the annular flow model and bubbly flow model are explained. The resolution of the annular flow and bubbly flow problems are taken separately as two distinct codes due to the different characteristic time scales and complexity of the problems.

When an external heat flux is applied to the annular flow model, we obtain a base set of non-linear differential equations, valid for both condensation and evaporation:

$$\underline{f}(\underline{T}, \underline{\delta}, \underline{q}) = 0 \quad (4.1)$$

$$\dot{\underline{\delta}} - \underline{f}_{\underline{\delta}}(\underline{\delta}, \underline{u}, \underline{v}, \underline{T}) = 0 \quad (4.2)$$

$$\dot{\underline{U}} - \underline{f}_{\underline{U}}(\underline{\delta}, \underline{u}, \underline{v}, \underline{T}) = 0 \quad (4.3)$$

$$\dot{\underline{u}} - \underline{f}_{\underline{u}}(\underline{\delta}, \underline{u}, \underline{v}, \underline{T}) = 0 \quad (4.4)$$

$$\dot{\underline{v}} - \underline{f}_{\underline{v}}(\underline{\delta}, \underline{u}, \underline{v}, \underline{T}, \underline{u}, \underline{p}) = 0 \quad (4.5)$$

$$\dot{\underline{p}} - \underline{f}_{\underline{p}}(\underline{\delta}, \underline{u}, \underline{v}, \underline{T}, \underline{U}, \underline{p}) = 0 \quad (4.6)$$

where the quantities  $\underline{\delta}, \underline{u}, \underline{v}, \underline{T}, \underline{U}, \underline{p}$  are the unknowns of interest, respectively the liquid film thickness, axial and azimuthal velocities, vapor velocity and liquid film pressure. In the case of an evaporating annular flow, the resolution of the contact line motion requires two additional differential equations, namely the advection equation Eq. 2.26 and the resolution of the contact angle :

$$\dot{\underline{C}} - \underline{f}_{\underline{C}}(\underline{C}, \underline{u}, \underline{v}) = 0 \quad (4.7)$$

$$\dot{\underline{\theta}} - \underline{f}_{\underline{\theta}, \underline{\delta}} = 0 \quad (4.8)$$

with given initial conditions:

$$\underline{\delta}_0 = \underline{\delta}_0 \quad (4.9)$$

$$\underline{u}_0 = \underline{u}_0 \quad (4.10)$$

$$\underline{v}_0 = \underline{v}_0 \quad (4.11)$$

$$\underline{C}_0 = 0 \quad (4.12)$$

$$\underline{\theta}_0 = 0 \quad (4.13)$$

and inlet conditions:

$$\underline{\xi}(i, z=0)_0 = \underline{\delta}_i(\xi) \quad (4.14)$$

$$\underline{\xi}(i, z=0)_0 = \underline{u}_i(\xi) \quad (4.15)$$

$$\underline{\xi}(i, z=0)_0 = \underline{v}_i(\xi) \quad (4.16)$$

The initial conditions need to be characterized differently for the evaporating annular flow and the condensing annular flow. Indeed, the initial conditions for condensation are based on the initial vapor quality required by the user, which will tend to be close to 1 (very thin liquid film). For simple geometries, the initial condition generally rarely affects the numerical convergence of the problem, but complicated geometries tend to require running the code in adiabatic conditions beforehand in order to obtain an initial condition closer to the solution. For evaporation, running a preliminary adiabatic case at low vapor qualities is required in order to guarantee the convergence otherwise instabilities arise quickly due primarily to the importance of surface tension forces. Provided that the problem is stiff due to the numerous time scales (contact line motion, surface tension etc), an implicit method needs to be used in order to solve the problem. An approach already proposed by Nebuloni and Thome [32] can be used in the current situation. It consists in an approximation of the equations in time using a backward Euler method [40]:

$$\underline{f}(\underline{T}^{\Delta t+t}, \underline{\delta}^{\Delta t+t}, \underline{q}^{\Delta t+t}) = 0 \quad (4.17)$$

$$\underline{\delta}^{\Delta t+t} - \underline{\delta}^t - \underline{f}_{\delta}(\underline{\delta}^{\Delta t+t}, \underline{u}^{\Delta t+t}, \underline{v}^{\Delta t+t}, \underline{T}) = 0 \quad (4.18)$$

$$\underline{U}^{\Delta t+t} - \underline{U}^t - \underline{f}_U(\underline{\delta}, \underline{u}^{\Delta t+t}, \underline{v}^{\Delta t+t}, \underline{T}^{\Delta t+t}) = 0 \quad (4.19)$$

$$\underline{u}^{\Delta t+t} - \underline{u}^t - \underline{f}_u(\underline{\delta}^{\Delta t+t}, \underline{u}^{\Delta t+t}, \underline{v}^{\Delta t+t}, \underline{T}^{\Delta t+t}) = 0 \quad (4.20)$$

$$\underline{v}^{\Delta t+t} - \underline{v}^t - \underline{f}_v(\underline{\delta}^{\Delta t+t}, \underline{u}^{\Delta t+t}, \underline{v}^{\Delta t+t}, \underline{T}^{\Delta t+t}, \underline{u}^{\Delta t+t}, \underline{p}^{\Delta t+t}) = 0 \quad (4.21)$$

$$\underline{p}^{\Delta t+t} - \underline{f}_p(\underline{\delta}, \underline{u}^{\Delta t+t}, \underline{v}^{\Delta t+t}, \underline{T}^{\Delta t+t}, \underline{U}^{\Delta t+t}, \underline{U})^{\Delta t+t} = 0 \quad (4.22)$$

The system can then be solved using a modified Newton method where the Jacobian, which is quite intensive in computational cost, will be updated only when the convergence is impossible or low.



Then at each time step, the following criteria are used for convergence:

$$\max\left(\frac{\delta^{t+\Delta t, n+1} \delta^{t, n}}{\delta^{t, n+1}}\right) \leq \epsilon_{\delta_0} \quad (4.23)$$

$$\frac{1}{\Delta p_r} \max(p_k^{t+\Delta t, n+1} p_k^{t+\Delta t, n}) \leq \epsilon_p \quad (4.24)$$

The resolution procedure is shown in Fig. 4.1. For instance, the Jacobian matrix is calculated once and then only updated when the convergence is weak. The Jacobian matrix will obviously be different for both evaporation and condensation.

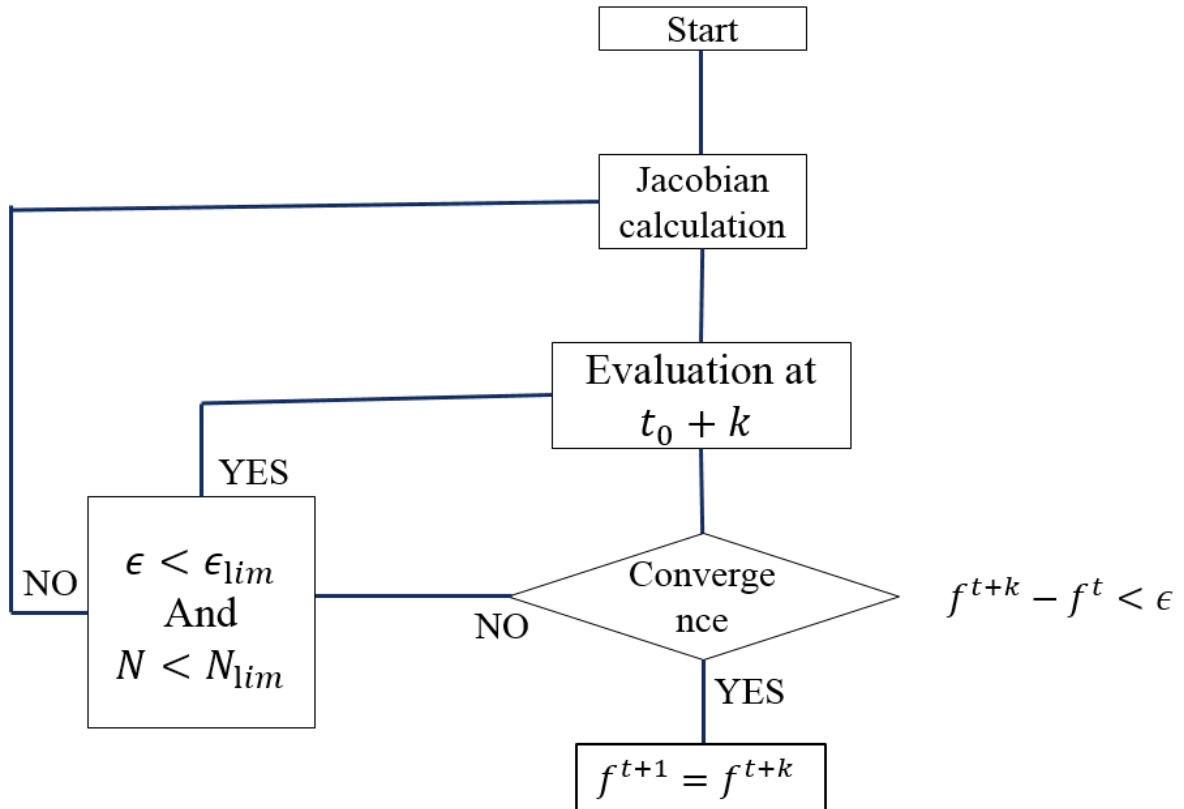


Figure 4.1: Resolution procedure for the annular flow model

Turbulence is taken into account implicitly in Eq. 4.6. Indeed, the use of a straightforward algebraic model for turbulence prevents the need of additional differential equations which would increase the computational cost, such as in standard CFD models like  $k - \epsilon$  or  $k - \omega$

In the case of bubbly flows, the situation will depend on the stage at which the system is, namely single phase, nucleation, bubble growth or consecutive bubbles. For the single phase flow case, which we take rather as an initial condition for nucleation, the problem simplifies to a wall conduction problem with a time-dependent convective cooling boundary condition:

$$\dot{T} - f_T(T_c) = 0 \quad (4.25)$$

with:

$$T(t = 0) = T_0 \quad (4.26)$$

and an imposed heat flux at the outer boundaries and a zero heat flux condition at the inlet and outlet boundaries of the domain.

During the nucleation process, the growth of the bubble is controlled by its nucleation velocity defined earlier, as such we obtain:

$$\dot{T} - f_T(r, T_c) = 0 \quad (4.27)$$

with:

$$T(t = 0) = T_{singlephase} \quad (4.28)$$

When the bubble has reached the microchannel walls, it flows downstream and we are required to solved the growth of the bubble combined with the wall conduction:

$$\dot{T} - f_T(T_c, z_N) = 0 \quad (4.29)$$

$$z_N \dot{N} - f_T T_c, z_N = 0 \quad (4.30)$$

with:

$$T(t = 0) = T_{singlephase} \quad (4.31)$$

$$z_N(t = 0) = r_{max} \quad (4.32)$$

where  $r_{max}$  is the maximum radius of the bubble during the nucleation phase.

Finally, when consecutive bubbles flow in the microchannel, we obtain the following system of equations:

$$\dot{T} - f_T(T_c, z_N) = 0 \quad (4.33)$$

$$z_N^i - f_T(T_c, z_N^i) = 0 \quad (4.34)$$

$$z_N^{i+1} - f_T(T_c, z_N^{i+1}) = 0 \quad (4.35)$$

Compared to the annular flow model, this system is easier to solver and we can as well use an implicit method.

## 5 Experimental validation

The turbulent annular liquid film model was validated against a set of experimental results for both condensation and evaporation. Turbulent condensation is validated against the experimental results of Del Col *et al.* [21] for various vapor qualities, while the simulations for evaporating turbulent liquid film are validated against the results of Ong and Thome [35].

To implement this, an adiabatic entrance length is placed before the diabatic section (as in Fig. 5.1) with heat flux boundary condition. This allows the liquid film and vapor core to be fully developed at the entrance of the section, but obviously a thermal development region will form at the inlet of the diabatic section.

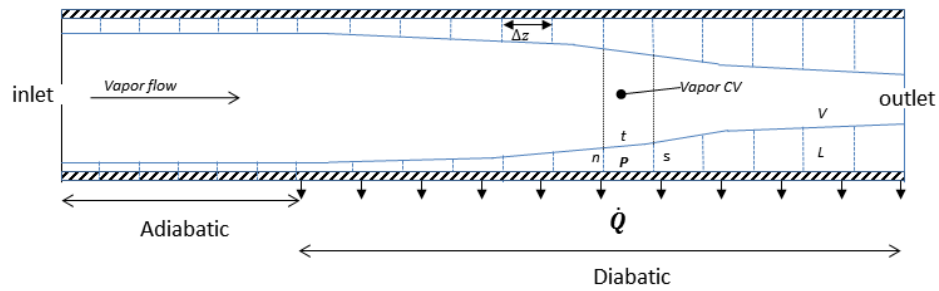


Figure 5.1: Adiabatic entrance length definition for the experimental validation

### 5.1 Turbulent liquid film condensation validation

Del Col *et al.* [21] carried out experiments on a single square copper microchannel with a hydraulic diameter of  $1.23\text{ mm}$  where the coolant (water) flows circumferentially around the inner microchannel

	Total length [mm]	$D_h$ [mm]	$G$ [ $\frac{kg}{m^2s}$ ]	fluid	$T_{sat}$ [ $^{\circ}C$ ]	State
Experimental setup	240	1.23	200	R134a	31	-
Experimental setup	240	1.23	400	R134a	31	-
Numerical setup	140	1.23	200	R134a	31	Laminar
Numerical setup	140	1.23	200	R134a	31	Turbulent
Numerical setup	140	1.23	400	R134a	31	Turbulent

Table 5.1: Del Col *et al.* [21] annular flow condensation operating conditions

(as in Fig. 5.2). By placing thermocouples in the surrounding coolant, they were able to capture local temperature variations which are very small for condensation. This led to a capture of the local refrigerant temperature, the local heat transfer coefficient and heat fluxes. Since no general flow pattern currently exists for condensation in microchannels, the transition from annular to plug/slug flow can hardly be identified. Harirchian et al. [24] provide a flow pattern map for R134a at 52  $^{\circ}C$  in a 1 mm diameter channel that can be used to calculate the outlet vapor quality for the numerical simulation and hence the length of the channel in the latter. The map shows the exit vapor quality of Del Col *et al.* [21] is in an annular state and hence the same length of channel can be used.

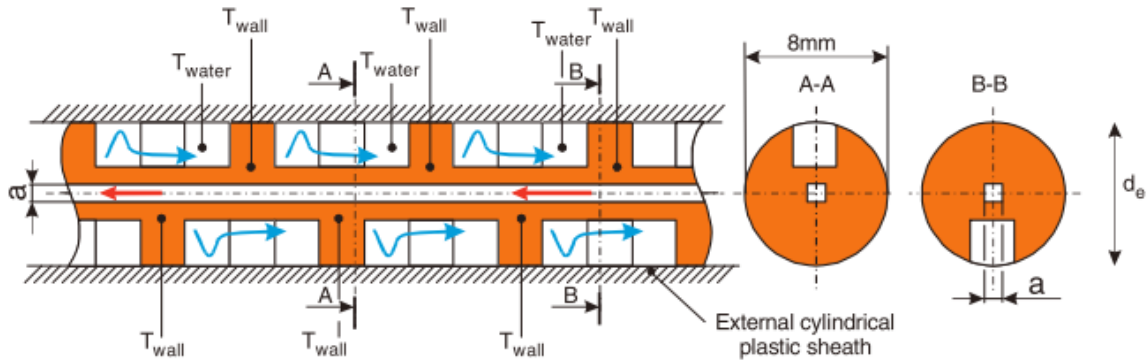


Figure 5.2: Vapor to liquid volume ratio identification

The operating characteristics of the experimental and numerical equivalent model are summarized in Tab. 5.1.

A preliminary run is first done in the adiabatic mode in order to get rid of the hydraulic development length, but the thermal development length will however remain. Three cases were run, one laminar annular condensation case at mass velocity  $G = 200 \frac{kg}{m^2s}$  and two turbulent cases at  $G = 200 \frac{kg}{m^2s}$  and  $G = 400 \frac{kg}{m^2s}$ . Fig. 5.3 shows the results of the simulation for the selected operating conditions. It is interesting to see that the laminar annular liquid film approach captures well the trend of the low mass velocity case at  $G = 200 \frac{kg}{m^2s}$ . Furthermore, for the two other cases for condensation at 200 and  $400 \frac{kg}{m^2s}$ , both seem to follow the trend of the  $G = 400 \frac{kg}{m^2s}$  simulation. This can be explained by the fact that for a square channel, at high vapor qualities and low mass velocities, the capillary forces will still remain dominant with respect to the forces exerted by the shearing gas and that are the source of turbulence in our current model. As such, for such cases, the turbulent eddy diffusivity for momentum and heat will be only active in the corners of the microchannel. Higher mass velocities and lower vapor qualities should lead to larger disparities between the simulation cases. This will in fact be the case most of the

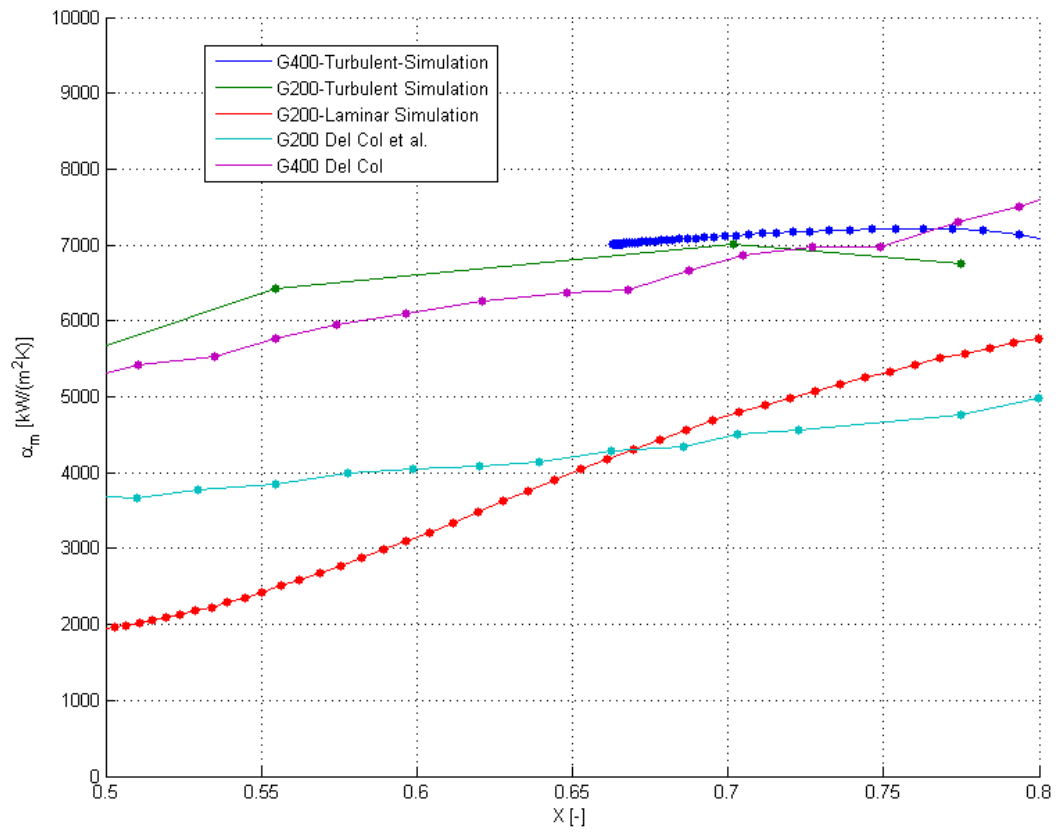


Figure 5.3: Validation against experimental data of Del Col *et al.*, R134a at  $31^\circ\text{C}$ , square cross section with  $D_h = 1.23\text{mm}$ , horizontal orientation

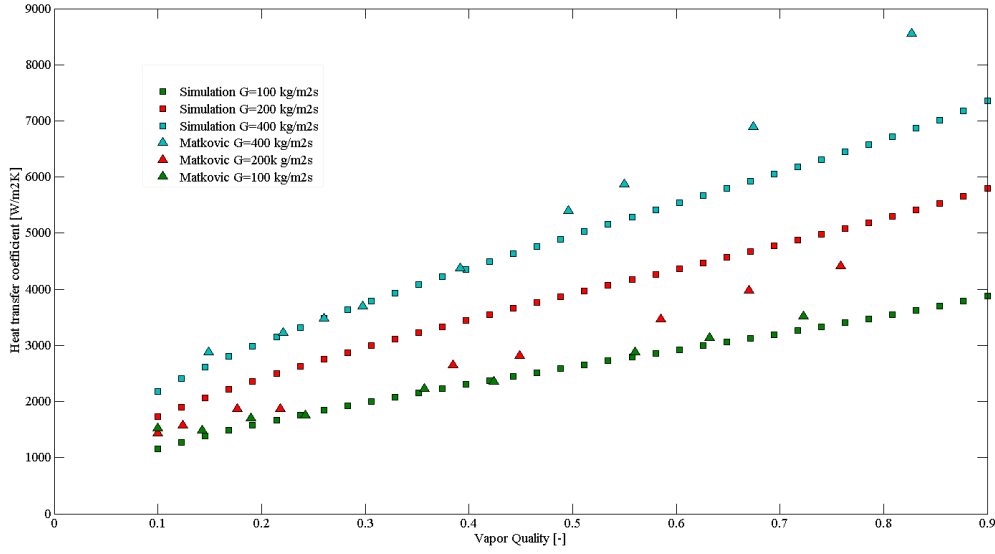


Figure 5.4: Validation against experimental data of Matkovic *et al.* [30], R134a at 31°C, Circular cross section with  $D_h = 960\mu m$ , horizontal orientation

time for evaporation where the capillary forces are not dominant compared to interfacial evaporation. As there is no criteria to determine where the laminar to turbulent transition occurs, Fig. 5.3 shows best agreement with the case at  $G=400 \frac{kg}{m^2s}$ . The transition from the laminar liquid film approach to the turbulent liquid film could be enhanced by fine adapting the eddy diffusivities for heat and momentum to smaller channels.

It is interesting to compare the results above where a turbulent liquid film is assumed with the simulation results of a complete laminar assumption that were done earlier. Fig. 5.4 shows the results obtained for three different experimental conditions for a circular microchannel cross section at  $G = 100, 200$  and  $400 \frac{kg}{m^2s}$  and R134a (operating conditions in Tab.5.2). While the low mass velocity case agrees well with the experimental results, the simulations at high mass velocities again under predict data under the assumption of a laminar liquid film. In particular, the numerical code fails at predicting the sharp increase of the higher mass velocity data at high vapor qualities, certainly due to the creation of complicated patterns at the liquid-vapor interface that enhance the heat transfer.

Data from the same laboratory gathered by Matkovic *et al.* [30] was compared with the simulation results at higher mass velocities of  $G = 600$  and  $G = 800 \frac{kg}{m^2s}$  (see Tab. 5.2). Fig. 5.5 shows the numerical results agree well with the experimental data at high mass velocities by capturing well the upward trend of the heat transfer coefficient versus the vapor quality. It does still under predict the heat transfer coefficient at high vapor qualities.

Simulation results under laminar and turbulent annular liquid film conditions show a fairly good agreement with the experimental data gathered by different researchers. The overall trend shows that a turbulent liquid film condition is needed in order to capture the heat transfer trend at high mass velocities, without which the heat transfer coefficients would be highly under predicted. We can also notice a better agreement of the data with circular test sections compared to rectangular test

	$D_h$ [mm]	$G$ [ $\frac{kg}{m^2s}$ ]	fluid	$T_{sat}$ [ $^{\circ}C$ ]	Liquid film state
Experimental setup	0.96	100	R134a	31	-
Experimental setup	0.96	200	R134a	31	-
Experimental setup	0.96	400	R134a	31	-
Experimental setup	0.96	600	R134a	31	-
Experimental setup	0.96	800	R134a	31	-
Numerical setup	0.96	100	R134a	31	Laminar
Numerical setup	0.96	200	R134a	31	Laminar
Numerical setup	0.96	400	R134a	31	Laminar
Numerical setup	0.96	600	R134a	31	Turbulent
Numerical setup	0.96	800	R134a	31	Turbulent

Table 5.2: Matkovic *et al.* [30] annular flow condensation operating conditions

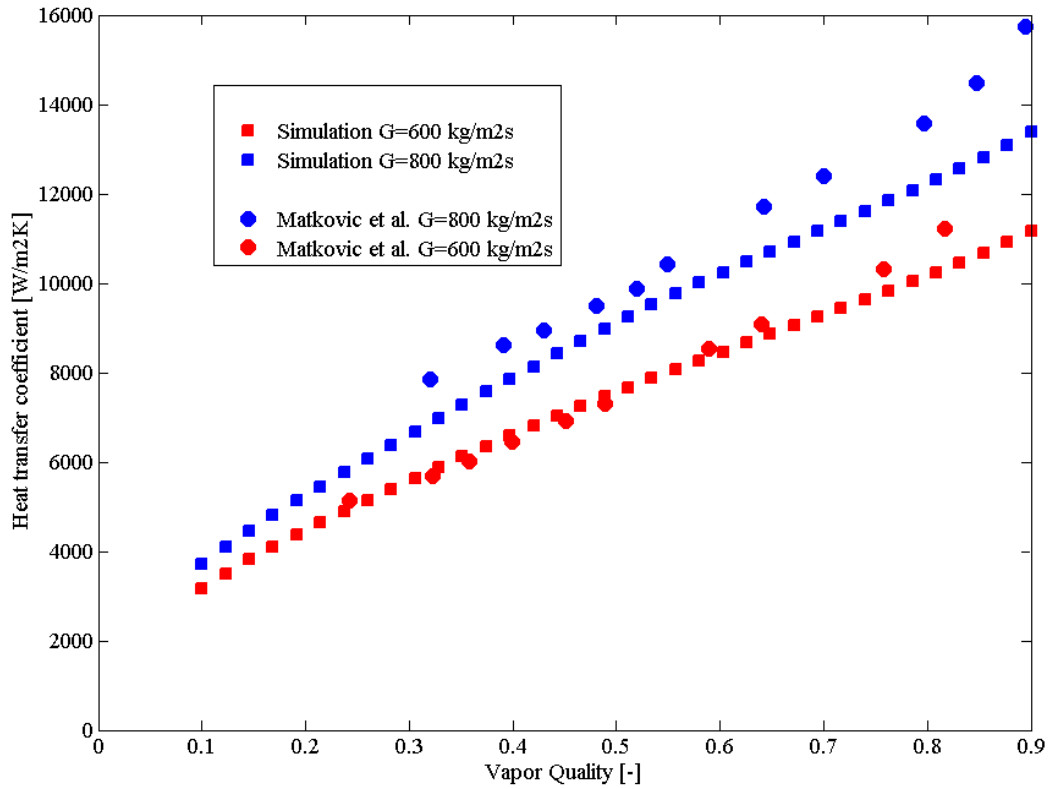


Figure 5.5: Validation against experimental data of Matkovic *et al.*, R134a at 31 $^{\circ}C$ , Square cross section with  $D_h = 1.18mm$ , horizontal orientation

	Total length [mm]	$D_h$ [mm]	$G$ [ $\frac{kg}{m^2s}$ ]	fluid	$T_{sat}$ [ $^{\circ}C$ ]
Experimental setup 1	180	1.030	200	R245fa, R	40
Experimental setup 2	180	1.030	200	R236fa, R	40
Numerical setup 1	100	1.03	200	R245fa	40
Numerical setup 2	100	1.03	200	R236fa	40

Table 5.3: Ong et al. *et al.* [35] annular condensation operating conditions

sections. This is partially due to the microchannel corners that would play a major role in dampening or fostering the turbulent eddy diffusivity for heat and momentum. A transition from laminar to turbulent liquid films, while not depicted here, is likely to happen between 200 and 400  $\frac{kg}{m^2s}$  but would be dependent on the microchannel cross sectional shape.

## 5.2 Annular flow evaporation validation

The evaporating annular flow model is validated against the experimental data of Ong. *et al.* [35] for R134a in a horizontal 1.030mm circular channel. These authors provided heat transfer results for three different regimes (isolated bubble, coalescing bubble and annular flows) for mass velocities ranging from 200 to 1600  $\frac{kg}{m^2s}$ , heat fluxes from 2.3 to 250  $\frac{kW}{m^2}$  and include subcooling. The current heat transfer validation is carried out for two low mass velocities of 200 and 400  $\frac{kg}{m^2s}$  and the operating conditions described below:

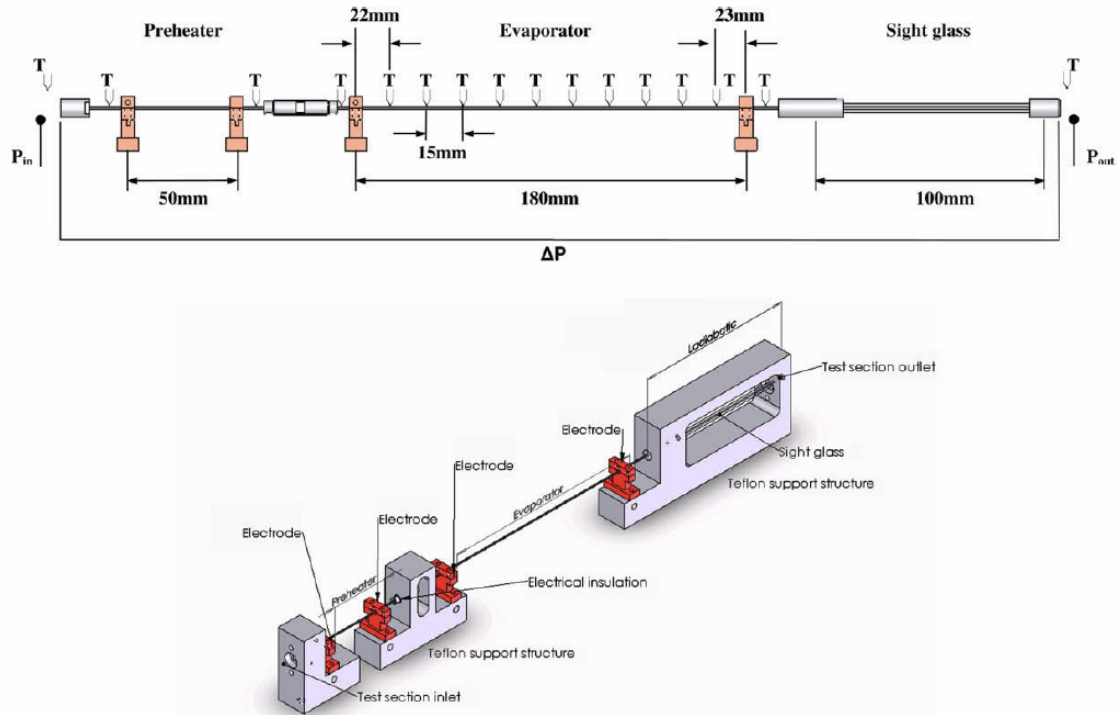


Figure 5.6: Ong and Thome *et al.* [35] experimental setup

Two different refrigerants were tested, R245fa and R136a . At a low mass velocity of 200  $\frac{kg}{m^2s}$  in Fig 5.7, the simulations agree well with the experimental results for both R236fa and R245fa but slightly under predict the results for high vapor qualities. This can be due to the transition to a very highly



flow pattern with non negligible entrainment of liquid that can increase the heat transfer by thinning the liquid film. Simulations at a higher mass velocity of  $400 \frac{kg}{m^2s}$  is shown in Fig. 5.8. The same under

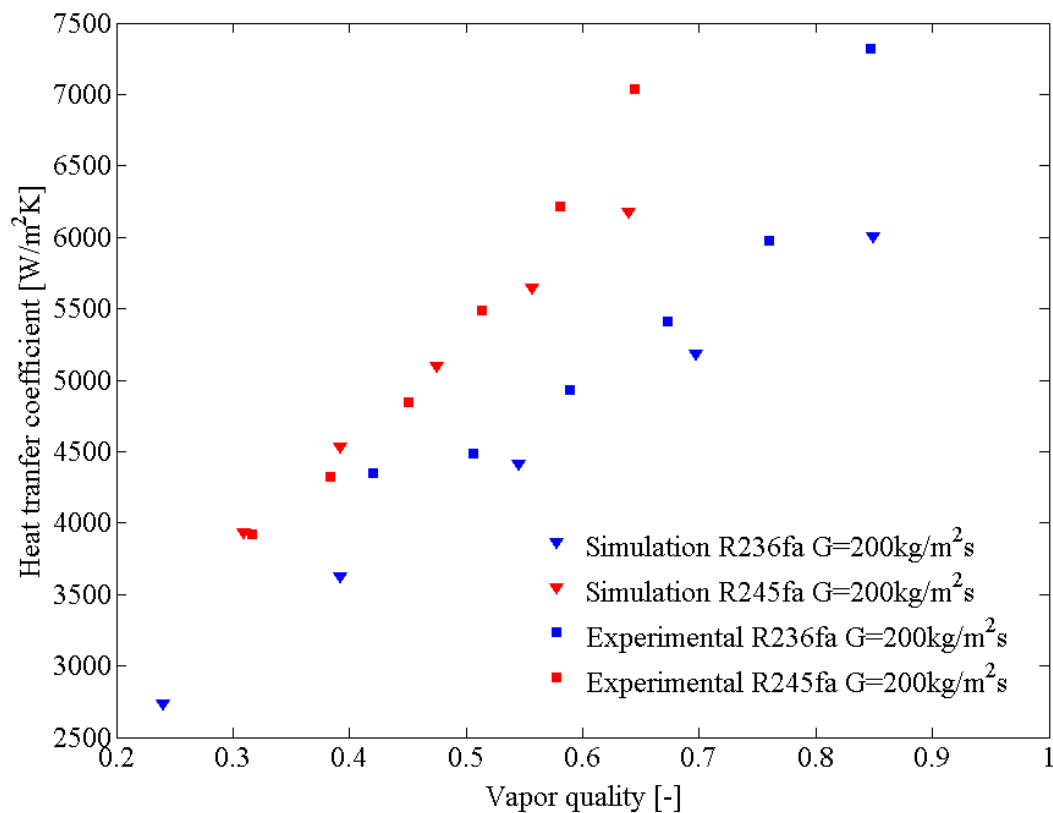


Figure 5.7: Ong and Thome [35] experimental comparison, mass velocity  $G=200 \frac{kg}{m^2s}$

prediction occurs at high vapor qualities. At around a mass velocity of  $x = 0.4$ , the results show an increase in heat transfer coefficient while decreasing the vapor quality. This is certainly due to the transition to a slug/elongated bubble flow regime which is not taken into account in the annular flow model. All simulations show an increase of the heat transfer coefficient with the vapor quality. In the current scenario, the simulated conditions were without the occurrence of a dry patch, thus preventing the drop in heat transfer coefficient that would otherwise be seen. These assumptions seems to be acceptable for circular cross sections as the lack of capillary forces arising from the corners in non-circular microchannels is likely to create a shear driven film that is uniformly distributed around the circumference of the microchannel.

Providing a fairly good estimate of the heat transfer coefficient for microchannel annular flow evaporation, it is interesting to now compare the results for slug flows and elongated bubbles in microchannels, a flow regime that is widely investigated experimentally.

### 5.3 Slug flow and elongated bubble validation

We can identify at low vapor qualities two different flow regimes according to flow pattern map of Revellin and Thome [44] and the updated version of Ong and Thome [33], namely the isolated bubble

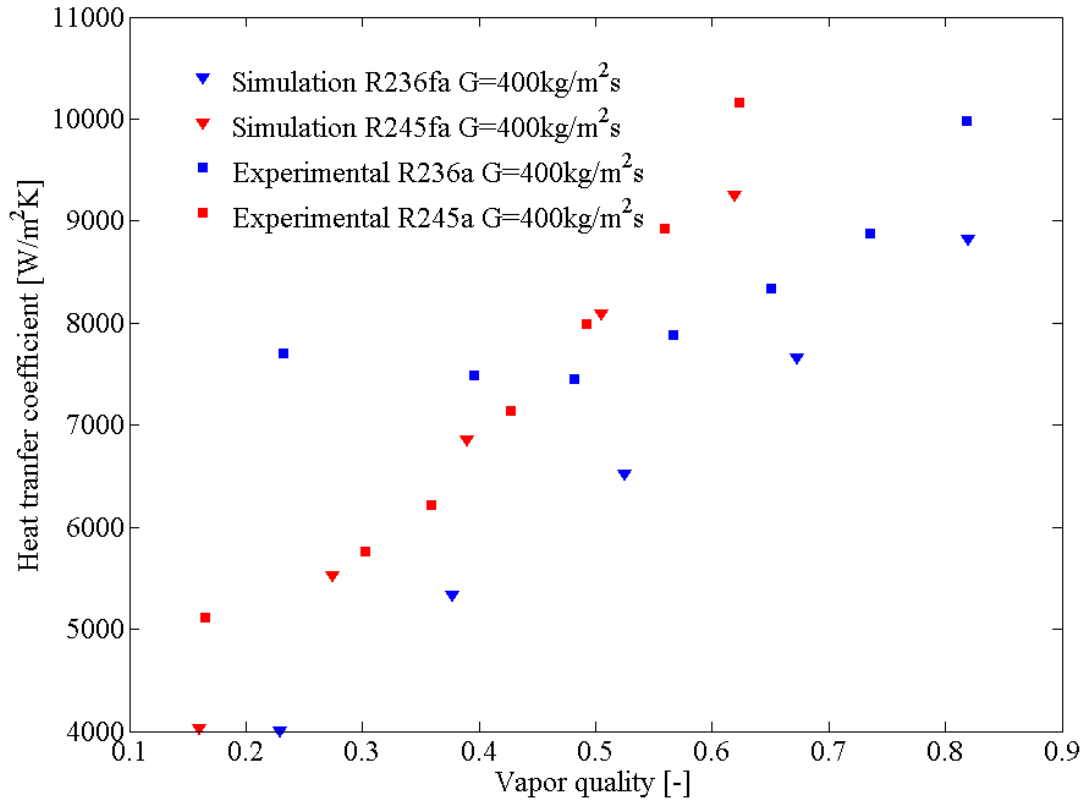


Figure 5.8: Ong and Thome [35] experimental comparison, mass velocity  $G=400 \frac{\text{kg}}{\text{m}^2\text{s}}$

regime and the coalescing bubble regime. In the isolated bubble regime, single bubbles nucleate independently and flow downstream with the average flow. As they flow, their volumes increase and they elongate. In the coalescing bubble regime, elongated bubbles coalesce together and form longer bubbles that are likely to transform the flow into an annular flow regime. Coalescence of elongated bubbles (and disappearance of the dry patch between the bubble and the wall) tends to happen because the low thermal resistance of the liquid film trapped between the bubble and the wall tends to provoke a high vapor-liquid interface mass transfer that increases the volume of the bubble. In the coalescing bubble regime, the bubbles are likely to grow in both directions, thus favoring coalescence between two consecutive bubbles.

In the current model, coalescence of bubbles is not considered in the code. Therefore, we will limit the simulations to the cases of the Isolated bubble regime which tends to be found between vapor qualities of 0 to 0.2 and mass velocities of 0 to  $500 \frac{\text{kg}}{\text{m}^2\text{s}}$ . As the mass velocity increases, the isolated bubble regime narrows down and bubbles coalesce directly. The cyclical nature of the flow requires the use of a time averaged heat transfer coefficient over a period  $\tau$ :

$$\alpha = \frac{1}{\tau} (\tau_{\text{singlephase}} \alpha_{\text{liquid}} \tau_{\text{slug}} \alpha_{\text{slug}} + \tau_{\text{thin film}} \alpha_{\text{thin film}}) \quad (5.1)$$

where  $\tau$  is the period we are considering and  $\tau_i$  are the respective passage time of the slug, thin film or single phase flow. A first step into the validation of the model is the bubble growth rate when the

nucleation phase is over. As the bubbles reach the inner walls, they start flowing down and elongate, creating a thin film between the bubble and the wall. Evaporation through the thin film is the main active mechanism of bubble growth in our case and needs to be verified.

Agostini *et al.* [4] carried out experiments in two horizontal micro-evaporator channels for R134a in 509 and 790  $\mu\text{m}$  microchannels at mass velocities of 200 and 500  $\frac{\text{kg}}{\text{m}^2\text{s}}$ . The authors used fast, high definition digital video camera to capture the bubble speed as a function of the bubble length. In particular they found that the bubble speed increased with increasing channel diameter and homogeneous flow velocity. In order to eliminate the effect of the average velocity of the flow on the bubble velocity, they subtracted the homogeneous flow velocity from the bubble velocity, defined as:

$$U_h = \frac{Gx}{\rho_v} + \frac{G(1-x)}{\rho_l} \quad (5.2)$$

where  $x$  is the thermodynamic vapor quality. As stated by the homogeneous flow model, when small bubbles flow in a liquid, their velocity should tend towards the velocity of the surrounding liquid, and therefore  $U_b - U_h$  should tend towards 0. Then thin film evaporation becomes active and the bubble grows. Since one of the empirical parameters we use is the front liquid film thickness at the nose of the bubble, it is interesting to see how it relates to the pair velocity (velocity of liquid slug and bubble combined).

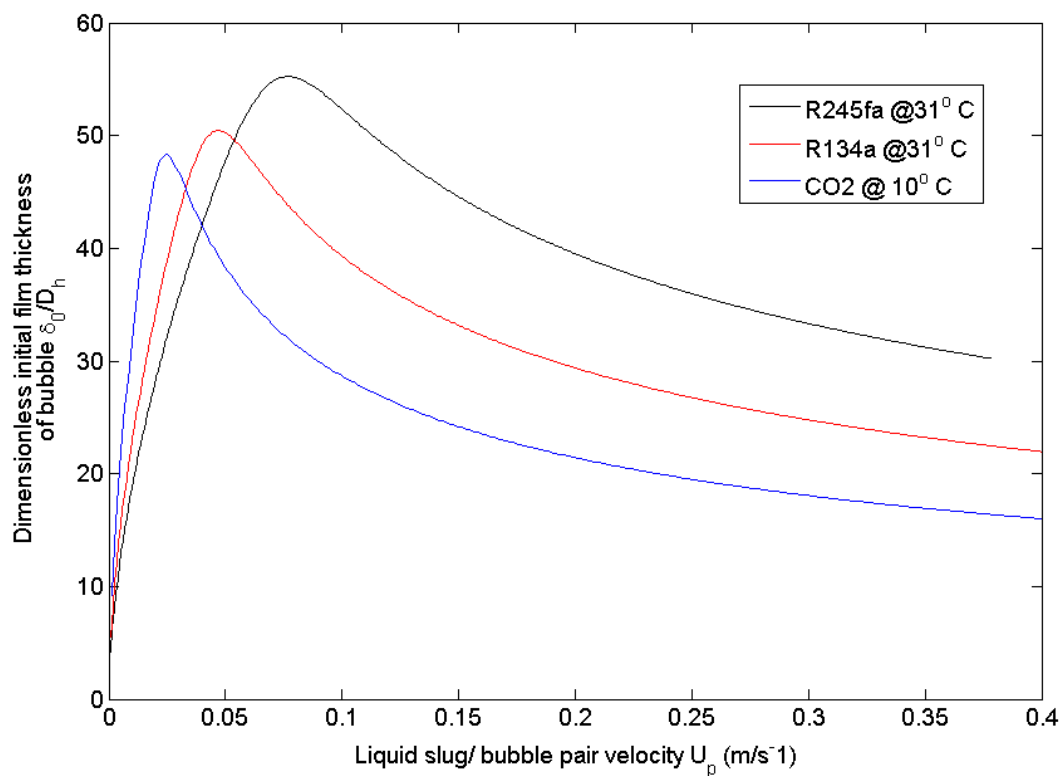


Figure 5.9: Elongated bubble front film thickness correlation of Moriyama *et al.* [31] modified by Dupont *et al.* [23] for R134a, R245fa and CO2

Fig. 5.9 shows the dimensionless liquid film thickness as a function of the pair velocity for three

different fluids. While the correlation was developed for R113, we still consider it can be used for our operating fluids R134a, R245fa and CO<sub>2</sub>. We can notice that in our range of velocities of interest, at above 0.2 m/s (we consider flows above 100 kg/m<sup>2</sup>s, the dimensionless thickness of the front film thickness decreases with bubble velocity. Considering this is the boundary condition for the resolution of our thin film evaporation, it is fair to assume that as the inlet film thickness decreases, the average film thickness trapped between the vapor and the wall will decrease and therefore the mass transfer through the interface will be higher (lower thermal resistance). As such, the bubble growth should on one side be higher when increasing inlet mass velocity, and should also increase with increasing bubble growth (bubble growth being the difference between the homogeneous flow velocity and the bubble velocity).

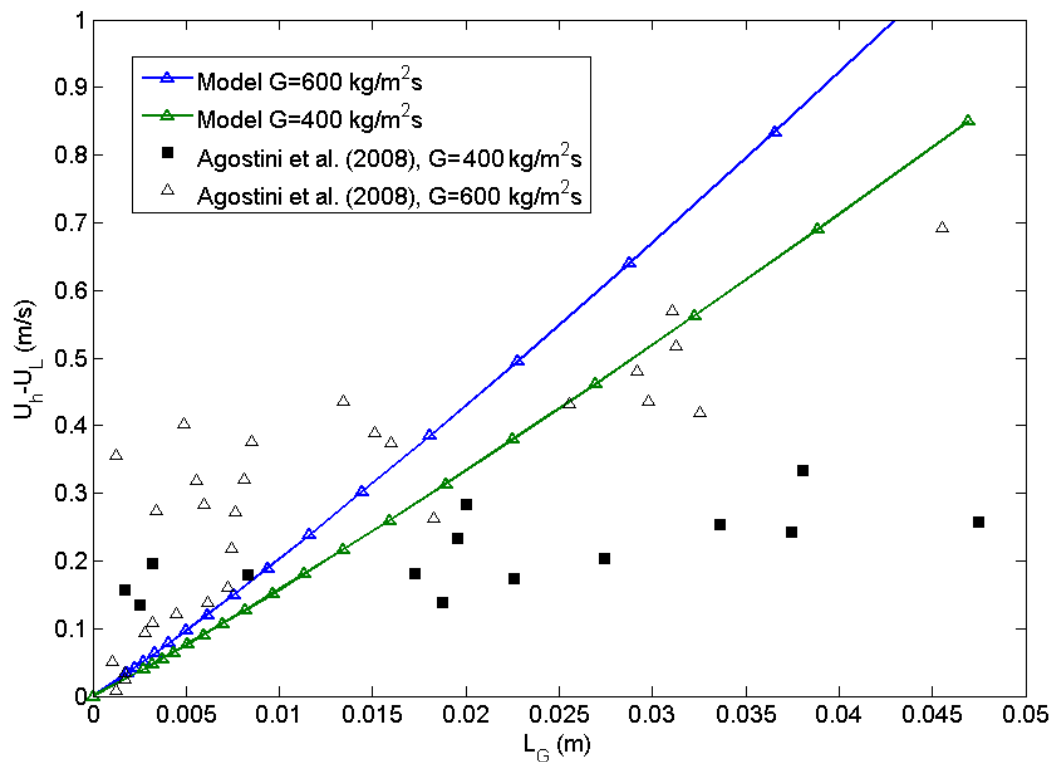


Figure 5.10: Predicted bubble velocity versus experimental results of Agostini and Thome [4]

The flow pattern map of Ong and Thome [35] is used to identify the transition between the isolated bubble regime and the coalescing bubble region at low vapor qualities. In the isolated bubble regime, the bubble growth was plotted against the bubble size in Fig. 5.10 for two different inlet mass velocities. The bubble velocity increases as expected when increasing inlet mass velocity from 400 to 600 kg/m<sup>2</sup>s and increases when the bubble length increases. We notice the model used agrees well with the experimental data at 600 kg/m<sup>2</sup>s while it over predicts the relative bubble velocity for the low mass velocity condition of 400 kg/m<sup>2</sup>s. The latter is particularly the case for very long bubbles above 10 mm. From their experimental results, Agostini *et al.* [4] noticed the bubble relative velocity reached a plateau when increasing the length of the bubble and would not go faster. This effect may arise from either the creation of capillary instabilities at the tail of the bubble and is not taken into account yet in our model, or the appearance of a local dry patch at the tail of the bubble that would reduce

	Total length [mm]	$D_h$ [mm]	$G$ [ $\frac{kg}{m^2s}$ ]	fluid	$T_{sat}$ [ $^{\circ}C$ ]
Experimental setup 1	180	1.03	400	R245fa, R	31
Experimental setup 2	180	1.030	200	R134a, R	31
Experimental setup 2	180	1.030	400	R134a, R	31
Numerical setup 1	50	1.03	200	R134a	31
Numerical setup 2	50	1.03	400	R134a	31
Numerical setup 2	50	1.03	400	R245fa	31

Table 5.4: Ong et al. *et al.* [35] experimental validation parameters

the evaporative rate and hence the bubble growth rate. A future development could include these characteristics in order to properly model very long bubbles in microchannels. As the bubble length goes to 0, the model shows it is going to 0 while the experimental data never reaches a 0 slip velocity. In our simulation, however, the minimum bubble size when bubble growth is active (and hence a liquid film evaporated) is the channel hydraulic diameter since we have an initial step where we nucleate the bubble before it elongates. This prevents the bubble from have a 0 velocity.

Following the validation of the bubble velocity with respect to length, the heat transfer coefficient is compared to the data of Ong and Thome [35] for vapor qualities between 0 and 0.15 and fluids R134a and R245fa with the following operating conditions.

The current model does not take into account bubble coalescence for now and therefore we remain in the isolated bubble regime. Furthermore, as we consider nucleation at the inlet of the channel, the initial condition for the code is a fully developed single phase convective cooling flow. The nucleation of the first bubble is triggered manually at the inlet of the microchannel while the subsequent ones will be characterized by a frequency of appearance given by the model of Plesset and Zwick [37]. As we start from a single phase flow regime and the wall is super heated, the data analyzed are only taken in the fully developed regime, once the wall has reached a steady state average temperature (there might be local fluctuations of the temperature depending on the bubble frequency and length). Due to the intermittent nature of the flow, the local heat transfer coefficient at a given location is given as time averaged value over the total passage time of the concerned heat transfer mechanisms, given by:

$$\alpha_{total} = \frac{1}{\tau} (\tau_{slug} \alpha_{slug} + \tau_{thinfilm} \alpha_{thinfilm}) \quad (5.3)$$

where  $\tau$ ,  $\tau_{slug}$  and  $\tau_{thinfilm}$  are respectively the period of observation, the passage time of the slug and the passage time of the bubble. A first step before the validation is to guarantee we are in a steady state mode. Indeed, the nucleation process and bubble flow is sensitive to the initial conditions such as the initial wall temperature. As such, the comparison is done only once the parameter of interest is no longer fluctuating. The heat transfer coefficient at the outlet of the microchannel is given in Fig. 5.11 for the three cases validated and calculated as follows (the heat transfer coefficient in Fig. 5.11 gives the fluid-vapor side heat transfer coefficient but does not take into account the coupled fluid-heat transfer problem):

$$\alpha_{total} = \frac{q''}{T_w - T_{sat}} \quad (5.4)$$

where  $T_w$  is the local wall temperature. It can be seen that the outlet value of the heat transfer coefficient reaches a steady value after about 2s of the startup. It also shows the different time scales

involved in the process as for the three cases studied, the bubble frequency is between 200 and 400 Hz while the resilience time of the wall is above 1s. In terms of modeling isolated and elongated bubbles, it also shows the limits of most simulations that currently can only handle a few bubbles and cannot therefore capture well the behavior of the conjugate problem. In Fig. 5.11, the initial wall temperature was arbitrarily added as an input to the code in order to converge faster rather than starting from a single phase flow mode where the wall superheat would be much higher.

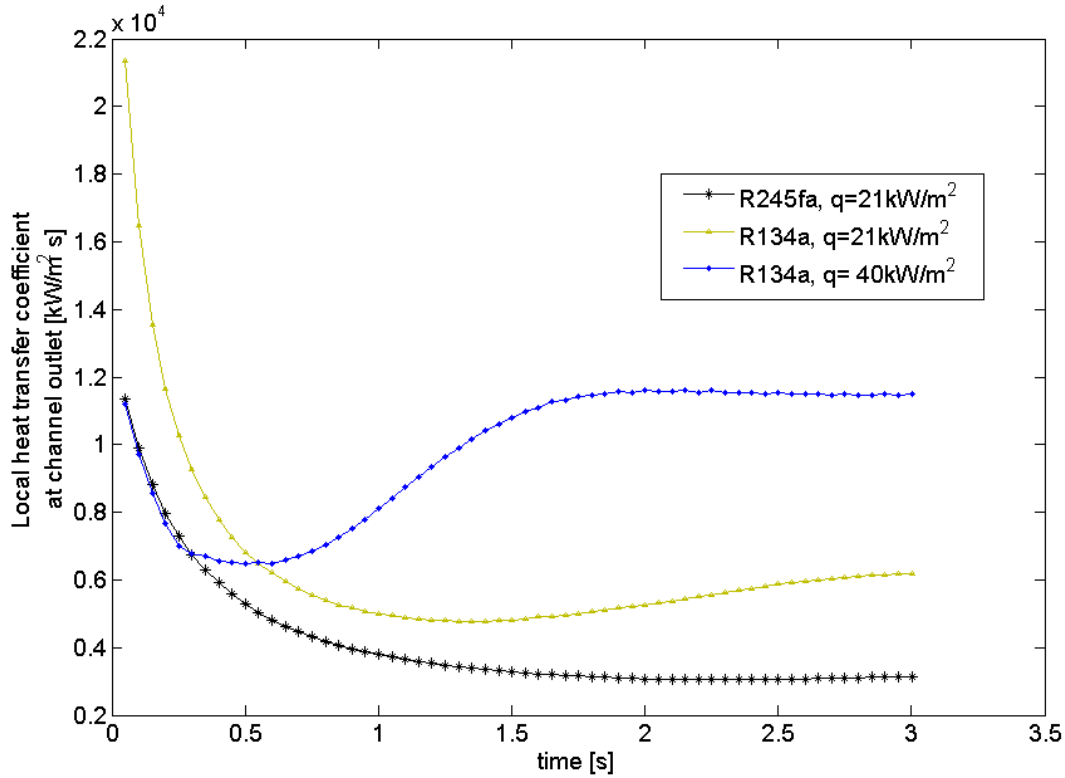


Figure 5.11: Fully developed state definition

During the steady state mode, the heat transfer coefficient can be plotted for different vapor qualities along the channel. Fig. 5.12 provides a comparison for the the three cases considered in Tab. 5.4 and vapor qualities taken between 0 and 0.1. It can be noticed that the agreement with experimental results is fairly good for low vapor qualities with a maximum error of 25% for R134a at a mass velocity of  $200 \text{ kg/m}^2\text{s}$  and 15 % for R245fa at  $200 \text{ kg/m}^2\text{s}$ , the error being lower at lower vapor qualities. However, the models highly over predicts the data at  $400 \text{ kg/m}^2\text{s}$  for R134a, in particular at higher vapor qualities. An explanation for such a discrepancy might come from the difficulty to replicate the experimental conditions on the model. Indeed, as already stated, the heat transfer coefficient will be very sensitive to the bubble frequency at these low vapor qualities. Furthermore, the three-zone model operating only with two zones has seen less experimental validation. The trend observed experimentally for the case of high mass velocities and high heat fluxes is different than the one observed at lower mass fluxes and velocities, with a flat behavior of the heat transfer coefficient with respect to the vapor quality. This leads one to think that in the case of high mass velocities and high heat fluxes, we are more likely to be in a regime with a high number of isolated bubbles that flow with

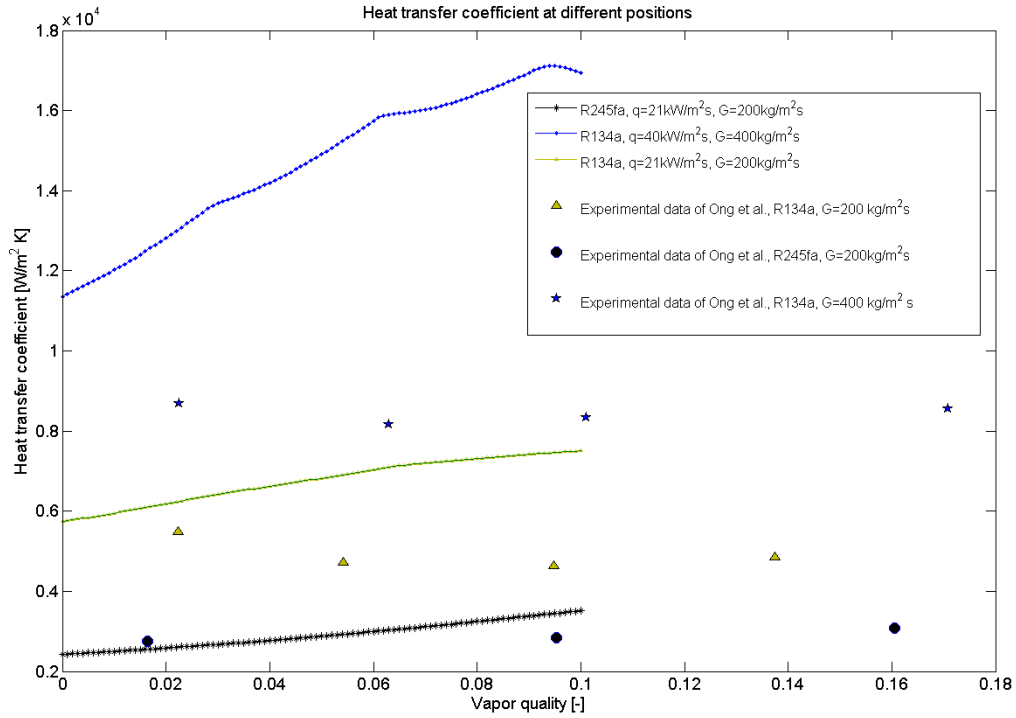


Figure 5.12: Ong and Thome *et al.* [35] heat transfer coefficient experimental validation for isolated bubble regime, Circular microchannel with  $D_h = 1 \text{ mm}$

the saturated liquid while at lower mass velocities the bubbles are likely to merge and elongate, thus describing an increase of heat transfer coefficient with respect to the vapor quality (partly due to the appearance of thin films between the bubble and the wall). The next section will try to understand these different behaviors and their impact on the heat transfer process.





## 6 Case studies

In the current chapter, selected simulation results will be shown and explained with the objective to provide some useful insights on the design of microchannel heat exchangers. Firstly, we will consider turbulent condensing flows and how turbulence can influence the overall performance of the heat exchanger. Secondly, we will consider evaporating annular flows in microchannels and try to depict the difference with condensing annular flows or condensation in microchannels. Finally, we will look at bubbly flows and elongated bubbles behavior.

### 6.1 Condensing turbulent annular flows

Condensing annular flows encountered in common applications are often beyond the laminar region. While the capillary effects do play a dampening effect on the annular flows itself, for instance dampening the turbulent eddies through the surface tension, for high mass velocities, the shear exerted by the vapor core will influence the liquid film and foster the transition towards a turbulent or at least unstable liquid film. In the current analysis, we will investigate what influence the turbulent eddies can have on the overall thermal performance of the heat exchanger. While it is well established that higher mass velocities, or an increased turbulence, will favor the exchange of heat between the vapor and the wall, other parameters such as the microchannel geometry can have a large impact on the flow itself by promoting turbulence.

We consider three microchannels with an equivalent hydraulic diameter of 1.23 mm but different areas and cross sections. Three cross sectional shapes are used, (a circular, an elliptical and a rectangular microchannel) with the following operating conditions: the mass velocity is kept at  $400 \frac{kg}{m^2s}$  in order to guarantee the appearance of turbulence. The ellipse has a major axis of 1.6 mm and a minor axis of 0.8 mm (aspect ratio of 2) and the gravity points towards the minor axis direction. Fig. 6.1 shows the cross sectional film thickness profile at the outlet of each microchannel. With competition of the capillary forces versus gravity forces, the profile displays a typical thick film at the channel corners where the

	Shape	$D_h$ [mm]	$G$ [ $\frac{kg}{m^2s}$ ]	fluid	$T_{sat}$ [ $^{\circ}C$ ]
Numerical setup	circular, elliptical, square	1.23	400	R134a	31

Table 6.1: Turbulent Annular Flow Condensation Parameters

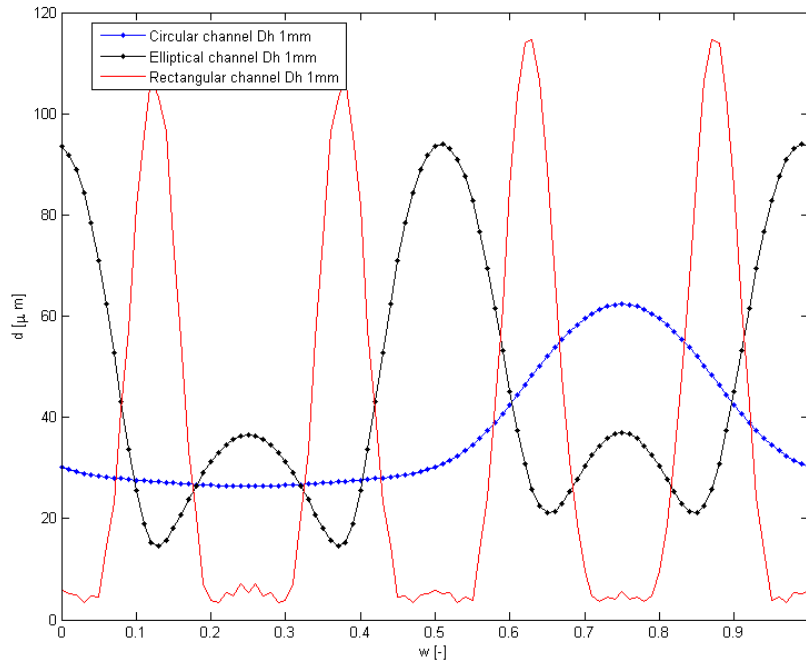


Figure 6.1: Cross sectional liquid film thickness for square, circular and elliptical channel with  $D_h = 1.23\text{mm}$

condensate is pulled. The circular channel shows a dominant influence of the gravity by pulling the liquid towards the bottom of the channel. The elliptical cross section displays an influence of both gravity and capillary forces as the liquid is also pulled towards the sides of the microchannel where the microchannel curvature is higher. The square channel shows a typical influence of the capillary forces due to the corners of the microchannel. As such, the liquid will be pulled towards the corners and display a very low thermal resistance at the center of the channel walls where the liquid film is thin.

In its dimensionless form, using the approach proposed by Cioncolini and Thome [12], the liquid film thickness displayed in Fig 6.2 gives a similar profile as the dimensional one. It is interesting to remember the lower boundaries for the turbulent eddy diffusivity for heat and momentum. The turbulent eddy diffusivity for momentum is active from a dimensionless thickness of  $t^+ = 10$  while the eddy diffusivity for heat for dimensionless film thickness of  $T^+ = 30$ . As such, we can notice that the eddy diffusivity for momentum will be less active than the eddy diffusivity for heat, yet it will have an influence in the rectangular cross section and elliptical cross section which sees peaks of dimensionless film thickness up to 100. The eddy diffusivity for heat will be always active for the circular microchannel but will be limited to  $T^+ = 40$  while for the square cross section, it will peak at  $t^+ = 100$ , leading to very high heat dissipation.

The calculated eddy diffusivity for heat for the three cross sections is provided in Fig 6.3. We can notice the sharp rises in eddy diffusivity for the rectangular cross section at the channel corners. These have an important effect on the overall heat transfer coefficient since the equivalent thermal conductivity (laminar and turbulent thermal conductivities combined) can be 7 times higher in the peak regions. In the circular case, the turbulent eddy diffusivity for heat will always be active, increasing the equivalent

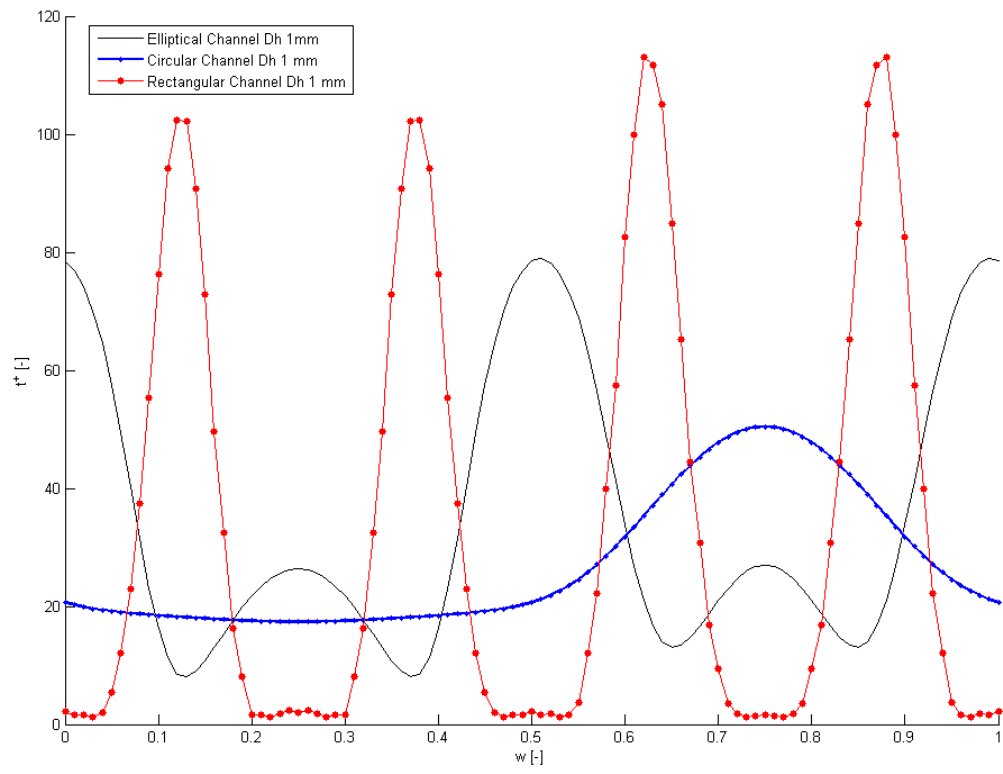


Figure 6.2: Cross sectional local dimensionless film thickness for square, circular and elliptical channel with  $D_h = 1.23\text{ mm}$

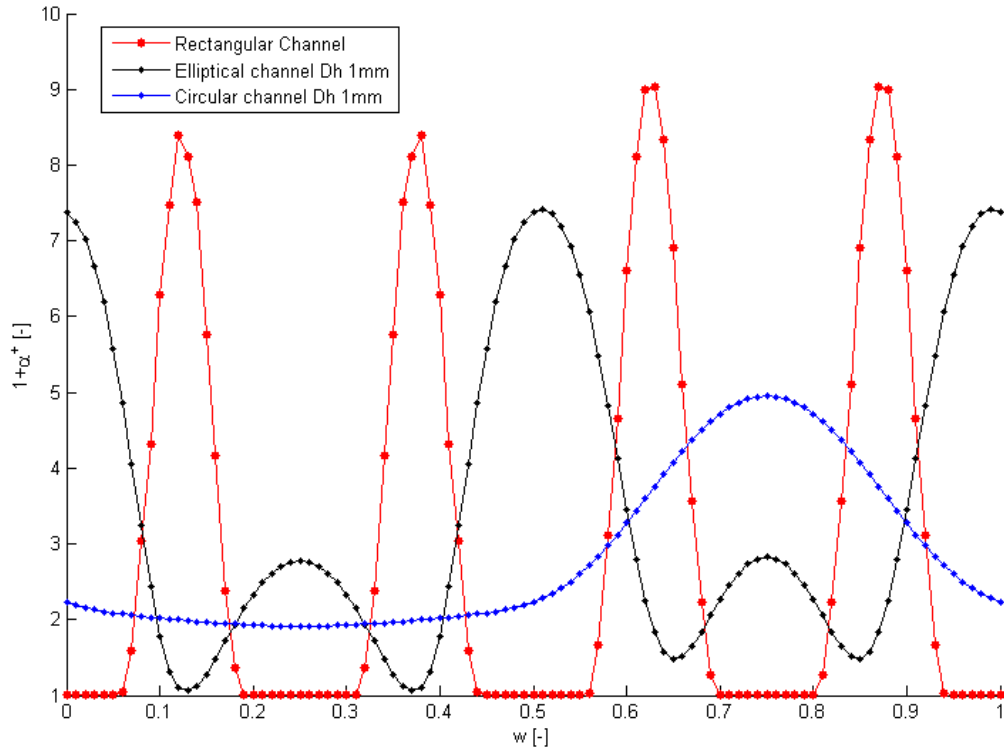


Figure 6.3: Cross sectional local eddy diffusivity for heat for square, circular and elliptical channel with  $D_h = 1.23\text{mm}$

thermal conductivity up to five times compared to the laminar liquid film case.

The consequence of the eddy diffusivity for heat on the overall heat transfer performance is displayed in Fig. 6.4 and Fig. 6.5 where we see the local heat transfer coefficient simulated for the local test conditions. We can notice that in the current scenario the peaks of heat transfer coefficient will be situated at the corners of the microchannel where the film is the thickest. If compared to an equivalent laminar flow condensation, using the square cross section of Agarwall *et al.* [2], we can see a different trend as the thin film conductivity will no longer be the dominant mode of heat transfer and the turbulent dissipation can become more important to consider.

The overall influence of the activation of liquid film turbulence in annular microchannels is depicted in Fig. 6.6 where the perimeter averaged heat transfer coefficient is displayed versus the vapor quality for the three different shapes. Not surprisingly, the rectangular microchannel delivers a higher thermal performance compared to the circular and elliptical microchannel due to the activation of eddy diffusivity for heat at the thick corners. The circular and elliptical microchannel will display a similar performance, considering that the integral of the eddy diffusivity for heat over the perimeter of the microchannel is similar. An interesting observation is the lack of an upward trend that is generally noticed in laminar annular condensation where, while the thin film become thinner, the liquid film thermal resistance reduces and the heat transfer coefficient increases. This leads to two different approaches when considering the turbulent or the laminar case. When the operating conditions are turbulent, one will seek to increase the turbulent eddy diffusivities in order to increase

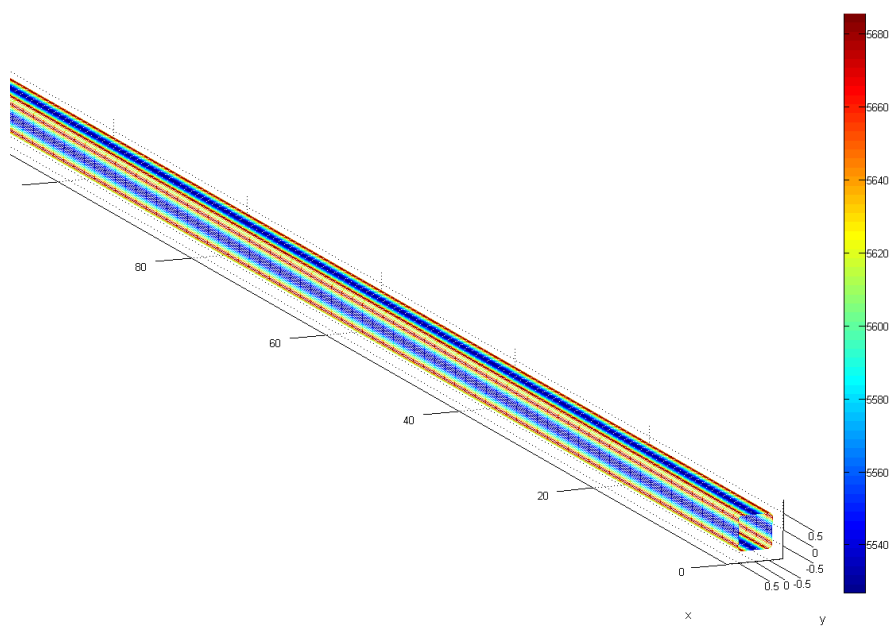


Figure 6.4: 3D representations of the local heat transfer coefficient for square channel,  $D_h = 1.23\text{ mm}$

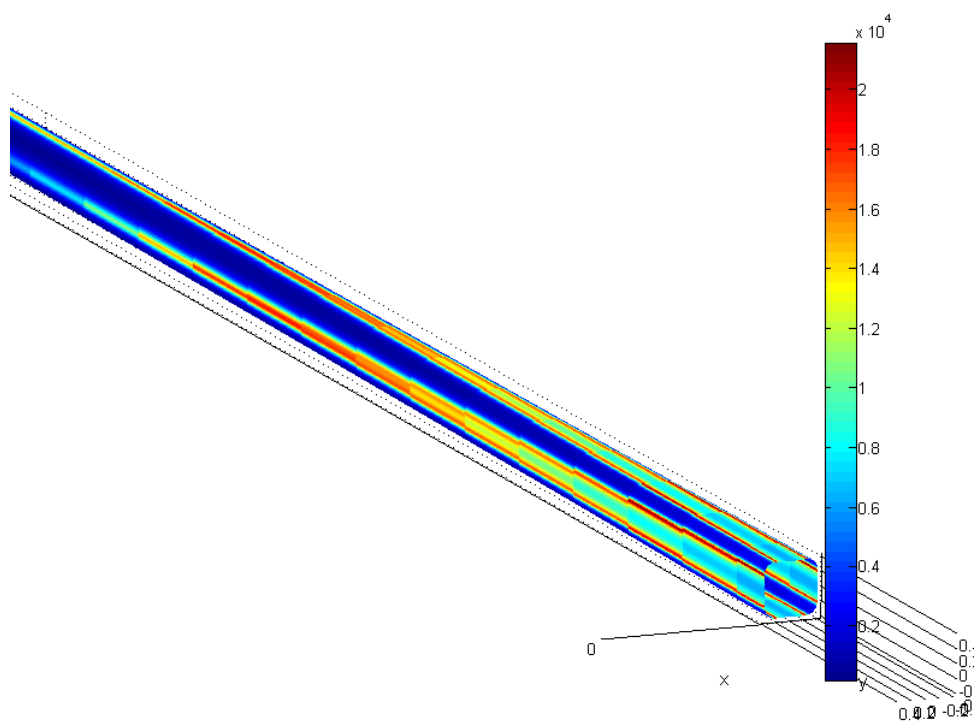


Figure 6.5: 3D representations of the local heat transfer coefficient for square channel, test section of Agarwal *et al.* [2]

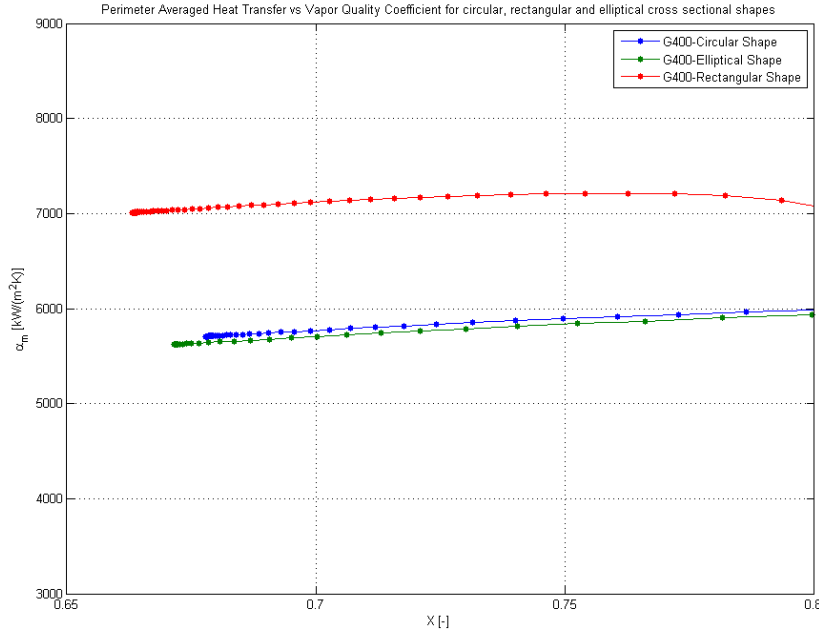


Figure 6.6: Perimeter averaged heat transfer coefficient for square, circular and elliptical channel

performance, either by playing on the Weber number, which influences the interfacial shear stress, or by guaranteeing the thick films at given locations in the microchannel. Oppositely, for laminar annular condensation, one will try to increase the length of thin film regions, by for example, increasing the aspect ratio of rectangular microchannels. It is interesting to notice that for high vapor qualities, the rectangular channel heat transfer coefficient depicts a downward trend, which is against what is found in the laminar liquid film assumption. The main reason for this trend is the disappearance of active turbulence sites at the corners of the microchannel as the vapor quality increases and the liquid film thickens. Hence this trend can be explained as the transition from a turbulent liquid film to a laminar liquid film that leads to a lower overall heat transfer coefficient, despite the thinning of the liquid substrate on the channel walls. For the circular and elliptical channels, this trend is not observed since the lack of corners does not activate so many sites where turbulence is active.

While providing useful insights for increasing the performance of the microchannels at higher heat fluxes, the current approach has a weaknesses. It is likely to overestimate the heat transfer coefficient in cross sections with large capillary effects where the surface tension tends to dampen the turbulent eddies and therefore the local heat transfer coefficient in the microchannel corners would be lower. However, it provides a useful approach by combining the effects of laminar and turbulent condensation, thus making it suitable for a large range of operating conditions.

## 6.2 Evaporating annular flows

Evaporating annular flows are more complex in nature than condensing annular flows. Indeed, evaporating flows in microchannels are highly unstable due to the competition between capillary forces and liquid film evaporation. Indeed, the liquid evaporating in thin liquid film regions triggers a

mass flow from the remaining film towards the thin film regions. In the opposite direction, imposed capillary forces such as a microchannel corner curvature, tend to pull the liquid towards the corners. As shown in the energy equation, the interfacial evaporation  $J_{j,k}^e$  will depend on fluid thermodynamic properties, wall properties and imposed boundary condition. On the other side, capillary forces acting on the fluid are function of the fluid operating conditions, fluid properties and microchannel shape.

Not aiming at resolving the thermo-capillary instability problem, it is interesting to think how this can affect our heat transfer performance and how we can, eventually find the best shapes for improving heat transfer. A first step is to perform a dimensionless analysis on the set of momentum and energy equations as shown in Chapter 3. The characteristic length of the problem can be taken as  $H$ , given by:

$$H = \frac{1}{P} \int_P |K|_{xy} dl \quad (6.1)$$

where  $P$  is the perimeter of the channel and  $K_{xy}$  the local curvature of the channel inner wall. The parameter gives us an idea of the how important the shape of the microchannel is. The type of boundary condition imposed is of foremost importance as the wall conduction and heat flux can play an important role over the liquid film heat transfer. Nebuloni and Thome [32] came up with a heat transfer length for the condensation problem that we will consider here, which is given by:

$$L_{ht} = \frac{l_c}{L_t} \quad (6.2)$$

where the heat characteristic heat transfer length is given by:

$$l_c = \sqrt{\frac{k_w \lambda_w}{h_i}} \quad (6.3)$$

where  $h_i$  is the characteristic heat transfer coefficient on the evaporating side. After performing the dimensionless analysis, we are able to obtain the interface mass transfer and the interfacial pressure numbers as :

$$I_{r,q} = \frac{1}{J_T} \left( \frac{\sigma k_l^4 \rho_l H^4}{\mu_l \Delta h_{lv}^3 |\dot{q}|} \right)^{1/4} \quad (6.4)$$

$$I_{p,q} = \frac{J_P}{J_T} \left( \frac{\sigma^5 \rho_l k_l^4 \Delta h_{lv} H^8}{\mu_l |\dot{q}|^5} \right)^{1/4} \quad (6.5)$$

The interfacial resistance number represents the ratio between the interfacial resistance and the liquid film resistance while the interface pressure number characterizes the ratio between the mass flux contribution due to the pressure jump across the interface and the mass flux due to the temperature difference.

These numbers are interesting from the perspective of understanding the evaporating annular flow behavior as we reduce the scale of the microchannel. Indeed, as was previously stated, the thermo-capillary phenomena that arises from going to microscale levels will have a large influence on the heat transfer performance. For condensing flows, we are generally able to define the transition from

Shape	$D_h$	Heat Flux $\frac{kW}{m^2K}$	$G [\frac{kg}{m^2s}]$	fluid	$T_{sat} [^\circ C]$
Circular	1.03	60	400	R245fa	31
Rectangular	1.00	20	50	R134a	31

macro to micro scale as when the capillary forces will dominate of the inertia forces. For evaporating flows, the transition exists as well, but is likely to influence the heat transfer and fluid flow behavior differently due to the instabilities arising. For instance, at high vapor qualities, when the liquid film is generally thin, researchers have struggled to characterize the trend of the heat transfer coefficient (see Ong and Thome [35]) versus the vapor quality. Indeed, since the heat transfer coefficient is dependent on the heat flux, boundary conditions and fluid properties, it was difficult to propose and explaining for the heat transfer coefficient that would fit a large set of operating conditions or fluids.

If we consider the two cases, one where the capillary forces are dominant (such as in condensation) and one where both the interfacial evaporation and capillary forces have a similar influence, in the first case, we are likely to obtain in the first case a stable liquid film, whose shape will be driven by the microchannel geometry, while in the second case, the liquid film shape is likely to be unstable. From a heat transfer perspective, in the first case we will tend towards a thin film heat transfer process, while for the second case, the heat transfer would be function of the wavy interface. In the first case, when the thin liquid film heat transfer is the dominant mode of wall to vapor heat transfer, we are likely to see the heat transfer coefficient to increase with the vapor quality such as in evaporation until eventually reaching local dryout. In the second case, however, the wavy interface would dampen the influence of the thin film heat transfer and the heat transfer coefficient is likely to remain constant as the vapor quality increases since the highly conductive thin film regions will no longer exist.

Let us consider for our case different simulations scenarios, first a stable liquid film in a circular channel with R245fa and the following characteristics:

Fig. 6.7 shows the typical thin film profile driven by gravity. In the current case, no dry patch forms as the liquid is pulled towards the low thermal resistance regions and evaporate. The equivalent heat transfer coefficient profile is shown in Fig. 6.8 and shows the higher heat transfer areas at the top of the microchannel with an increased overall performance. In the second case, we consider a rectangular microchannel with R134a. Fig. 6.9 displays the evolution of the liquid film between 0 and 2 ms. The competing effects of the capillary forces and thin film evaporation render the liquid highly unstable and wavy. This obviously impacts the heat transfer coefficient, shown in Fig 6.10 as a dry patch is created at 1.9 ms, thus reducing the perimeter averaged heat transfer coefficient.

The two examples mentioned above show how different the obtained performance of a heat exchanger can be in the annular flow regime depending on parameters such as the microchannel geometry, the operating conditions and the fluid. While it is difficult to define optimal operating conditions for each situation, we are able to derive a certain number of conclusions from the analysis above:

- The higher  $H$ , the more likely it is to become unstable
- Higher interface mass transfer numbers lead to unstable regimes

One of the critical aspects that must be understood when designing microchannels that will operate



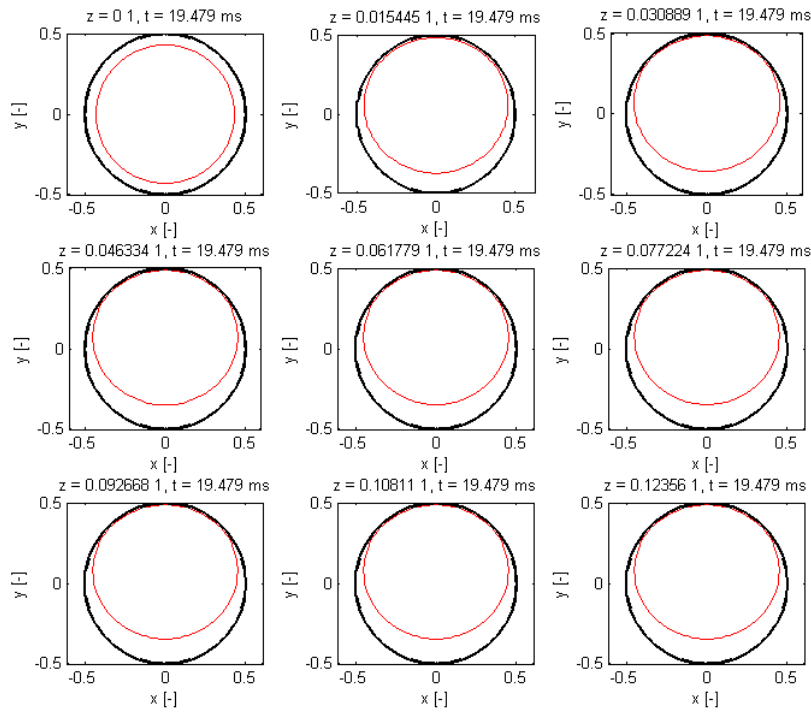


Figure 6.7: Liquid film profile, circular cross section  $Dh = 1.03mm$

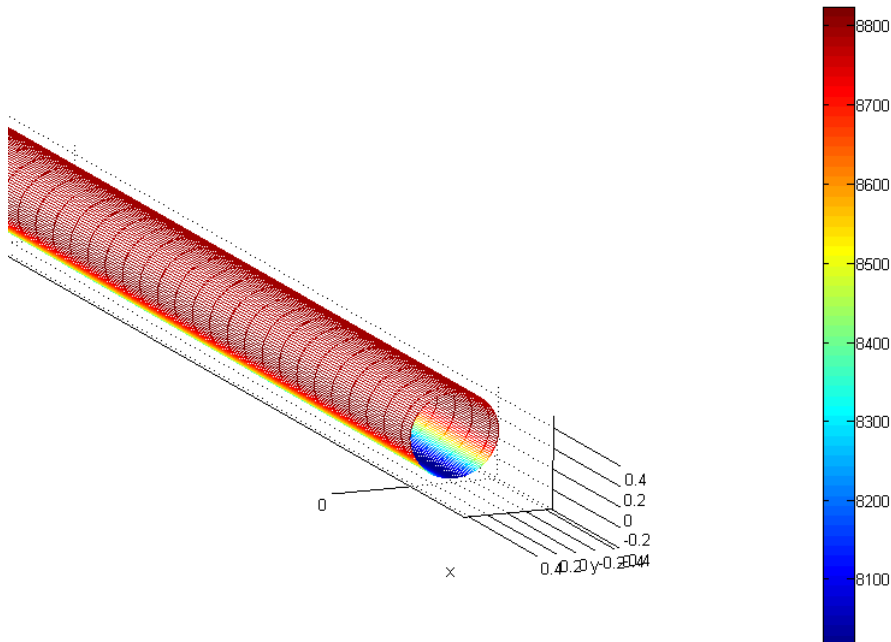


Figure 6.8: Heat transfer coefficient profile, circular cross section  $Dh = 1.03mm$

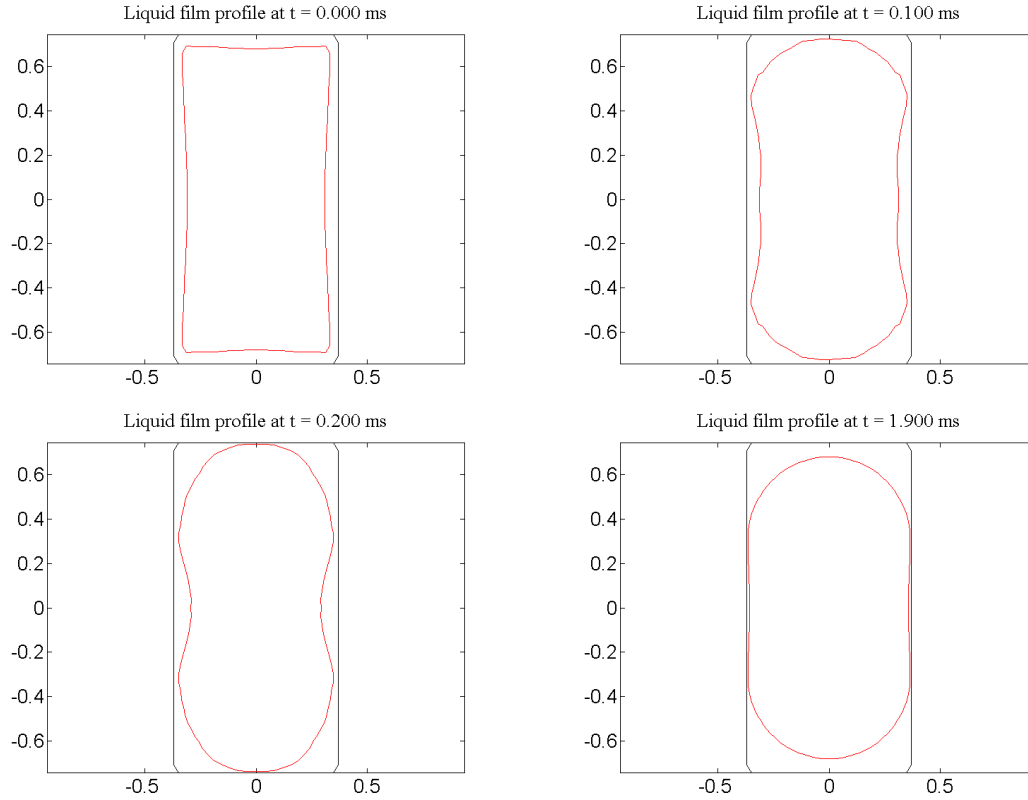


Figure 6.9: Liquid film profile evolution under heat flux  $Q = 20 \frac{kW}{M^2}$

at high vapor qualities is the onset of dryout through of the following modes:

- **Critical heat flux:** the heat flux at the wall is so high that a layer of vapor forms at between the liquid and the wall
- **Dryout of the liquid film:** the liquid film within the annular film completely evaporates
- **Entrainment of the liquid film:** the vapor shear stress is strong enough to completely remove the liquid film.

Critical heat flux can be determined using already available correlations since the process is similar to surpassing the peak nucleate heat flux in pool boiling. The third case, when the liquid film is sheared off by the gas, will not be treated but can be predicted using the already available entrainment model of Cioncolini and Thome [12]. The second case is of interest for our model as the dryout of the liquid film will strongly depend on the local heat transfer performance of the heat exchanger, i.e. on a certain number of parameters such as the geometry, the heat flux and the fluid thermophysical properties. In order to understand how the onset of dryout is due to complete or partial evaporation of the liquid film, we will consider the two different cases. Firstly, a stable liquid film forms and dries out as the liquid evaporates, so that in that case the appearance of a dry patch will rather depend on the geometry. Secondly, we consider an unstable liquid film (at lower mass velocities to avoid the liquid film from begin sheared off by the vapor core), in which case intermittent dry patches will form and the overall performance of the heat exchanger will decrease. The cases are presented for a

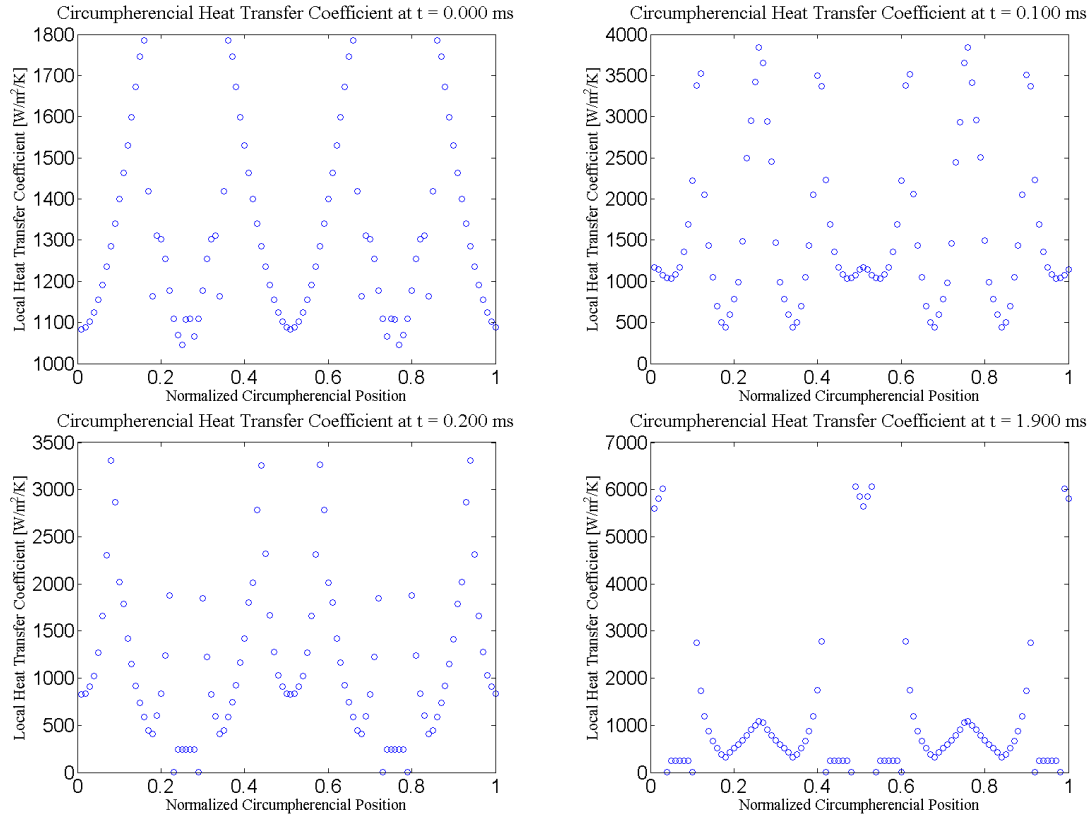


Figure 6.10: Liquid film profile evolution under heat flux  $Q = 20 \frac{kW}{M^2}$

Shape	$D_h$ [mm]	Fluid	Saturation Temperature <sup>o</sup> C	$G$ [ $\frac{kg}{m^2s}$ ]	Orientation
Circular	1.00	R245fa	31	400	horizontal
Rectangular	1.20	CO2	10	400	horizontal
Rectangular	1.20	R245fa	31	400	horizontal

Table 6.2: Input parameters for circular and rectangular cross section simulations

stable circular liquid film that dries out due to the gravitational forces, the second will consider and unstable liquid film with CO2 and R-245fa as shown in Tab. 6.2. The liquid film profile at the outlet of the microchannel is shown as a function of the circumferential position in Fig. 6.11 at times between 0 and 26 ms (where  $t=0$  ms is the initial thickness). We can notice a progressive evaporation of the liquid film until it reaches one of the walls, and then a dry patch forms at 24 ms, altering the performance of the microchannel. In the case of the circular channel, the behavior of the liquid film will therefore rather be governed by the liquid film Bond number (here  $Bo = 2.7$ ). The corresponding heat transfer performance is shown via the Nusselt number in Fig. 6.12 at different times. We can clearly notice the transition from a fully wet cross section to a partially dried out cross section. Interestingly, the low resistance of the liquid film at the three phase line leads to a peak in Nusselt number that might, as long as the dry patch is small enough, counter balance the reduced performance due to the dry patch.

While the circular microchannel tends to lead to a stable liquid film (there might be some arising from the vapor shearing the liquid film), the rectangular channel tends to lead to an unstable liquid film most of the time. The evolution of the microchannel outlet liquid film profile in time is shown in

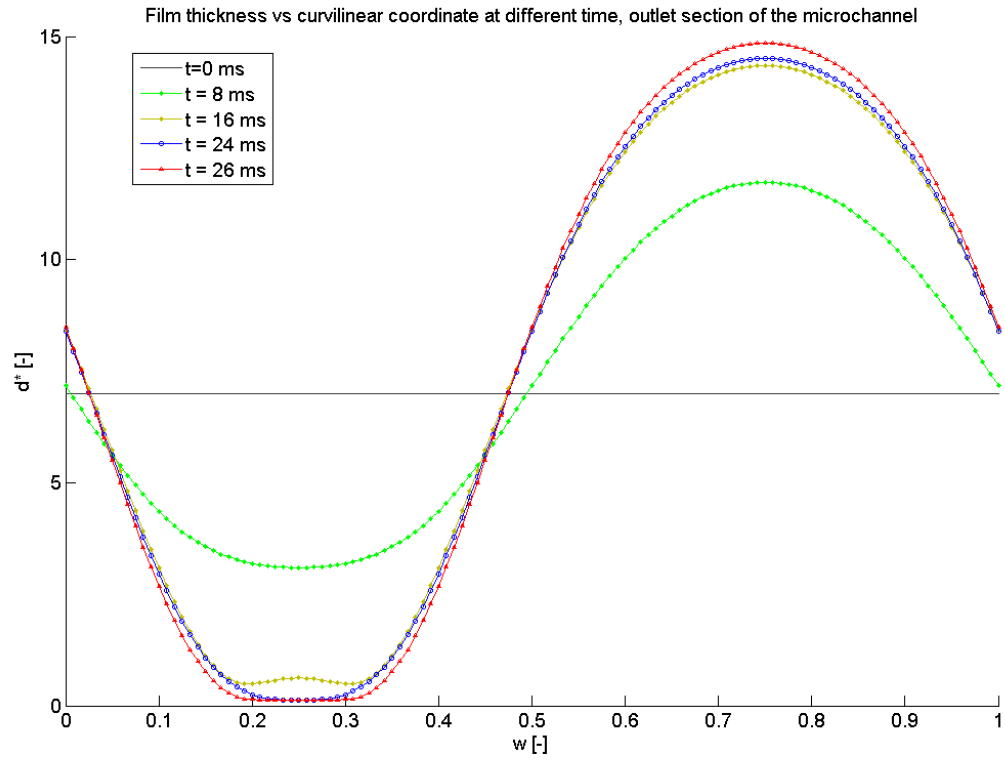


Figure 6.11: Film thickness profile at outlet of microchannel at different times,  $Dh = 1.03\text{ mm}$ , R134a at  $31^\circ$

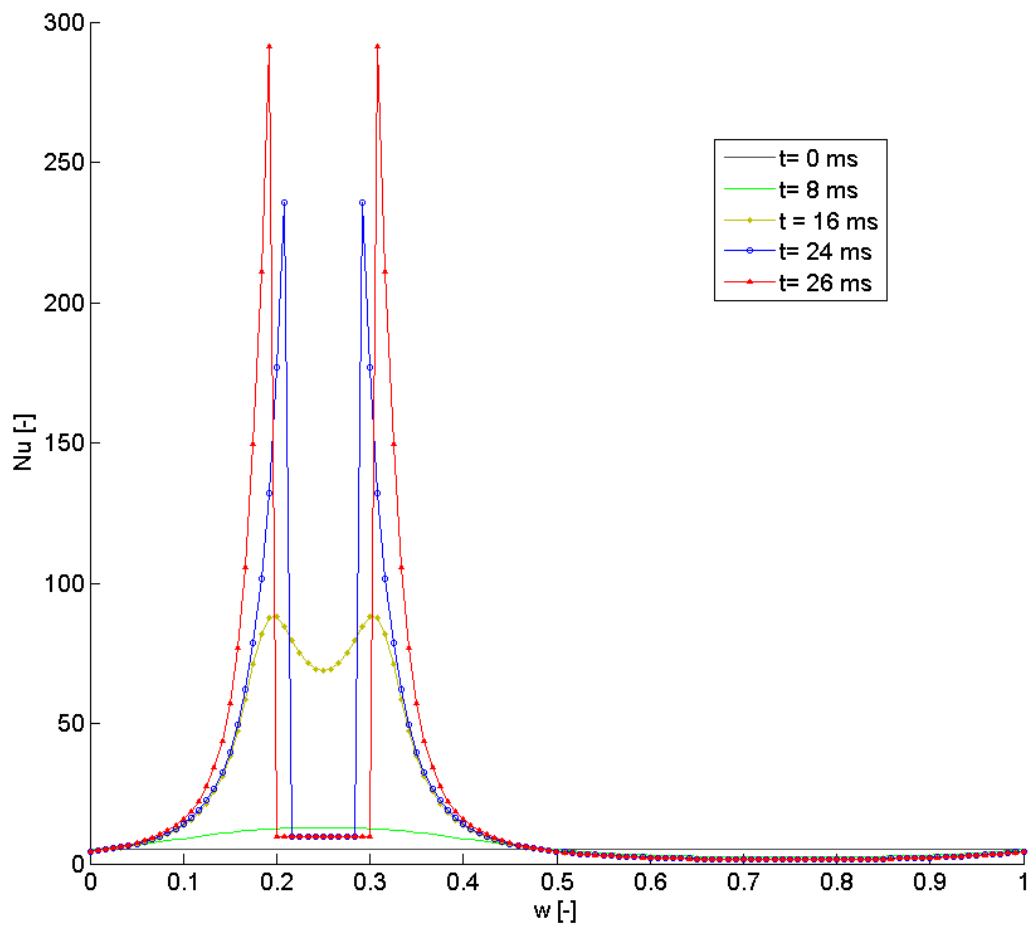


Figure 6.12: Local Nusselt number at outlet of microchannel at different times,  $Dh = 1.03\text{ mm}$ , R134a at  $31^\circ$

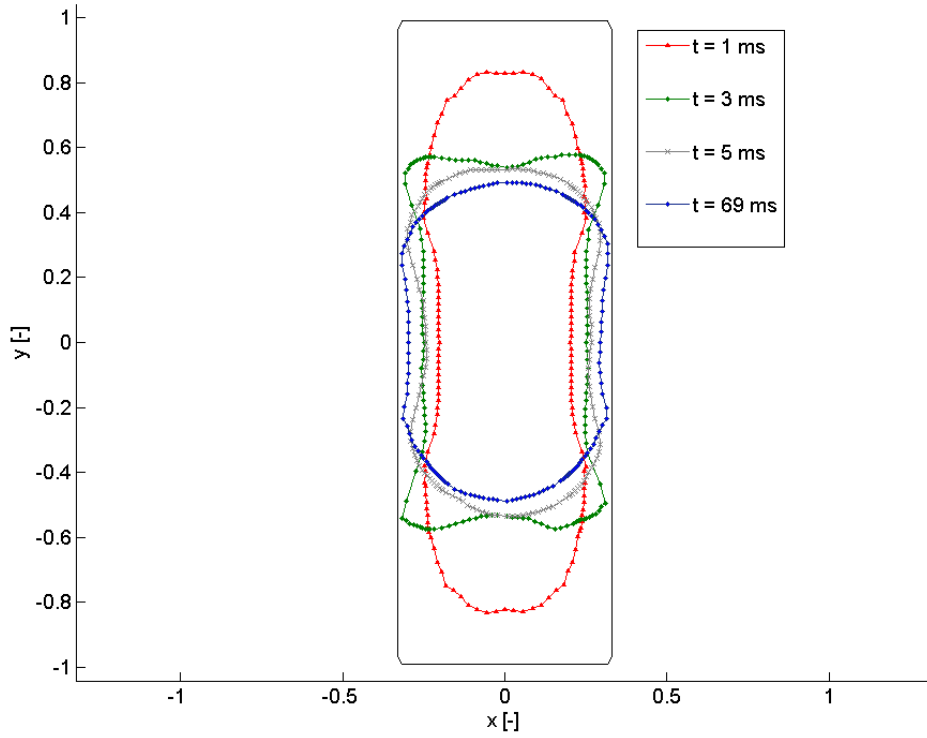


Figure 6.13: Liquid vapor interface at outlet of microchannel at different times,  $Dh = 1\text{ mm}$ , R-245fa at  $31^\circ$

Fig. 6.13 and Fig. 6.13 for R-245fa and CO<sub>2</sub>. A clear behavior that we can see, as mentioned earlier, is the appearance of circumferential disturbances due to the combined effects of capillary forces and liquid-vapor interface mass transfer. In particular, the CO<sub>2</sub> displays a more unstable behavior than R245fa. It is interesting to notice that the Interface mass transfer number for CO<sub>2</sub> is  $4.89e^{-5}$  while for R245fa it is  $2.72e^{-4}$  which might be a factor that will foster the instability. We can also notice the creation of local fluid patches on the sides of the microchannel than can eventually detach from the remaining of the liquid film. For rectangular channel, the aspect ratio plays a critical role in counter balancing the instability as very high aspect ratio will foster a capillary dominated regime compared to a regime with thermo capillary instabilities.

The impact of the instability on the overall heat transfer performance is not only negative. Indeed, the instability can prevent the creation of dry patches by favoring the rewetting of the latter, thus preventing a critical drop of the heat transfer coefficient. However, when the liquid fully wets the walls, the interfacial waves occurring at the liquid-vapor interface are likely to reduce the overall heat transfer performance as no thin films (with low thermal resistance) will be created. As such, we are more likely to observe a heat transfer coefficient that varies little with vapor quality. Currently, little agreement has been found experimentally regarding the trend of the heat transfer coefficient in microchannels at high vapor qualities and when capillary effects become important. While for macrochannels, the heat transfer coefficient increases with vapor quality, different studies have found a reduction of the heat transfer coefficient in microchannels (while others have found an increase). Different

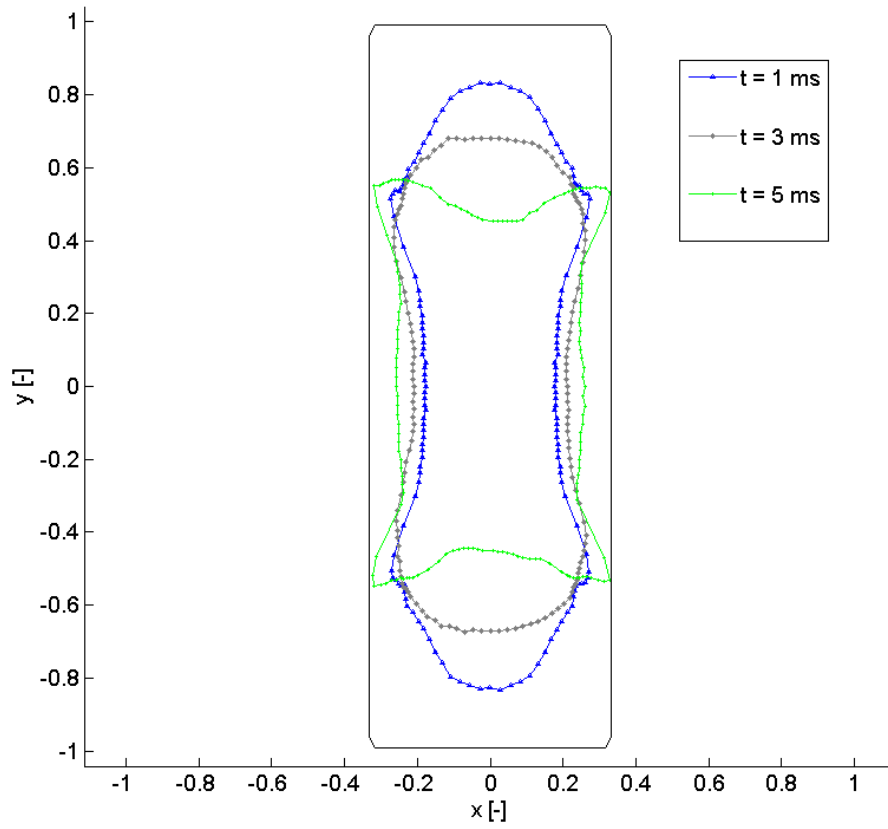


Figure 6.14: Liquid vapor interface at outlet of microchannel at different times,  $Dh = 1\text{ mm}$ ,  $\text{CO}_2$  at  $10^\circ$

Authors	Shape	$D_h$ [mm]	Fluid	Saturation Temperature <sup>o</sup> K	$G$ [ $\frac{kg}{m^2s}$ ]	Imposed Heat flux [ $\frac{kW}{m^2}$ ]	Onset of dryout	Heat transfer coefficient trend	Ir Ir
Saitoh <i>et al.</i> (2005)	Circular	3.1	R134a	278	15	12	0.9	flat	0.063
	Circular	3.1	R134a	278	300	12	0.9	flat	0.063
	Circular	3.1	R134a	278	300	24	0.9	flat	0.0532
	Circular	1.2	R134a	283	150	13	0.7	increases	0.1717
	Circular	1.2	R134a	283	300	13	0.85	increases	0.1717
	Circular	1.2	R134a	283	300	27	0.85	increases	0.1430
	Circular	0.5	R134a	288	150	15	0.45	increases	0.3711
	Circular	0.5	R134a	288	300	15	0.45	increases	0.3711
	Circular	0.5	R134a	288	300	29	0.45	increases	0.3147
Lin <i>et al.</i> (2001)	Circular	1.00	R141b	305.5	510	18	0.6	increases	0.056
	Circular	1.00	R141b	305.5	510	23	0.6	increases	0.053
	Circular	1.00	R141b	305.5	510	30	0.6	increases	0.050
	Circular	1.00	R141b	305.5	510	36	0.6	flat	0.047
	Circular	1.00	R141b	305.5	510	42	0.6	decreases	0.046
	Circular	1.00	R141b	305.5	510	48	0.6	decreases	0.044
	Circular	1.00	R141b	305.5	510	53	0.6	decreases	0.043
	Circular	1.00	R141b	305.5	510	59	0.6	decreases	0.042
	Circular	1.00	R141b	305.5	510	64	0.6	decreases	0.041

Table 6.3: Heat transfer coefficient trends observed at high vapor qualities and corresponding interfacial resistance number

explanations included the existence of remaining liquid slugs that did not completely evaporate while others assume partial dryout occurs and reduces the performance. It is interesting to compare, from a purely qualitative perspective, the trends observed by different researchers and their corresponding interfacial mass transfer number. It is interesting to notice from Tab. 6.3 that for a given fluid, the heat transfer coefficient seems to (1) increase with respect to vapor quality for higher values of the interface mass transfer number (2) reach a dry out state at higher vapor qualities when the interface mass resistance number decreases. While not giving a quantitative explanation of the trend of the heat transfer coefficient at higher vapor qualities, the interface mass transfer number can provide a rough estimate of how the convective boiling process would behave at higher vapor qualities.

### 6.2.1 Bubbly flows and elongated bubbles in microchannels

The numerical model for annular flows provides an interesting perspective on how to efficiently design micro heat exchangers at high vapor qualities. Yet, most applications that use convective boiling stay within the lower vapor quality boundaries in order to keep a security margin before dryout occurs. While annular flows take advantage of the combined effects of falling film evaporation and shear driven flows, convective boiling in the isolated bubble and coalescing bubble regime takes advantage of different parameters, such as the frequency of generation of the bubbles, the bubble nose film thickness or the bubble length. As shown in the previous section, our model accurately predicts the heat transfer behavior of convective boiling from the nucleation to the onset of the coalescing bubble regime space. The current model is able to simulate the heat transfer and bubble growth process of 1 to several thousands of consecutive bubbles, making this particularly interesting as it can model the behavior of either an elongated bubble flowing downstream with a thin, low thermal resistance, liquid film forming between the bubble and the wall, or many consecutive bubbles growing at the onset of the nucleation process and highly dependent on the nucleation frequency. It is interesting to investigate the influence of a certain number of parameters on the overall efficiency of the micro



Shape	$D_h$ [ $\mu m$ ]	Fluid	Saturation Temperature <sup>o</sup> C	Heat flux [ $kW/m^2$ ]	$G$ [ $\frac{kg}{m^2s}$ ]	Frequency of nucleation [Hz]
Circular	500	R245fa	31	40	400	29
Circular	500	R245fa	31	40	400	48
Circular	500	R245fa	31	40	400	59
Circular	500	R245fa	31	40	400	85

Table 6.4: Influence of frequency on overall heat transfer coefficient, input parameters

heat exchanger and in particular the modeled base temperature which will be an output of critical importance for real applications.

The current section will include an analysis of the following parameters:

- Effect of bubble frequency on the heat transfer coefficient
- Effect of wall material on single elongated bubble and multiple bubble
- Startup process and transient modes

In the first case, we consider a 1 cm long single microchannel with the following operating conditions: The local heat transfer coefficient is given in Fig. 6.15 for different inlet frequencies (given by the nucleation frequency). We can clearly notice that the higher frequencies lead to a higher heat transfer coefficient. At such low frequencies, it is interesting to compare the obtained heat transfer coefficient with the single phase flow equivalent (in this case around 1500). The bubbles at the lowest frequency have a very little impact on the overall heat transfer coefficient. The increase that we can see in the region above 0.5 points out to a growing bubble with lower initial thickness and therefore higher heat transfer coefficient. The next graph, Fig. 6.16 shows the axial wall temperature for two different materials, silicon and copper. Both simulations have been run under the same operating conditions, namely the same as in Tab. 6.4 for a frequency of 49 Hz. As expected, the silicon leads to a higher temperature gradient between the inlet and outlet section of the microchannel due to the lower thermal conductivity. The high temperature gradient between the regions with elongated bubbles (the high heat transfer regions) and the regions where bubbles nucleate is large. Therefore, axial wall conductivity should be taken into account in the current cases as the bubbles downstream will cool down the wall upstream. In the case of higher frequencies, we should tend towards a more stable and flat temperature profile with negligible axial conduction. Finally, the evolution of the wall temperature from an initial single phase flow state with large wall superheat to a low bubble frequency heat transfer is given in Fig 6.17. The time needed for the wall to reach a steady state temperature cannot be neglected for both the copper wall and the silicon wall cases.

The current chapter has permitted the identification of a certain number of important phenomena in microchannel heat transfer using the two different models for annular flows and bubbly/slug flows. As a general summary, it can be derived from the analysis above that:

- The turbulent eddy diffusivity for heat can play a critical role in enhancing heat transfer in microchannels
- The design of microchannels for evaporating annular flows does not follow the same rules as for annular condensing flows. It is advisable to focus on circular channels (in particular vertical

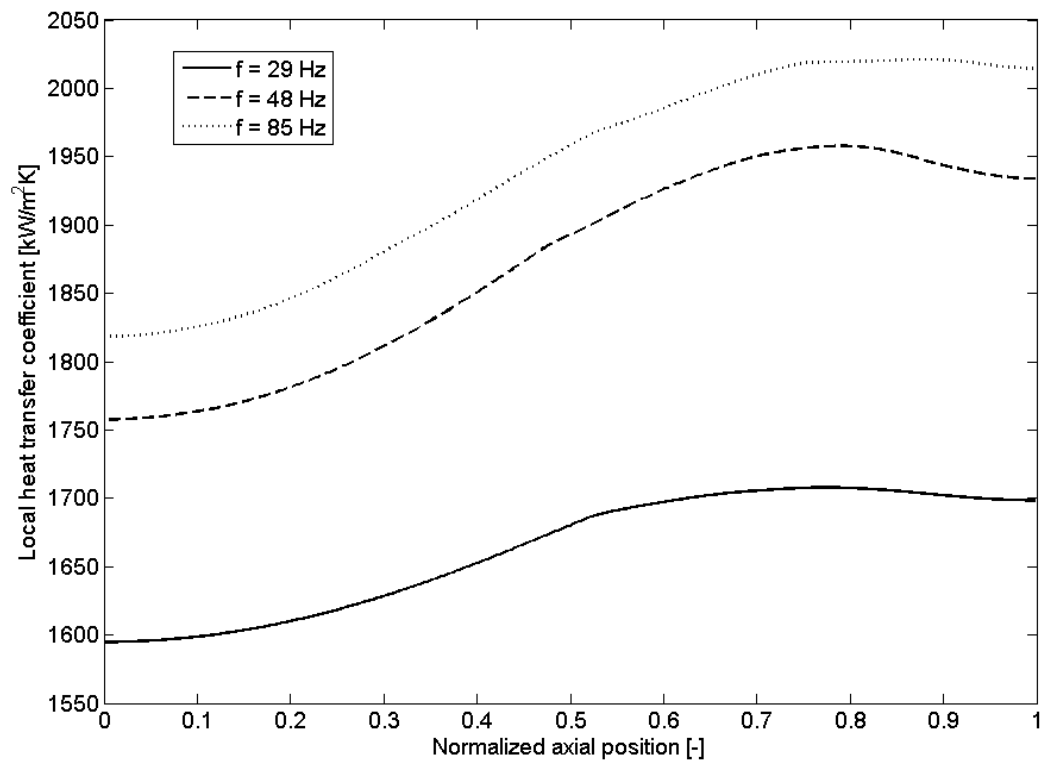


Figure 6.15: Local heat transfer coefficient for bubble frequencies 29-85 Hz

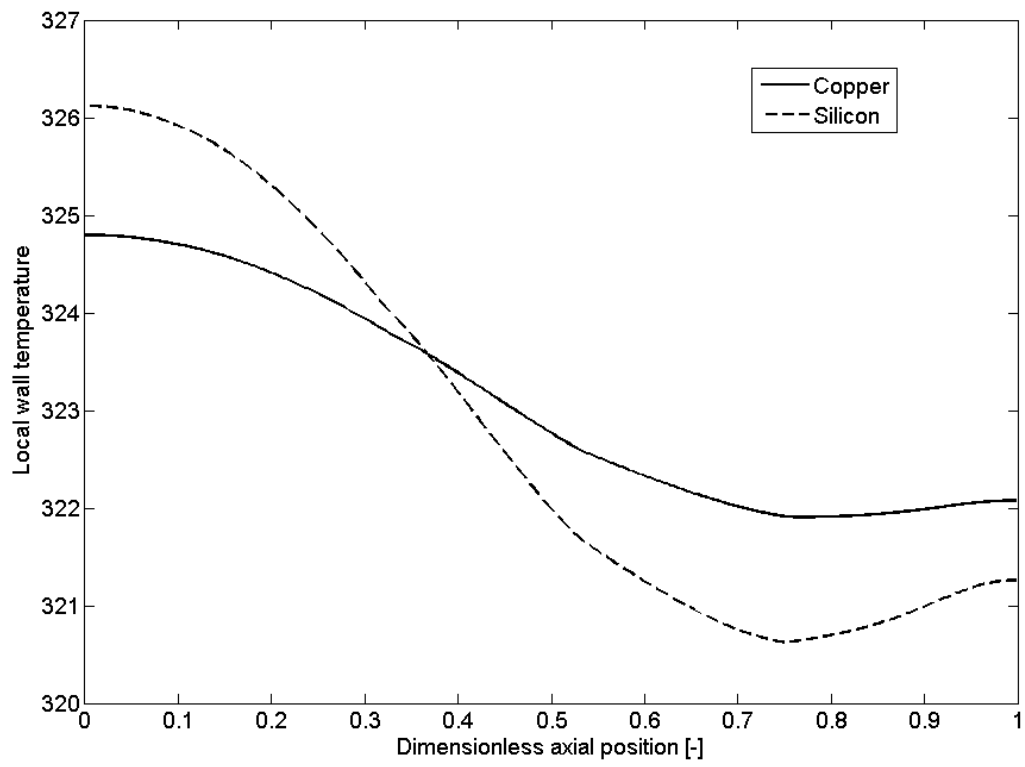


Figure 6.16: Wall temperature profile at  $t = 2s$  for copper and silicon microchannels

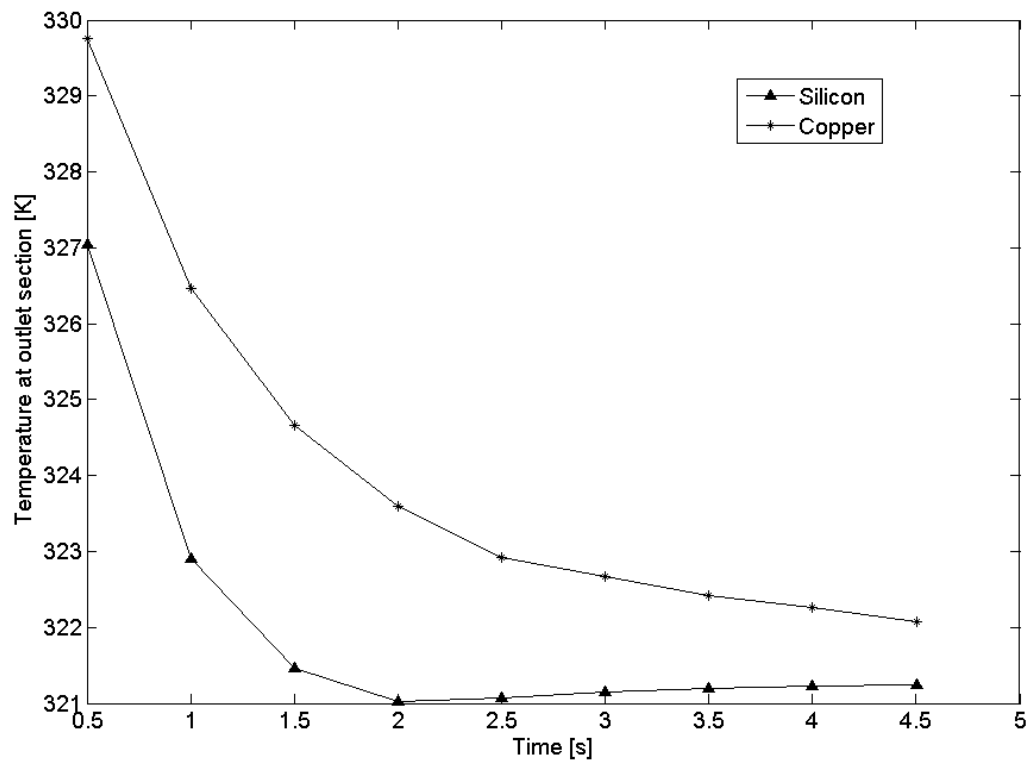


Figure 6.17: Start up phase, wall temperature variation with time

orientation) in order to (i) avoid thermo capillary instabilities (ii) avoid the creation of local dry patches

- Nucleation frequency at low vapor qualities plays a critical role for understanding the behavior of the heat transfer coefficient.



## 7 Conclusions

A pragmatic numerical model was developed for predicting the heat transfer and fluid flow behavior in microchannels for evaporating and condensing flows in the annular and isolated bubble regime. The results were validated against a large set of experimental data for different fluids and operating conditions, originating from different laboratories. The models developed included in particular:

- **Treatment of turbulent evaporating and condensing liquid films**
- **Treatment of evaporating annular flows, including dry patch formation**
- **Simulation of isolated bubbles and elongated bubbles in microchannels**

The models were later used to critically assess the influence of a certain number of parameters relevant to the engineer when considering the design of a new microchannel heat exchanger. The key outcomes of the design can be summarized as follows:

- The role of turbulent liquid films : turbulent liquid films lead to a very different heat transfer behavior compared to laminar liquid films, their existence must therefore be considered during the design process. While in the case of laminar liquid films, capillary forces are beneficial due to the creation of a very low resistance liquid film on the sides of the channel, in the case of turbulent liquid films, the turbulent eddy diffusivity for heat will occurring at the thickest regions of the thin film, will promote the heat transfer.
- The role of dry patches in evaporating annular flows : The microchannel geometry can influence the reduction of the heat transfer performance at high vapor qualities through one of the following modes: (i) by the creation of a local dry patch from the drying out of the liquid film (effect that can be promoted by the capillary forces or gravity forces) (ii) by the creation of an unstable liquid film with eventual transient dry patch creation. The first case is likely to lead to lead the heat exchanger to a critical condition as the temperature rise will hardly be counter balanced. In the second case, the overall performance will be reduced as the vapor quality increases but we should not see a steep decrease of heat transfer coefficient until reaching very high levels of vapor qualities (close to 1). Circular channels will tend to have a stable liquid film dominated by shear forces down to small diameters, however, gravity forces can play an important role and favor the appearance of dry patches. Non-circular channels will tend to

develop highly unstable liquid films as there will be competition between the capillary forces and the evaporating mass fluxes. Through, the impact on the heat exchanger performance should not be critical as it is likely that local dry patches are re-wetted as soon as they are created. The unstable liquid film is likely to lead to a flat behavior of the heat transfer coefficient with respect to vapor quality in the annular flow regime.

- Influence of bubble frequency : At low vapor qualities, the frequency of nucleation plays an important role on the overall heat transfer and can determine the initial trends of the heat transfer coefficient. We can consider two different cases (i) a low frequency nucleation, where the bubble will elongate through vaporisation (ii) a high frequency process where bubbles will coalesce quickly, leading to longer and more thermally efficient bubbles. In the second case, it is likely that the heat transfer coefficient at the lowest vapor qualities will be high. Noting that the frequency of nucleation depends on the thermo-physical properties of the fluid and the wall superheat, the trend of the heat transfer coefficient at low vapor qualities will shall be flatter when the nucleation frequency is higher

Several models can be found in the literature that try to predict and describe the heat transfer and fluid flow behavior in microchannels. These models can either be fully empirical models, include some light physical analysis and thus be called mechanistic models, or be fully numerical models. Unfortunately, none of these models is currently able to cover a large range of experimental and operating conditions. For instance, most empirical models perform very poorly when applied to other operating conditions than the ones they were correlated with. A few mechanistic models were develop that do predict well and quickly heat transfer and fluid flow data but again they hardly cover several flow pattern regimes. Full numerical models do provide a meaningful analysis of the local fluid flow and heat transfer behavior but are not practical for design purposes due to their computational cost. The approach proposed in the current thesis and initiated by Nebuloni and Thome [32] tries to merge the benefits of all modeling approaches in order to reduce computational cost while still capturing enough fluid flow and heat transfer characteristics to develop design and optimization works and covering the most important flow regimes and operating conditions. While it is dependent on many empirical models, which generally lead to a higher uncertainty, the current pragmatic code is flexible enough to allow the implementation of new approaches and methods.

A natural continuation to the study carried out so far would be to merge both the annular code and the slug/elongated bubbles code in order to be able to capture the effects of the microchannel geometry on the evolution of the bubble itself. Furthermore, more research would have to be done for mapping the different evaporating annular flow regimes depending on the microchannel geometry and the boundary conditions. Finally, geometrical consideration, in particular for evaporating annular flows, could be used to improve existing mini/macro scale correlations in order to account for the characteristics of small scale forces.



## A Color function calculation

The geometric problem of reconstructing a volume cut by a plane is considered. It is used for the calculation of the volume fraction of vapor to liquid at the three phase lines and therefore tracking the position of the contact line. in the current case, the volume considered is an arbitrary defined volume that identifies the dry zones where direct wall to vapor convection occurs. In particular, due to the particular geometry of our control volumes, we need to adapt and approach that was proposed by Scardovelli and Zaleski [45]. Fig. A.1 shows the three dimensional parallelepiped in the local reference system of the wall. A plane crossing the arbitrary control volume can be defined by the equation:

$$m_1 x_1 + m_2 x_2 + m_3 x_3 = \alpha \quad (\text{A.1})$$

where  $\alpha$  is a constant related to the smallest distance from the origin. The vapor to liquid volume ratio is calculated based on Fig. A.1. The arbitrary hexaedron of thickness  $\delta_{min}$  is used as reference to calculate the color function or volume of vapor to volume of liquid ratio. The color function can be stated as:

$$\frac{1}{C} = \frac{V_{\delta_{lim}} - V_{GLSBTMJIHK}}{V_{MNLGKHIJ}} \quad (\text{A.2})$$

and the contact angle can be linked to the normal vector to the plane through:

$$\tan\theta = \frac{\sqrt{m_1^2 + m_2^2}}{m_3} \quad (\text{A.3})$$

The plane DCNA intersects the arbitrary hexaedron  $\Omega_{i,j}$  and is characterized by a normal unit vector  $[m_1, m_2, m_3]$  which in our case is given by the contact angle calculation. it is possible to calculate the volume of vapor  $NBTS$  by removing the tetrahedrons  $AHOPQ$  and  $CJRP$  to the tetrahedron  $DKRO$  that is reconstructed from the plane  $DABC$ . The Volume of  $DORK$  can be stated as:

$$V_{DORK} = \frac{\alpha^3}{6m_1 m_2 m_3} \quad (\text{A.4})$$

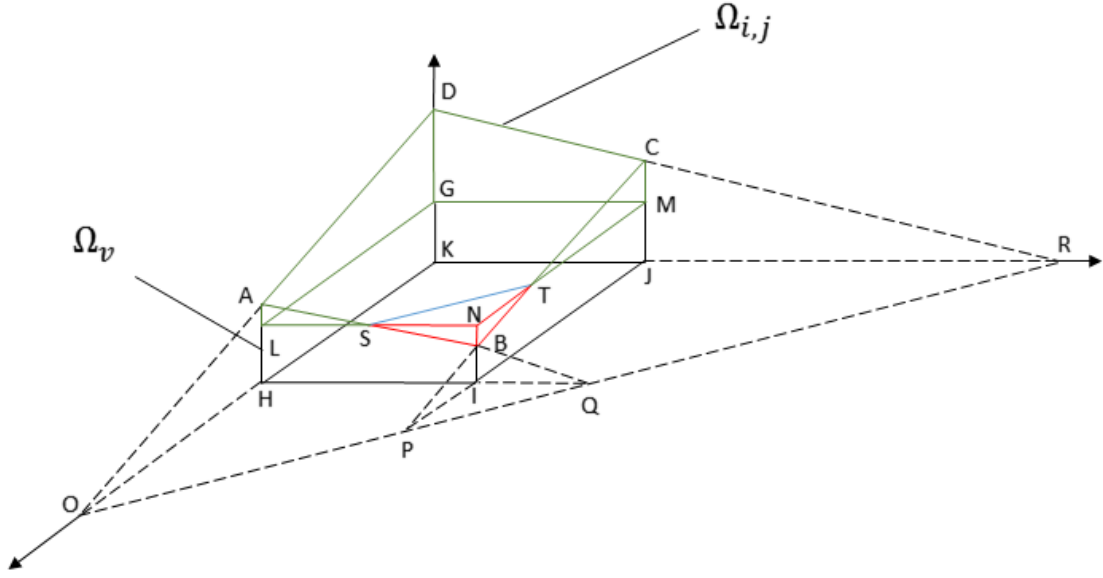


Figure A.1: Vapor to liquid ratio

where  $\alpha$  is the distance to the local reference point. The volume of the tetraedrons  $V_{AHOQ}$ ,  $V_{CRJP}$ ,  $V_{BQPI}$  and  $V_{DORK}$  can be calculated:

$$V_{AHOQ} = V_{DORK} * \left(1 - \frac{m_1 L_{KH}}{\alpha}\right)^3 \quad (\text{A.5})$$

$$V_{CRJP} = V_{DORK} * \left(1 - \frac{m_2 L_{KJ}}{\alpha}\right)^3 \quad (\text{A.6})$$

$$V_{BQPI} = V_{DORK} * \left(1 - \frac{m_1 L_{KH}}{\alpha} - \frac{m_1 L_{KH}}{\alpha}\right)^3 \quad (\text{A.7})$$

$$V_{DORK} = \frac{\alpha^3}{6m_1 m_2 m_3} \quad (\text{A.8})$$

The volume  $DABCJKHI$  and  $BNST$  can then be reconstructed:

$$V_{DABCJKHI} = V_{DORK} - V_{CRJP} - V_{AHOQ} + V_{BQPI} \quad (\text{A.9})$$

$$(\text{A.10})$$

We can distinguish three distinct cases, each one requiring different calculations but the methodology can be the same as the one mentioned above:

- $CJ > MJ$  and  $AH > LH$  in which case only 1 corner will be below  $\delta_{min}$

- $AH > LH$  and  $CJ < MJ$  in which case 2 corners will be below  $\delta_{min}$
- $AH < LH$  and  $CJ < MJ$  in which case 3 corners will be below  $\delta_{min}$

Once the ratio of volume of vapor to volume of liquid is calculated, the position of the contact line can be interpolated based on the neighboring color functions and therefore the adapted surface tension model that takes into account the contact angle can be added to the model.



## B Laminar and turbulent liquid films

Similarly to liquid films in high speed bearings, we can apply the lubrication theory to a thin film subject to a large shear stress from the vapor core.

While lubrication theory has widely been used in laminar conditions, extensively explained by [36] and applied in the literature, this theory is used to describe the flow in a geometry which one dimension is significantly smaller. Mathematically, we exploit the disparity between two length scales (the characteristic film thickness and the substrate length scales). In the current scenario, our thin film can be either laminar or turbulent. While the laminar case is well known, the turbulence case was introduced for studying high speed bearings where a lubricant is trapped between the rotating cylinder and the base. By using an algebraic model provided by Cioncolini and Thome [12] that relates the eddy diffusivity for momentum and heat to the film thickness (based on the premise that the thin film is mainly shear driven by the vapor core), we are able to obtain the mean flow equations for a thin film.

The momentum equation for a thin turbulent film can be stated as:

$$(\mu_l + \mu_t) \frac{\partial^2 u}{\partial y^2} = \frac{\partial p}{\partial x} - \rho_l g \quad (\text{B.1})$$

where the turbulent viscosity is given by the eddy diffusivity for momentum model for annular flows

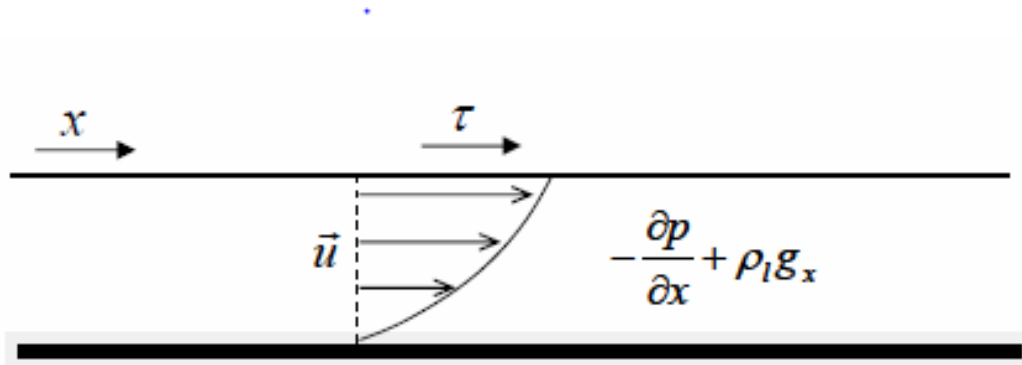


Figure B.1: Liquid film velocity profile

of Cioncolini and Thome [12]

$$1 + v_t^+ = 0.033 t^+ \quad (\text{B.2})$$

where  $v_t^+ = \frac{\mu_t}{\mu_l}$  and  $t^+$  can be compared to a local liquid film Reynolds number with  $V^* = \sqrt{\frac{\tau_w}{\rho_l}}$  as the characteristic velocity and the local film thickness as the characteristic dimension. Considering that the turbulent eddy diffusivity for heat is only a function of the liquid film thickness, the liquid film profile can easily be integrated:

$$u(y) = \frac{\tau_w y}{\mu_l + \mu_t} - \frac{1}{2(\mu_l + \mu_t)} \left( \frac{\partial p}{\partial x} - \rho_l g \right) \delta^2 \left[ 2 \frac{y}{\delta} - \left( \frac{y}{\delta} \right)^2 \right] \quad (\text{B.3})$$

The average velocity can be integrated as:

$$U_{av} = \int_0^\delta u(y) dy = \frac{\tau \delta}{2(\mu_l + \mu_t)} - \frac{1}{3\mu_l} \left( \frac{\partial p}{\partial x} - \rho_l g \right) \delta^2 \quad (\text{B.4})$$

and the wall shear can be expressed as a function of the bulk velocity where:

$$\tau_w = \mu_l \frac{\alpha U_{av}}{\delta} \quad (\text{B.5})$$

In the fully laminar case, the expression for  $U_{av}$  can be obtained by combining B.4 and B.5 while in the turbulent case, an empirical correlation connecting  $\tau$  and  $U_{av}$  is used:

$$f_{tp} = 0.0196 We_v^{-0.372} Re_l^{0.318} \quad (\text{B.6})$$

where the vapor Weber number is used:

$$We_v = \frac{\rho_v U_v^2 D_{hv}}{\sigma} \quad (\text{B.7})$$

and the liquid film Reynolds number is defined as:

$$\frac{\rho_l \delta U_l}{\sigma} \quad (\text{B.8})$$

## C Thin film integral model

The model used for the integral of the total heat transfer and evaporative mass flux in the thin-film region comes from the analytical solution provided by Wang *et al.* [54]. As mentioned earlier, when a liquid film wets a wall, the extended meniscus can be divided in three regions, a non-evaporating region, a thin-film and an intrinsic meniscus. The thin-film region is characterized by a very low thermal resistance and therefore high heat transfer rates, the intrinsic meniscus is dominated by capillary forces and the adsorbed layer is dominated by inter molecular forces. The augmented Young-Laplace equation, giving the pressure difference between the vapor and liquid, can be stated as:

$$P_v = P_l + P_c + P_d \quad (\text{C.1})$$

where  $P_c$  is the capillary pressure  $P_c = \sigma K$  and  $P_d$  is the disjoining pressure given by  $P_d = A/\delta^3$ . The liquid vapor interface curvature is given by  $K = \delta''(1 + \delta'^2)^{-1.5}$ . The previous equations let us obtain a third-order differential equation governing the liquid film profile  $\delta(x)$ :

$$\delta''' - \frac{3\delta'\delta''^2}{1 + \delta'^2} + \frac{1}{\sigma} \left( \frac{dP_l}{dx} - \frac{3A}{\delta^4} \delta' \right) (1 + \delta'^2)^{1.5} \quad (\text{C.2})$$

The lubrication theory can be applied considering the large length-to-height ratio of the liquid film. Assuming a no slip boundary condition at the wall and a no shear boundary condition at the liquid-vapor interface, the pressure gradient can be derived as a function of the the evaporative mass flux:

$$\frac{dP_l}{dx} = \frac{3v}{\delta^3} \int_{-\text{inf}}^x m'' dx \quad (\text{C.3})$$

Injecting Eq. C.3 Eq. C.2 we obtain the well established fourth order differential equation governing the liquid film profile.

$$\frac{d}{dx} \left( \left[ \frac{\sigma\delta'''}{(1 + \delta'^2)^{2.5}} - \frac{3\sigma\delta'\delta''^2}{(1 + \delta'^2)^{2.5}} - \frac{3A\delta'}{\delta^4} \right] \right) = -m'' \quad (\text{C.4})$$

The solution of the equation gives the location and length of the region of interest, the thin-film region.

It is commonly stated that the end of the thin film region (before entering the intrinsic meniscus region) is when the total pressure falls below  $1/2000^{th}$  of the disjoining pressure  $P_d$ , meaning that wall molecules do no longer feel the 'presence' of vapor molecules. The simplification proposed by Wang *et al.* assumes the following:

- The thin-film region is supported by the disjoining pressure, which drops from the non-evaporating region to the intrinsic meniscus and allows the liquid to flow into the liquid film to compensate evaporation.
- The evaporation mass flux is calculated using the simplified expression of Wayner *et al.* [58] that assumes the temperature at the liquid vapor interface  $T_{lv} \approx T_v$ .

From the lubrication theory, the mass flow rate at a position  $x$ ,  $m'(x)$  may be obtained:

$$m'(x) = \frac{A}{\delta v} \left( \frac{d\delta}{dx} \right) \quad (C.5)$$

which is equal to the integral of the evaporative mass flux from the non-evaporating region to the position  $x$ . Thus we obtain the total heat dissipated from the non-evaporating region to the position  $x$ :

$$q(x) = m'(x) \Delta h_{lv} \quad (C.6)$$

Then, by solving C.4, deriving the gradient of the liquid film profile with respect to  $x$ , and setting  $\delta$  to infinity lets us obtain the total heat transfer from the thin-film region:

$$q_t = \sqrt{\frac{2A h_{tf} \Delta h_{lv} (T_w - T_v)}{v}} \ln \left( \frac{k_l}{h_{tf} \delta_0} + 1 \right) \quad (C.7)$$

where  $h_{tf}$  is the thin-film heat transfer coefficient given by:

$$h_{tf} = C \left( \frac{M}{2\pi R T_{lv}} \right)^{1/2} \frac{P_v M \Delta h_{lv}}{R T_v T_{lv}} \quad (C.8)$$

The total mass transfer through the liquid-vapor interface in the thin film region can therefore be defined as:

$$m' = \frac{1}{\Delta h_{lv}} q_t \quad (C.9)$$

The total mass flux to be added as an additional evaporative term to the cells crossed by a contact line is the integral of Eq. C.9 over the segment of contact line of the concerned cell.



# Bibliography

- [1] S. Afkhami, S. Zaleski, and M. Bussmann. A mesh-dependent model for applying dynamic contact angles to VOF simulations. *Journal of Computational Physics*, 228(15):5370–5389, Aug. 2009.
- [2] A. Agarwal, T. M. Bandhauer, and S. Garimella. Measurement and modeling of condensation heat transfer in non-circular microchannels. *International Journal of Refrigeration*, 33(6):1169–1179, Sept. 2010.
- [3] B. Agostini, A. Bontemps, and B. Thonon. Effects of Geometrical and Thermophysical Parameters on Heat Transfer Measurements in Small-Diameter Channels. *Heat Transfer Engineering*, 27(1):14–24, Jan. 2006.
- [4] B. Agostini, J. R. Thome, M. Fabbri, B. Michel, D. Calmi, and U. Kloter. High heat flux flow boiling in silicon multi-microchannels – Part I: Heat transfer characteristics of refrigerant R236fa. *International Journal of Heat and Mass Transfer*, 51(21-22):5400–5414, Oct. 2008.
- [5] T. M. Bandhauer, A. Agarwal, and S. Garimella. Measurement and Modeling of Condensation Heat Transfer Coefficients in Circular Microchannels. *Journal of Heat Transfer*, 128(10):1050, 2006.
- [6] A. E. Bergles, J. H. Lienhard V, G. E. Kendall, and P. Griffith. Boiling and Evaporation in Small Diameter Channels. *Heat Transfer Engineering*, 24(1):18–40, Jan. 2003.
- [7] S. S. Bertsch, E. a. Groll, and S. V. Garimella. A composite heat transfer correlation for saturated flow boiling in small channels. *International Journal of Heat and Mass Transfer*, 52(7-8):2110–2118, Mar. 2009.
- [8] S. Bortolin, E. Da Riva, and D. Del Col. Condensation in a Square Minichannel: Application of the VOF Method. *Heat Transfer Engineering*, 35(February 2015):193–203, 2014.
- [9] Brackbill J.U. A continuum method for modeling surface tension, 1991.
- [10] S. Churchill. Friction-factor equation spans all fluid-flow regimes, Chem. Eng. 84 (1977) 91–92. *Chemical Engineering*, 84:91–92, 1977.
- [11] A. Cioncolini and J. R. Thome. Algebraic turbulence modeling in adiabatic and evaporating annular two-phase flow. *International Journal of Heat and Fluid Flow*, 32(4):805–817, Aug. 2011.

- [12] A. Cioncolini, J. R. Thome, and C. Lombardi. Algebraic turbulence modeling in adiabatic gas–liquid annular two-phase flow. *International Journal of Multiphase Flow*, 35(6):580–596, June 2009.
- [13] A. Cioncolini, J. R. Thome, and C. Lombardi. Unified macro-to-microscale method to predict two-phase frictional pressure drops of annular flows. *International Journal of Multiphase Flow*, 35(12):1138–1148, Dec. 2009.
- [14] J. W. Coleman and S. Garimella. Characterization of two-phase flow patterns in small diameter round and rectangular tubes. *International Journal of Heat and Mass Transfer*, 42:2869–2881, 1999.
- [15] J. W. Coleman and S. Garimella. Two-phase flow regimes in round , square and rectangular tubes during condensation of refrigerant R134. *International Journal of Refrigeration*, 26:117–128, 2003.
- [16] L. Consolini and J. R. Thome. A heat transfer model for evaporating microchannel coalescing bubble. (May):3–7, 2009.
- [17] L. Consolini and J. R. Thome. A heat transfer model for evaporation of coalescing bubbles in micro-channel flow. *International Journal of Heat and Fluid Flow*, 31(1):115–125, Feb. 2010.
- [18] E. Costa-Patry and J. R. Thome. Flow pattern-based flow boiling heat transfer model for microchannels. *International Journal of Refrigeration*, 36(2):414–420, Mar. 2013.
- [19] E. Da Riva and D. Del Col. Numerical Simulation of Laminar Liquid Film Condensation in a Horizontal Circular Minichannel. *Journal of Heat Transfer*, 134(May 2012):051019, 2012.
- [20] E. Da Riva, D. Del Col, S. V. Garimella, and A. Cavallini. The importance of turbulence during condensation in a horizontal circular minichannel. *International Journal of Heat and Mass Transfer*, 55(13-14):3470–3481, June 2012.
- [21] D. Del Col, S. Bortolin, A. Cavallini, and M. Matkovic. Effect of cross sectional shape during condensation in a single square minichannel. *International Journal of Heat and Mass Transfer*, 54(17-18):3909–3920, Aug. 2011.
- [22] D. Del Col, D. Torresin, and a. Cavallini. Heat transfer and pressure drop during condensation of the low GWP refrigerant R1234yf. *International Journal of Refrigeration*, 33(7):1307–1318, Nov. 2010.
- [23] V. Dupont, J. R. Thome, and A. M. Jacobi. Heat transfer model for evaporation in microchannels. Part II: comparison with the database. *International Journal of Heat and Mass Transfer*, 47(14-16):3387–3401, July 2004.
- [24] T. Harirchian and S. V. Garimella. A comprehensive flow regime map for microchannel flow boiling with quantitative transition criteria. *International Journal of Heat and Mass Transfer*, 53(13-14):2694–2702, June 2010.
- [25] T. Harirchian and S. V. Garimella. Flow regime-based modeling of heat transfer and pressure drop in microchannel flow boiling. *International Journal of Heat and Mass Transfer*, 55(4):1246–1260, Jan. 2012.

- [26] T. Jiang, O. Soo-Gun, and J. Slattery. Correlation for dynamic contact angle. *Journal of Colloid and Interface Science*, 69(1):74–77, 1979.
- [27] S. G. Kandlikar. Heat Transfer Mechanisms During Flow Boiling in Microchannels. *Journal of Heat Transfer*, 126(1):8, 2004.
- [28] T. G. Karayiannis, D. Shiferaw, D. B. R. Kenning, and V. V. Wadekar. Flow Patterns and Heat Transfer for Flow Boiling in Small to Micro Diameter Tubes. *Heat Transfer Engineering*, 31(4):257–275, Apr. 2010.
- [29] S. Koyama. An experimental study on condensation of refrigerant R134a in a multi port extruded tube. *International Journal of Refrigeration*, 26(4):425–432, June 2003.
- [30] M. Matkovic, A. Cavallini, D. Del Col, and L. Rossetto. Experimental study on condensation heat transfer inside a single circular minichannel. *International Journal of Heat and Mass Transfer*, 52(9-10):2311–2323, Apr. 2009.
- [31] K. Moriyama and A. Inoue. Thickness of the liquid film formed by a growing bubble in a narrow gap between two horizontal plates. *Journal of Heat Transfer*, 118, 1996.
- [32] S. Nebuloni and J. R. Thome. Numerical modeling of laminar annular film condensation for different channel shapes. *International Journal of Heat and Mass Transfer*, 53(13-14):2615–2627, June 2010.
- [33] C. Ong and J. Thome. Macro-to-microchannel transition in two-phase flow: Part 1 – Two-phase flow patterns and film thickness measurements. *Experimental Thermal and Fluid Science*, 35(1):37–47, Jan. 2011.
- [34] C. Ong and J. Thome. Macro-to-microchannel transition in two-phase flow: Part 2 – Flow boiling heat transfer and critical heat flux. *Experimental Thermal and Fluid Science*, 35(6):873–886, Sept. 2011.
- [35] C. L. Ong and J. R. Thome. Flow boiling heat transfer of R134a, R236fa and R245fa in a horizontal 1.030mm circular channel. *Experimental Thermal and Fluid Science*, 33(4):651–663, Apr. 2009.
- [36] A. Oron, S. H. Davis, and S. G. Bankoff. Long-scale evolution of thin liquid films. 69(3), 1997.
- [37] M. S. Plesset and A. Prosperetti. Bubble dynamics and cavitation. *Annual Review of fluid mechanics*, 9:145–185, 1977.
- [38] M. S. Plesset and A. Zwick. The growth of vapor bubbles in superheated liquids. *Journal of applied physics*, 25(4):493–500, 1953.
- [39] X. Quan, P. Cheng, and H. Wu. Transition from annular flow to plug/slug flow in condensation of steam in microchannels. *International Journal of Heat and Mass Transfer*, 51(3-4):707–716, Feb. 2008.
- [40] A. Quarteroni. *Numerical methods for differential problems*. 2009.
- [41] a. Y. Rednikov and P. Colinet. Truncated versus extended microfilms at a vapor-liquid contact line on a heated substrate. *Langmuir : the ACS journal of surfaces and colloids*, 27(5):1758–69, Mar. 2011.

- [42] M. Renardy, Y. Renardy, and J. Li. Numerical Simulation of Moving Contact Line Problems Using a Volume-of-Fluid Method. *Journal of Computational Physics*, 171(1):243–263, July 2001.
- [43] R. Revellin, B. Agostini, and J. R. Thome. Elongated bubbles in microchannels. Part II: Experimental study and modeling of bubble collisions. *International Journal of Multiphase Flow*, 34(6):590–601, June 2008.
- [44] R. Revellin, V. Dupont, T. Ursenbacher, J. R. Thome, and I. Zun. Characterization of diabatic two-phase flows in microchannels: Flow parameter results for R-134a in a 0.5mm channel. *International Journal of Multiphase Flow*, 32(7):755–774, July 2006.
- [45] R. Scardovelli and S. Zaleski. Analytical Relations Connecting Linear Interfaces and Volume Fractions in Rectangular Grids. *Journal of Computational Physics*, 164(1):228–237, Oct. 2000.
- [46] Springer. *VDI-Warmeatlas*. Berlin, Heidelberg, 1997.
- [47] S. Szczukiewicz, N. Borhani, and J. R. Thome. Two-phase heat transfer and high-speed visualization of refrigerant flows in  $100 \times 100$   $\mu\text{m}$  silicon multi-microchannels. *International Journal of Refrigeration*, 36(2):402–413, Mar. 2013.
- [48] S. Szczukiewicz, M. Magnini, and J. Thome. Proposed models, ongoing experiments, and latest numerical simulations of microchannel two-phase flow boiling. *International Journal of Multiphase Flow*, 59:84–101, Feb. 2014.
- [49] L. Tanner. The spreading of silicone oil drops on horizontal surface. *Journal of applied physics*, 12(9):1473–1484, 1979.
- [50] J. Thome. *Engineering Databook III*. Wolverine Tube, Inc., 2008.
- [51] J. R. Thome. Boiling in microchannels: a review of experiment and theory. *International Journal of Heat and Fluid Flow*, 25(2):128–139, Apr. 2004.
- [52] T. N. Tran, M. W. Wambsganss, and D. M. France. Small circular and rectangular channel boiling with two refrigerants. *International Journal of Multiphase Flow*, 3(4):485–498, 1996.
- [53] F. Vakili-Farahani, B. Agostini, and J. Thome. Experimental study on flow boiling heat transfer of multiport tubes with R245fa and R1234ze(E). *International Journal of Refrigeration*, 36(2):335–352, Mar. 2013.
- [54] H. Wang, S. V. Garimella, and J. Y. Murthy. An analytical solution for the total heat transfer in the thin-film region of an evaporating meniscus. *International Journal of Heat and Mass Transfer*, 51(25-26):6317–6322, Dec. 2008.
- [55] H. S. Wang, S. V. Garimella, and J. Y. Murthy. Characteristics of an evaporating thin film in a microchannel. *International Journal of Heat and Mass Transfer*, 50(19-20):3933–3942, Sept. 2007.
- [56] H. S. Wang and J. W. Rose. A Theory of Film Condensation in Horizontal Noncircular Section Microchannels. *Journal of Heat Transfer*, 127(10):1096, 2005.
- [57] H. S. Wang and J. W. Rose. A Theory of Film Condensation in Horizontal Noncircular Section Microchannels. *Journal of Heat Transfer*, 127(10):1096, 2005.

- [58] P. C. Wayner, Y. K. Kao, and L. V. Lacroix. The interline heat-transfer coefficient of an evaporating wetting film. *International Journal of Heat and Mass Transfer*, 19:487–492, 1976.
- [59] T. Zhao and Q. Liao. Theoretical analysis of film condensation heat transfer inside vertical mini triangular channels. *International Journal of Heat and Mass Transfer*, 45(13):2829–2842, June 2002.



## Nicolas Antonsen

### PERSONAL DATA

Name	Nicolas Antonsen
Date of birth	20 <sup>th</sup> December, 1988
Birthplace	Barcelona, Spain
Nationality	French, Norwegian

### EDUCATION

2011-2015	<b>Doctoral student and assistant</b> , Laboratory of Heat and Mass Transfer, Swiss Federal Institute of Technology (EPFL), Lausanne
2006-2011	<b>Master of Science in Mechanical Engineering</b> , Laboratory of Heat and Mass Transfer, Swiss Federal Institute of Technology (EPFL), Lausanne

### WORK EXPERIENCE

2011-2014	<b>Swiss Federal Institute of Technology (EPFL), Laboratory of Heat and Mass Transfer, Lausanne</b> Research Assistant;
2013-2015	<b>ShARE Think-tank, Lausanne</b> Global President;

### PUBLICATIONS

N. Antonsen and J. R. Thome, Pragmatic numerical simulation of condensation and evaporation in microchannels, *Book Chapter*, Encyclopedia of Two-phase Heat Transfer and Fluid Flows, 2015

N. Antonsen and J. R. Thome, Pragmatic Numerical Modeling of Thermal Performance of a Microevaporator, Proceedings of the ASME 2015 12th International Conference on Nanochannels, Microchannels, and Minichannels, InterPACKIC-NMM2015, July 6-9, San Francisco, California, USA

N. Antonsen and J. R. Thome, Numerical Simulation of Condensing and Evaporating Flows in Microchannels with Laminar and Turbulent Liquid Films, Proceedings of the 15th International Heat Transfer Conference, IHTC-15, August 10-15, 2014, Kyoto, Japan